OPEN-LOOP AND CLOSED-LOOP TRAILING-EDGE SEPARATION CONTROL ON A NATURAL LAMINAR FLOW AIRFOIL

BY

ROHIT GUPTA

THESIS

Submitted in partial fulfillment of the requirements
for the degree of Master of Science in Aerospace Engineering
in the Graduate College of the
University of Illinois at Urbana-Champaign, 2016

Urbana, Illinois

Adviser:

Assistant Professor Phillip J. Ansell

Abstract

Active Unsteady Flow Control experiments were performed on a Natural Laminar Flow, NLF 0414 airfoil at $Re_c = 1.0 \times 10^6$ in a 3-ft × 4-ft low-speed, low-turbulence wind tunnel. The NLF 0414 was designed with a region of favorable pressure gradient extending almost 70% of the chord on the upper surface of the airfoil. Aggressive pressure recovery in the aft 30% of the chord near the trailing edge results in the separation of the flow from the airfoil surface at the off-design conditions. The goal of this study was to control boundary-layer separation across the trailing-edge region of the airfoil in an effort to improve the performance beyond the designed angle-of-attack range.

Active control of separation was achieved using a series of fast-switching solenoid valves connected to blowing slots at $x/c = 0.75$ on the upper surface of the airfoil. The airfoil in its baseline configuration was first evaluated to identify the dominant modes in the spectral content of unsteady C_p. Airfoil performance data were then acquired across a parametric range of blowing amplitudes, actuation frequencies and duty cycles in order to understand the effects of variations in the major forcing parameters on the performance of the model. Phase-averaged and phase-locked planar PIV measurements were also acquired across a horizontal plane near the trailing-edge region of the airfoil model in order to examine the spatio-temporal evolution of the flowfield and understand the mechanism responsible for the alleviation of separation as a result of actuation at the different flow control settings.

A closed loop controller was developed to vary the actuation parameters *in-situ* using sensory feedback from the unsteady surface pressure measurements. Adaptive modal decomposition methods were used to identify the frequencies of natural instabilities in the flowfield in real-time. A proportional controller was designed to automatically control the blowing amplitude by estimating the state of the flow and the extent of boundary-layer separation. The closed-loop system was able to simultaneously control the blowing amplitude and the actuation frequency such that a desired value of C_l was obtained.

Acknowledgements

This work would not be complete without the support and guidance that I received from my adviser Prof. Phil Ansell. He has been tremendously helpful in bringing this work to completion and I have enjoyed every moment of my time working under his supervision. Additionally, I have also appreciated the conversations we have had outside the work environment on broader topics in science.

Nothing that I've ever done would have been successful without my parents and my family and I am forever indebted for their love and support. Knowledge that I've gained over the years through conversations with my Uncle has been incredibly helpful in my life and will continue to do so in the future. Undergraduate education that I've received as a student at IIEST, particularly the classes taught by Prof. Mukherjea and our subsequent discussions, have been invaluable in developing my interest in fluid mechanics and I consider myself very fortunate to have been his student.

Just as much as my advisor, I am also grateful to Jeff Diebold, Ryan Fontaine, Ruben Hortensius, Gavin Ananda and Brent Pomeroy for all the help and support I've received and the things I've learned from them during my time as a graduate student. On the same page, I am also thankful to all the members of the Aerodynamics and Unsteady Flows research group for their help with my experiments in the Aerodynamics Research Lab. Notwithstanding the time away from my family, I have always felt at home through the company of my friends who have always been an integral part of my life.

Table of Contents

List of Figures

List of Tables

Nomenclature

List of Symbols

α	airfoil angle of attack
A_{ss}	cross-section area of the wind tunnel settling section
A_{ts}	cross-section area of the wind tunnel test section
b	span of the airfoil model
B	flow control blowing ratio
c	airfoil chord length
C_d	airfoil drag coefficient
C_l	airfoil lift coefficient
C_m	airfoil pitching moment coefficient
C_μ	jet momentum coefficient
C_p	pressure coefficient
D	airfoil drag
DC	actuation duty cycle
ε	tunnel blockage velocity increment factor
f	dimensional actuation frequency
F^+	non-dimensional actuation frequency
F	aerodynamic forces
h	test section height
h_{slot}	blowing slot width
λ_{ci}	swirling strength
L	airfoil lift
l_{slot}	blowing slot length
$\dot{m}$	mass flow rate
M	airfoil pitching moment or Mach number
PR	actuation pressure ratio
P	static pressure
P_o	total pressure

q	dynamic pressure
ρ	density
R	universal gas constant
Re_c	chord-based Reynolds number
σ	streamline curvature compensation factor
S	airfoil reference area
t	airfoil thickness
T	static temperature
T_u	Turbulence intensity
U	velocity or uncertainty
V_m	volume of the airfoil model
ω	vorticity
x	airfoil chordwise direction
y	airfoil chord-normal direction

List of Abbreviations

AFC	active flow control
DFT	discrete Fourier transform
DTC	digital temperature compensation
EMD	empirical mode decomposition
FFT	fast Fourier transform
IMF	intrinsic mode function
LUT	look-up-table
NLF	natural laminar flow
PID	proportional-integral-derivative controller
PIV	particle image velocimetry
PSD	power spectral density
SLA	stereolithography
SCXI	signal conditioning eXtensions for instrumentation
ZNMF	zero-net-mass flux

Chapter 1

Introduction

Flow control is a mechanism where some form of actuation or manipulation is used to alter the flow characteristics from what would naturally occur. This process is typically preferred to produce more desirable performance characteristics from an aerodynamic geometry. Historically, flow control has primarily been used to delay transition, postpone separation, enhance lift, reduce drag, augment turbulence, and suppress noise.[1] If an Active Flow Control (AFC) method is used, boundary-layer forcing can be provided through steady or unsteady actuation. Unsteady Active Flow Control can be further divided into two categories: open-loop and closed-loop. In an open-loop flow control system, the flow control parameters, such as amplitude and frequency of actuation, are determined *a-priori*. On the other hand, in closed-loop flow control architecture, real-time information of the flowfield is obtained through sensors, which is then used to determine and drive the flow control actuation required to obtain the desired state of the flowfield.

1.1 Review of Literature

Schubauer and Skramstad[2] were first to introduce periodic perturbations in a laminar boundary layer to trigger a known instability, i.e. to initiate Tollmien-Schlichting waves. This breakthrough technique became a major tool for controlling laminar separation and transition.

Seifert et al.[3] investigated the concept of using oscillatory blowing to delay boundary layer separation on a flapped NACA 0015 airfoil equipped with a two-dimensional slot over the hinge of the flap. A steady source of momentum was supplied by a compressed air source over which relatively small oscillations were superimposed by a centrifugal blower. Significant benefits were observed when actuation was performed within the frequency range, $1 < F^+ < 3$ at a Reynolds number of $Re_c = 0.15 \times 10^6$. It was found in this study that the jet momentum required to achieve a given increase in performance was an order of magnitude less for unsteady actuation, as compared to steady actuation.

Wu et al.[4] performed two-dimensional simulations of turbulent flow over an NACA 0012 airfoil at angles of attack beyond stall. Unsteady actuation was found to modulate the evolution of the separated shear layer in a way that promoted the formation of concentrated vortices. Improvements in lift and reductions in drag were observed even at extreme angles of attack. Non-dimensional frequencies within a wide range, $0.3 < F^+ < 2.0$, were found to be equally effective in enhancing the performance of the airfoil due to the existence of a broad spectrum of unsteadiness in the separated shear layer. The authors also reported a minimum threshold value of $C_\mu \sim 0.01$, below which the effects of pulsed actuation were found to be insignificant.

McCormick[5] proposed a new concept, named the 'Directed Synthetic Jets' for boundary layer separation control. These actuators are similar to synthetic jets and zero-net mass flux (ZNMF) actuators. Unsteady actuation based on the new concept was observed to be effective on an airfoil over a range of $C_\mu = 0.0005 – 0.005$ at $Re_c = 5 \times 10^5$. As in the previous study, the separation control method was observed to be effective over a wide range of frequencies $F^+ = 0.25 – 3.5$ leading the authors to conclude that the frequency of actuation was not strongly associated with the performance of the airfoil.

Raju et al.[6] performed simulations on an NACA 4418 airfoil at a chord-based Reynolds number, $Re_c = 40{,}000$, and for an angle of attack of $\alpha = 18°$. The spectral content of the velocity across various locations within the flowfield was found to contain three distinct frequency scales corresponding to the leading-edge shear layer, separation bubble and the wake. Forcing at frequencies near the separation bubble frequency provided effective reduction in separation and a significant increase in the lift-to-drag ratio. On the other hand, shear layer forcing at frequencies of the order of $F^+ = O(10)$, resulted in an increase in the size of separation bubble, producing unfavorable effects in terms of separation control. In contrast, Griffin et al.[7] conducted flow

control experiments on a flat plate using zero-net-mass flux (ZNMF) actuators and demonstrated that actuation at the shear layer frequency produced the strongest pressure recovery from the baseline separated flow. Furthermore, experiments performed by Amitay and Glezer[8] on a symmetric NACA airfoil with a cylindrical leading edge at $Re_c = 3.1 \times 10^5$, reported a frequency of actuation of the order of $F^+ = O(10)$ to be highly effective.

Volino et al.[9] used synthetic vortex generating jets to prevent boundary layer separation from the suction side of a low-pressure turbine airfoil. Momentum transfer as a result of turbulent mixing was reasoned to be the dominating factor responsible for the performance gains. Reduced frequencies and blowing ratios (B) in the range of $F^+ = 0.14 – 0.56$ and $1 < B < 3$ were found to be extremely effective for this configuration. Higher duty cycles (DC) of actuation were found to perform better than actuation at the lower duty cycles, which was consistent with previous studies conducted by Packard and Bons[10] on an NACA 64_3-618 airfoil model. In contrast however, a later investigation by Hipp et al.[11] found that for post-stall angles of attack, low duty cycle actuation promoted early interaction and mixing between vortices and proved to be more effective than high duty cycle actuation.

Hecklau et al.[12] performed an experimental investigation of two different AFC concepts applied to a highly loaded compressor cascade. Pulsed blowing from the sidewalls was used for the suppression of secondary flow structures while the pressure-induced boundary-layer separation in the rear part of the blade was suppressed by means of pulsed excitation out of the slots in the blade's suction surface. The authors further implemented a closed-loop MIMO control architecture using static pressure at the trailing edge and measurements from spanwise pressure sensors as the control variables. Along similar lines, a more recent study conducted by Lee et al.[13] employed a PID-based closed-loop control algorithm on an NACA 64A210 airfoil. The frequency of actuation was modeled as a function of the chordwise mean pressures and pressure gradients. The control parameters for the PID controller were tuned experimentally. In contrast, Becker et al.[14] used the knowledge of static streamwise pressure differences to drive an extremum-seeking control algorithm that could be optimized in real-time at different test conditions, significantly improving the stability of the closed-loop controller. Corke et al.[15] developed a closed-loop dynamic stall control architecture by employing a thresholding method. This method compared the measured strength of pressure fluctuations, corresponding to the spectral energy for a given frequency of actuation, to a pre-determined threshold value. In the

event where the spectral energy of the pressure fluctuation was measured to be higher than the threshold value, plasma actuators installed close to the leading edge were set to a 'high powered' control state inducing flow reattachment on the upper surface of the airfoil. Pinier et al.[16] employed a correlation analysis between large-scale structures in the flow, extracted from the velocity field of the flow using Proper Orthogonal Decompositon, and surface pressure measurements to develop a robust closed loop flow control scheme. The information about the state of flow was obtained directly from the surface pressure measurements as a result of the correlation, which further helped in determining the most effective control parameters for active flow control.

The most effective actuation parameters reported in literature are summarized in Table 1.1, where the wide range of reported effective actuation frequencies complicate our understanding of the parametric influence of F^+ in unsteady actuation. For blowing amplitudes however, there appears to be a consensus on the existence of a threshold value which defines minimum amplitude that must be surpassed for unsteady actuation to provide any appreciable performance improvement. Unlike most other control parameters, very little investigation has been conducted into identifying the parametric influence of duty cycle to express any definite conclusions with regards to its influence on the performance enhancement of an aerodynamic geometry.

Table 1.1 Recommendations on the best actuation parameters from studies in literature

Author(s)	Model	Re	F^+	C_μ
Seifert et al. (1993)	Flapped NACA 0025	1.5×10^5	1.0–3.0	0.006–0.014
Wu et al. (1989)	NACA 0012	5.0×10^5	0.3–2.0	> 0.01
McCormick (2000)	Diffuser Geometry	5.0×10^5	0.25–3.5	0.0005–0.005
Raju et al. (2008)	NACA 4418	0.4×10^5	O(1)	-
Amitay and Glezer (2002)	NACA Sym- (Cyl. LE)	3.1×10^5	O(10)	-
Volino et al. (2012)	LPT Airfoil	0.25×10^5	0.14–0.56	$1.0<B<3.0$

1.2 Research Motivation and Objectives

While most of the earlier studies on airfoil flow control have focused on leading-edge separation control, the current investigation is aimed at instigating active flow control to manipulate trailing-edge separation on a Natural Laminar Flow (NLF 0414) airfoil in an effort to

improve its performance at off-design angles of attack. This study is further necessitated by the fact that previous studies involving the NLF 0414 have only focused on passive flow control methods through the use of vortex generators and boundary layer trips[17] in order to extend the performance beyond the narrow design regime. Moreover, the majority of the research in active flow control applied towards performance enhancement of aerodynamic geometries has utilized a parametric approach for the selection of optimal actuation parameters. In this investigation, however, major emphasis has been placed on understanding the flow physics of the primary forcing parameters i.e., F^+, DC and C_μ on the evolution of the flowfield around the NLF 0414 airfoil. This physics-based approach is expected to provide deeper insights into the mechanism governing the control of separation through unsteady actuation. Finally, most closed-loop flow control architectures developed in the past have relied on a great deal of *a-priori* calculation and correlation between sensory feedback and the state of the flow around a given geometry. An effort has been made in this study to develop an adaptive yet physically-relevant closed-loop flow control architecture that has real-time actuation frequency and amplitude control capabilities. The primary objectives of the current investigation can be summarized as follows:

- Characterize the spectral content of the relevant modes of unsteadiness present in the flowfield around the trailing-edge region of the NLF 0414 airfoil.
- Understand the flow physics of primary forcing parameters, i.e., F^+, DC and C_μ on open-loop trailing-edge separation control.
- Design a robust yet adaptive closed-loop flow control scheme that uses a physics-based approach of sensing the presence and extent of flow separation, and performing actuation based on the observed state of the boundary layer.

Chapter 2

Experimental Methods

This chapter describes the experimental methods and facilities used in this investigation. It includes a detailed description of the experimental setup, measurement systems, data acquisition practices, data reduction techniques, and methodology for active unsteady flow control.

2.1 Aerodynamic Testing Environment

2.1.1 Wind Tunnel

All of the experiments were conducted in an open-return type, subsonic wind tunnel. The wind tunnel had a rectangular test section, measuring 2.8 ft × 4 ft and extending 8 ft in length along the streamwise direction. The test section was designed with a linear gradient in the sectional area such that the downstream end was slightly larger in size in comparison with the upstream end in order to accommodate the growth of boundary layer along the walls. A four-inch thick honeycomb flow straightener and a total of four anti-turbulence screens formed the inlet section of the wind tunnel. This flow conditioning configuration was effective in containing the turbulence intensity in the test section to within 0.1% at all operating speeds. The ratio of the

sectional areas of the inlet of the wind tunnel to the upstream end of the test section was 7.5:1. A schematic of the wind tunnel is shown in Fig. 2.1.

An ABB ACS 800 Low Voltage AC Drive, with a regulated 125-horsepower AC motor was used to drive a five-bladed fan installed near the end of the tunnel diffuser. The motor was capable of achieving a maximum angular speed of approximately 1200 RPM corresponding to an empty test section speed of approximately 165 mph (242 ft/sec). The chord-based Reynolds number of an airfoil model was calculated using,

$$\mathrm{Re} = \frac{\rho U_\infty c}{\mu} \tag{2.1}$$

where U_∞ is the test-section freestream velocity, c is the airfoil chord, ρ is the air density, and μ is the dynamic viscosity of the air. The chord-based Reynolds number was controlled through an iterative computer routine to within 0.5% of the desired value during testing.

The freestream velocity in the test-section was determined implicitly by measuring the difference in the static pressures (ΔP) between the inlet settling section and the test-section inlet ($P_{ss} - P_{ts}$) using a Setra 239 15 in. WC differential pressure transducer. The static pressure at each of the two tunnel sections was measured as an average of the static pressures read by four pressure taps installed on each of the four tunnel walls. With assumptions of a steady, inviscid and incompressible flow through the tunnel, an expression of a constant volume flow rate (Eq. 2.2) across each section of the wind tunnel was used in conjunction with Bernoulli's equation (Eq. 2.3) applied at the settling section and the test section inlet to calculate the test section speed (Eq. 2.4)

$$A_{ss} U_{ss} = A_{ts} U_{ts} \tag{2.2}$$

$$\frac{1}{2}\rho U_{ts}^2 + P_{ts} = \frac{1}{2}\rho U_{ss}^2 + P_{ss} \tag{2.3}$$

$$U_{ts} = \sqrt{\frac{2\left(P_{ss} - P_{ts}\right)}{\rho_{amb}\left(1 - \left(\frac{A_{ts}}{A_{ss}}\right)^2\right)}} \tag{2.4}$$

where the term A_{ts}/A_{ss} represents the inverse of the contraction area ratio and ρ_{amb} represents the ambient air density. The air density could be calculated from the ideal gas expression,

$$\rho_{amb} = \frac{P_{amb}}{RT_{amb}} \tag{2.5}$$

where R represents the specific ideal gas constant for air. P_{amb} and T_{amb} were measured using a Setra 270 absolute pressure transducer and an Omega thermocouple respectively.

2.1.2 Airfoil Model and Flow Control System

The current study was performed using a single element NLF 0414 airfoil, presented in Fig. 2.2. The airfoil model was stereo-lithographically (SLA) fabricated from a thermosetting plastic, and had an 18-inch chord and 33.563-inch span. The NLF 0414 model was mounted vertically in the test section, spanning the tunnel floor to the tunnel ceiling, as shown in Fig. 2.3. In order to isolate the loads experienced by the airfoil model from the tunnel, a small gap was introduced at both walls of the test section. The load from the airfoil was transferred to the force balance through spars centered at x/c = 0.30 and 0.56 (Fig. 2.2). These spars formed the main load carrying members of the airfoil model and were mounted on the force balance using L-shaped mounting brackets described in detail in section 2.2.1. Additional rigidity to the airfoil model was provided through a series of semi-cylindrical ribs incorporated into the skin of the model as shown in Fig. 2.4.

The model was fitted with 68 static pressure taps distributed over the upper and lower surfaces near the mid-span, which were used for acquiring time-averaged static pressure measurements. In order to prevent the downstream taps from being enveloped by a turbulent wedge generated by an upstream tap, the static pressure taps were staggered at an angle of approximately 15° with respect to the freestream direction as shown in Fig. 2.5. Thus, each pressure tap was displaced along the spanwise axis with respect to the nearest upstream pressure tap by an angular separation that was larger than the half-spreading angle of the turbulent wedge. This two-dimensional distribution of pressure taps ensured that the airfoil pressure measurements were largely unaffected by tap-induced turbulence.

In addition to the static pressure taps, a total of five ultra-miniature high frequency response pressure transducers, model XCS-062-5D manufactured by Kulite Semiconductor Products Incorporated, were also integrated on the upper surface of the model at x/c = 0.1, 0.3, 0.5, 0.7 and 0.9. All of the unsteady pressure transducers were configured and calibrated by the manufacturer for a ±5 psi differential maximum pressure. The unsteady pressure transducers

were manufactured with a cylindrical outer shell, having a length of 0.375-inches and a diameter of 0.066-inches. Each transducer was equipped with four lead wires and a reference tube, which was connected to a reference pressure source (Fig. 2.6), described in greater detail in section 2.3.2. The lead wires were routed to the designated temperature compensation modules. The signal wires out of the temperature compensation modules were used to provide excitation and obtain voltage measurements from the pressure transducer.

The model also featured 12 blowing slots, each 1.5-inches long and 0.018-inches wide, spaced equally along the span on the upper surface at x/c = 0.75. The width of the slot was designed to be 0.1% of the chord length of the airfoil based on the recommendations of Englar,[18] who performed a parametric study on slot sizing involving the jet kinetic energy, coanda effect and power requirement for actuation. The exit of the blowing slot was inclined at an angle of 30^o with respect to the local tangent at the surface to enhance the effectiveness of pulsed actuation (Gunther et al.[19]). The path of the blowing slot was designed with a circular cross-section on the inlet side which transformed seamlessly into a rectangular profile at the exit, as shown in Fig. 2.7. This design was intended to provide a more uniform distribution of air at the exit of the blowing slot. A set of 12 fast-switching solenoid valves (Festo, MHJ-10 with a switching frequency up to 1000 Hz), were used to switch the blowing on and off through each of the 12 slots at a precisely controlled frequency (f) and duty cycle (DC). The solenoid valves were embedded inside the model in close proximity to the blowing slots in order to prevent damping of the unsteady switching, which occurs across long pneumatic lines. An access panel was incorporated on the lower surface of the airfoil that could be removed to provide easy access to the flow control components embedded inside the airfoil (Fig. 2.4 a)).

The airfoil model also housed a distribution manifold that was used to uniformly distribute air to each of the 12 solenoid valves. The air to the distribution manifold was fed through a pneumatic tube which was routed through the main spar from underneath the test section. A compressed air tank was used as the source of air for the flow control system. The mass flow rate was regulated by implicitly regulating the pressure using an electro-pneumatic pressure regulator (SMC, ITV-3050 series) and simultaneously measuring the mass flow rate using a high precision mass flow meter (Omega, FMA-1600A series). The process of setting a desired mass flow rate was automated through a computer routine. A schematic of the flow control system is presented in Fig. 2.8.

2.2 Force Balance Measurements

2.2.1 Balance Measurement Acquisition

Measurements of the model lift, drag, and quarter-chord pitching moment were obtained using a three-component force balance, shown in Fig. 2.9 manufactured by Aerotech ATE Limited. The airfoil model was mounted to the force plate of the balance using L-shaped mounting brackets which were further clamped to the airfoil model mounting spars and fastened to the force plate. This force plate was attached to a turntable which was used to regulate the model angle of attack to an accuracy of ±0.02°. Measurements from three load cells were used to calculate the forces in the normal and axial direction, and the moment about the center of the force plate. The airfoil model and the load bearing members of the force balance were isolated from the tunnel side-walls and the ground to prevent undesirable load transfers, thereby ensuring that the airfoil forces and moments were directly transferred to the balance force plate.

The balance signal conditioning system provided three different user-controlled load range settings (Table 2.1), each of which was associated with a different level of sensitivity. The load range setting could therefore be changed to ensure a high signal-to-noise ratio in the final measurements. The highest load range setting was used for all three balance components in this investigation. The balance signal conditioning system consisted of an amplifier and a low pass filter. Full-scale output voltage of the balance load cells were low pass filtered at a cutoff frequency of 1 Hz and subsequently amplified to a final full-scale output voltage of ±5 V. All of the balance results reported in this investigation were acquired at a sample rate of 100 Hz for a period of two seconds. These measurements were then time-averaged to produce an average voltage representative of the steady normal, axial force and pitching moment about the center of the force plate.

Table 2.1 Three-component balance load ranges

	HIGH RANGE	MEDIUM RANGE	LOW RANGE
NORMAL FORCE	±450 lb	±225 lb	±90 lb
AXIAL FORCE	±90 lb	±55 lb	±18 lb
PITCHING MOMENT	±45 ft-lb	±30 ft-lb	±15 ft-lb

2.2.2 Airfoil Performance Coefficients from Balance Measurements

Balance voltage measurements were zero corrected by subtracting the tare voltages acquired with the wind tunnel fan off across the desired angle of attack range. The resulting zero-corrected voltage (V_{0i}) was scaled by a range ratio (RR_i), summarized in Table 2.2, to compensate for the gain applied by the balance signal conditioning system. The scaled voltage (V_i) was calculated using,

$$V_i = (V_{0i})(RR_i) \tag{2.6}$$

Table 2.2 Three-component balance range ratios

	HIGH RANGE	MEDIUM RANGE	LOW RANGE
NORMAL, RR_N	1	0.4944	0.2046
AXIAL, RR_A	1	0.6278	0.2173
MOMENT, RR_M	1	0.6755	0.3413

The normal force, axial force, and pitching moment about the balance center (F_N, F_A, M) were then calculated from the corresponding scaled voltages from a system of coupled second-order algebraic equations using calibration test results provided by the manufacturer. The normal force, axial force and pitching moment about the balance center were calculated using,

$$\begin{Bmatrix} F_N \\ F_A \\ M \end{Bmatrix} = \begin{bmatrix} 37.7 & 0.03159 & -0.2095 & 0.01094 & 0 & -0.000865 \\ -0.1607 & 8.3125 & -0.01638 & 0.007084 & 0 & 0.007660 \\ -0.01299 & -0.005521 & 1.247 & -0.002122 & 0 & 0.0001497 \end{bmatrix} \begin{Bmatrix} V_N \\ V_A \\ V_M \\ V_N^2 \\ V_A^2 \\ V_M^2 \end{Bmatrix} \tag{2.7}$$

The resulting forces along the chord-normal and chord-axial directions were then rotated by the airfoil angle of attack (α) to obtain the airfoil lift and drag forces. The airfoil lift and drag forces were calculated using,

$$L = F_N \cos\alpha - F_A \sin\alpha \tag{2.8}$$

$$D = F_N \sin\alpha + F_A \cos\alpha \tag{2.9}$$

With knowledge of the balance normal and axial forces (F_N, F_A) and the offset between the quarter-chord location of the airfoil to the center of the balance (x_{offset}, y_{offset}), the airfoil pitching moment about balance center was redefined about the airfoil quarter-chord using,

$$M_{c/4} = M - x_{offset}F_N + y_{offset}F_A \tag{2.10}$$

The airfoil lift coefficient, drag coefficient and the quarter-chord pitching moment coefficient were calculated using,

$$C_l = \frac{L}{q_\infty S} \tag{2.11}$$

$$C_d = \frac{D}{q_\infty S} \tag{2.12}$$

$$C_m = \frac{M_{c/4}}{q_\infty Sc} \tag{2.13}$$

where q_∞ denotes the freestream dynamic pressure, S denotes the model reference area, and c denotes the model chord.

The balance measurements were found to be highly consistent with the pressure-based measurements of the airfoil lift and quarter-chord pitching moment. However, the measurements acquired by the balance system were mainly used for diagnostic and validation purposes and will not be reported here. The drag measurements from the balance were found to be slightly higher than the measurements obtained from a wake survey system. This increase was largely attributed to the gaps between the airfoil model and the test-section walls, which was necessary to ensure the model loads were properly transferred to the balance. However, these gaps led to the introduction of a small but significant induced drag component, especially at the higher angles of attack. Drag measured with the force balance includes this induced drag component, rendering a value higher than the corresponding measurements made by the wake survey system.

2.3 Pressure Measurements

2.3.1 Time-Averaged Pressure Measurements

Measurements of static pressure on the airfoil surface and the measurements of total

pressure in the wake of the airfoil are the two major classes of time-averaged pressure measurements that were acquired in this investigation. All of the time-averaged pressure measurements were acquired using miniature electronic differential pressure measurement units, models ESP-32HD manufactured by Esterline, Inc. The ESP scanners consisted of an array of silicon piezo-resistive sensors that were connected in a Wheatstone bridge configuration and generated a voltage that was proportional to the pressure input. The output voltages from the scanners were acquired using a Digital Temperature Compensation (DTC) Initium Data Acquisition System. Each of the ESP scanning modules used in this investigation contained 32 ports that could be connected to a series of pressure tubes connecting to either static pressure taps on the surface of the airfoil model or total pressure probes on the wake rake.

A total of 5 ESP-32HD scanners were used in this investigation. The pressure taps across the leading-edge region of the airfoil model, which corresponds to the region of highest expected pressure differentials, were connected to a ±5.0 psid ESP scanner. The remaining pressure taps on the airfoil model were connected to two ±1.0 psid ESP scanners. The total pressure probes in the wake rake were connected to two ±0.35 psid (±10.0 in. WC) ESP scanners. Pressure measurements were acquired at a sample rate of 50 Hz and time-averaged over a period of two seconds. All of the static pressure measurements on the airfoil surface were zero-referenced against the static pressure inside the test section of the wind tunnel. On the other hand, all of the total pressure measurements in the wake of the airfoil were zero-referenced against the ambient pressure inside the testing facility. The ESP scanners also featured a two position calibration manifold which could be switched between the run and calibrate modes by applying momentary pulses of control pressures. This calibration mode allowed the zero-load voltage of each channel to be redefined. The DTC Initium system provided a 6^{th} order, temperature-compensated calibration curve for each port, which was used to convert acquired voltages to pressure measurements.

2.3.1.1 Airfoil Performance Coefficients from Surface Pressure Measurements

In addition to measuring the model surface static pressures and the total pressures in the wake of the airfoil, one of the ports in the pressure scanner was reserved for measuring ($P_{ss} - P_{ts}$) in order to calculate the velocity and dynamic pressure of the freestream flow with an accuracy greater than the accuracy of the velocity calculated using the Setra 239 pressure transducer, as

outlined in section 2.1.1. The measurements from the Setra 239 pressure transducer were only used to set the tunnel speed to achieve a desired Reynolds number.

Static pressure measurements about the surface of the airfoil model were non-dimensionalize by the freestream dynamic pressure, based on the pressure measurements from the ESP pressure scanners, to obtain the conventional form of the pressure coefficient. The dynamic pressure of the freestream flow (q_∞) was calculated using,

$$q_\infty = \frac{1}{2}\rho_\infty U_\infty^2 \tag{2.14}$$

Using Eq. 2.4, Eq. 2.14 can be rewritten in terms of the tunnel contraction ratio as,

$$q_\infty = \frac{1}{2}\rho_\infty U_{ts}^2 = \frac{P_{ss} - P_{ts}}{1 - \left(\frac{A_{ts}}{A_{ss}}\right)^2} \tag{2.15}$$

with ambient density (ρ_{amb}) in Eq. 2.4 assumed to be equal to the density of freestream air (ρ_∞) used in Eq. 2.14, i.e., the flow through the wind tunnel was assumed incompressible ($M_\infty \leq 0.3$). The pressure coefficient (C_p) of a given location on the airfoil was calculated using,

$$C_p = \frac{P_s - P_\infty}{q_\infty} \tag{2.16}$$

The freestream dynamic pressure (q_∞) was assumed to be constant between the inlet of the test section, where the test section static pressure (P_{ts}) was measured, and the near upstream region of the airfoil model. Since the influence of boundary-layer growth on the cross-sectional area was accounted for in the wind tunnel design, the effective cross-sectional area could be assumed constant from the inlet of the test section to the location of the airfoil model. As a result, the static pressure at the test section inlet could be assumed to be equal to the static pressure encountered by the airfoil model.

The airfoil lift and pitching moment coefficients were calculated from the known static pressure distribution about the surface of the airfoil. This calculation was accomplished by approximating the airfoil contour by a series of panels. Each of the panels was constructed by a linear geometric interpolation of two adjacent pressure taps, thereby generating a total of (*n-1*) panels for *(n)* number of pressure taps. The pressure across the entire length of a panel was

assumed to be the average of the two pressures measured through the pressure taps at the two ends of the panel. The force due to the pressure distribution acting in a direction normal to the surface of a panel was then split into chord-normal and chord-axial components. This component extraction process was achieved through appropriate geometric transformations using knowledge of the panel orientation with respect to the chord line of the airfoil. The chord-normal force and chord-axial force across each panel (ΔF_N and ΔF_A) were calculated using,

$$\Delta F_N' = \frac{P_i + P_{i+1}}{2}\left(x_{i+1} - x_i\right) \tag{2.17}$$

$$\Delta F_A' = -\frac{P_i + P_{i+1}}{2}\left(y_{i+1} - y_i\right) \tag{2.18}$$

The net chord-normal force and chord-axial force acting on a spanwise section of the airfoil model was calculated by taking the sum of the sectional chord-normal and chord-axial forces over all the panels of the airfoil. The airfoil chord-normal sectional force and the chord-axial sectional force were calculated using,

$$F_N' = \sum_{i=1}^{n-1} \Delta F_N \tag{2.19}$$

$$F_A' = \sum_{i=1}^{n-1} \Delta F_A \tag{2.20}$$

The chord-normal and chord-axial sectional forces were further transformed into the airfoil sectional lift force using,

$$L' = F_N' \cos\alpha - F_A' \sin\alpha \tag{2.21}$$

The sectional pitching moment about the airfoil quarter chord due to the chord-normal and the chord-axial sectional forces across a given panel was calculated using,

$$\Delta M'_{c/4_i} = \Delta F_N' \left(x_{c/4} - \frac{x_i + x_{i+1}}{2} \right) + \Delta F_A' \left(\frac{y_i + y_{i+1}}{2} \right) \tag{2.22}$$

In a process similar to the computation of the net chord-normal and chord-axial forces, the net sectional pitching moment about the airfoil quarter-chord was calculated by summing over the

contributions of each panel to the pitching moment about the quarter-chord of the airfoil. The net airfoil sectional quarter-chord pitching moment was calculated using,

$$M'_{c/4} = \sum_{i=1}^{n-1} \Delta M'_{c/4_i} \tag{2.23}$$

The airfoil lift coefficient (C_l) and quarter-chord pitching moment coefficient (C_m) were calculated from the corresponding sectional lift force and quarter-chord pitching moment using,

$$C_l = \frac{L'}{q_\infty c} \tag{2.24}$$

$$C_m = \frac{M'_{c/4}}{q_\infty c^2} \tag{2.25}$$

2.3.1.2 Drag Calculation from Wake Pressures

A wake survey system consisting of a traversable wake rake and a two-axis traverse system was used to obtain profile drag measurements of the airfoil. The wake rake was constructed with 59 total pressure probes, each having an outer diameter of 0.04-inches. The probes were aligned horizontally along the rake in order to acquire the total pressure profile of the airfoil wake downstream of the vertically-oriented airfoil. The wake rake was suspended from the ceiling of the test section using a support structure as shown in Fig. 2.10. It was also capable of being traversed in the vertical (spanwise) and horizontal (chord normal) directions using a two-axis traverse mechanism controlled precisely by a stepper motor. Wake profiles were acquired approximately 1.2 chord lengths downstream of the trailing edge of the airfoil model. The wake rake was traversed in the horizontal (chord-normal) direction until the tails of the wake profile were sufficiently captured. This process was automated through a computer routine that determined the position of the wake tails by comparing the gradient of the total pressure deficit at multiple locations along the span of the wake profile.

The drag of the airfoil was calculated using the standard momentum deficit method described by Jones[20] and Schlichting.[21] The method involves a control volume analysis around the airfoil model with the exit of the control volume considered sufficiently downstream such that the static pressure in the wake at the exit plane (P_w) can be assumed to be equal to the freestream static pressure (P_∞). Due to viscous effects however, the total pressure in the wake is

expected to be lower than the freestream total pressure and this pressure loss can be attributed to the wake velocity deficit. Using the equation of conservation of momentum in the integral form, the drag at a given spanwise section of the airfoil model can be calculated using,

$$D' = \rho \int u_w \left(U_\infty - u_w\right) dy \tag{2.26}$$

The flow velocities can be rewritten in terms of the static and total pressures (within the incompressibility limit) using,

$$P_\infty + \frac{1}{2}\rho U_\infty^2 = P_{0,\infty} \tag{2.27}$$

$$P_\infty + \frac{1}{2}\rho u_w^2 = P_{0,w} \tag{2.28}$$

The velocity terms in Eq. 2.26 are solved for in terms of static and total pressures. The resulting pressure terms are substituted back into Eq. 2.26 to give,

$$D' = 2\int \sqrt{P_{0,w} - P_\infty}\left(\sqrt{P_{0,\infty} - P_\infty} - \sqrt{P_{0,w} - P_\infty}\right) dy \tag{2.29}$$

From Eqs. 2.27 and 2.28, the dynamic pressure at the wake plane can be explicitly expressed in terms of the wake total pressure, freestream total pressure and the freestream dynamic pressure using,

$$q_w = q_\infty - \left(P_{0,\infty} - P_{0,w}\right) \tag{2.30}$$

Using Eqs. 2.29 and 2.30, an expression for the sectional drag of the airfoil can be obtained in terms of the wake total pressure deficit,

$$D' = 2\int \sqrt{q_\infty - (P_{0,\infty} - P_{0,w})}\left(\sqrt{q_\infty} - \sqrt{q_\infty - (P_{0,\infty} - P_{0,w})}\right) dy \tag{2.31}$$

This expression of sectional drag is less complicated than the corresponding expression given by Eq. 2.29 because the difference between the freestream total pressure and the wake total pressure could be directly measured in the wake surveys to obtain an accurate estimate of the sectional drag. However, for greater repeatability of the drag measurements, the ESP scanners used for acquiring the wake pressures were referenced to a stable atmospheric pressure reference

in the control room. With this setup, gauge pressure measurements of the wake total pressure, ($P_{0,w} - P_{atm}$), were obtained in the wake of the airfoil while gauge pressure measurements of the freestream total pressure, ($P_{0,\infty} - P_{atm}$), were obtained in the potential flow region outside the wake of the airfoil. Thus the pressure deficit could be calculated using,

$$P_{0,\infty} - P_{0,w} = \left(P_{0,\infty} - P_{atm}\right) - \left(P_{0,w} - P_{atm}\right) \tag{2.32}$$

Using the expression of wake total pressure deficit given by Eq. 2.32, the sectional drag of the airfoil was calculated by numerically integrating Eq. 2.31 using the trapezoid method. Thus, the sectional drag of the airfoil could be calculated using,

$$D' = \sum_{i=1}^{n_{rake}-1} \left[\sqrt{q_\infty - (P_{0,\infty} - P_{0,w_i})} \left(\sqrt{q_\infty} - \sqrt{q_\infty - (P_{0,\infty} - P_{0,w_i})} \right) + \sqrt{q_\infty - (P_{0,\infty} - P_{0,w_{i+1}})} \left(\sqrt{q_\infty} - \sqrt{q_\infty - (P_{0,\infty} - P_{0,w_{i+1}})} \right) \right] (y_i - y_{i+1}) \tag{2.33}$$

where n_{rake} represents the total number of probes that were used to measure the wake. Due to manufacturing imperfections and finite span of the airfoil model, the flow around the model is generally associated with non-zero spanwise variation. As such, the sectional drag of the airfoil calculated using Eq. 2.33 was averaged over multiple spanwise stations to provide a spanwise invariant estimate of the sectional drag that would be characteristic of a true airfoil model of infinite span. The drag coefficient of the airfoil model was calculated from Eq. 2.33 using,

$$C_d = \frac{D'}{q_\infty c} \tag{2.34}$$

2.3.2 Unsteady Pressure Measurements

Unsteady pressure measurements were obtained using a total of five ultra-miniature, high frequency response pressure transducers. These transducers were manufactured by Kulite Semiconductor Products Incorporated, under model designation XCS-062-5D. The pressure transducers were integrated on the upper surface of the airfoil at x/c = 0.1, 0.3, 0.5, 0.7 and 0.9 as described in section 2.1.2. The unsteady pressure signals from the transducers were acquired through a National Instruments Signal Conditioning eXtensions for Instrumentation (SCXI) measurement system and a National Instruments PCI-MIO-16XE-10 A/D board.

The SCXI system consisted of a set of four signal conditioning modules: SCXI-1140 Simultaneous-Sampling Differential Amplifier module, SCXI-1142 8th order Lowpass Bessel Filter module, and two SCXI-1121 Isolation Amplifiers with Excitation modules. The SCXI-1121 modules were each connected to a SCXI-1321 terminal block, which provided a simple electrical connection platform for the measurement transducers. Excitation and electrical isolation of the instruments were provided through the SCXI-1121 module. In order to prevent aliasing, the SCXI-1142 module was configured to the correct Nyquist cutoff frequency using filter specifications provided by the manufacturer. The SCXI-1140 module provided for the simultaneous sampling of signals from each of the five pressure transducers. This simultaneity in the acquired signals was accomplished by storing the voltages acquired at any instant of time in a series of capacitors. The A/D system was then able to sample the voltages stored in the capacitors successively. A small gain was also applied to the voltage measurements in order to enhance the signal to noise ratio and improve the digitization of the analog signal. All of the SCXI modules were compactly integrated into a SCXI-1001 chassis. A schematic of the SCXI setup is presented in Fig. 2.11.

The XCS-062 pressure transducer consisted of a diaphragm connected in a four arm Wheatstone bridge configuration with an output voltage that was linearly proportional to the applied pressure. The calibration slope and intercept associated with each transducer was determined through a five-point calibration procedure. Thus, the pressure sensed by the transducer (ΔP_{trans}) against a known reference pressure could be calculated using,

$$\Delta P_{trans} = m V_{trans} + b \tag{2.35}$$

where m represents the calibration slope, b represents the intercept of the calibration and V_{trans} represents the output voltage of the transducer. All of the transducer measurements were zero-corrected by acquiring the tare voltages prior to each run. Data from these unsteady pressure transducers were used to calculate the Power Spectral Density (PSD) described in section 2.7.1.1.

2.4 Hot-film Measurements

Hot-film measurements were acquired at the exit of the blowing slots using a single-element hot-film probe (Fig. 2.12). All of the hot-film measurements were acquired using

a TSI Model 1201 Disposable Probe, with a TSI IFA-100 Constant-Temperature Anemometer. The constant-temperature anemometer consisted of a Wheatstone-bridge circuit coupled with a feedback amplifier. Fluctuations in the temperature of the hot-film probe caused by local perturbations in the fluid velocity introduced voltage imbalances in the Wheatstone-bridge circuit. The feedback amplifier was used to supply additional current into the circuit in order to restore the balance of the Wheatstone-bridge configuration and thus, maintain the hot-film probe at a constant temperature. The response time of the feedback amplifier was determined using a square-wave impulse test[22]. The hot-film setup used in the present investigation had a frequency-response of 5 kHz.

Prior to acquiring measurements of the jet velocities at the exit of the blowing slots, the hot-film probe was calibrated by simultaneously measuring the local fluid velocity using a pitot-static probe and recording the voltage output of the hot-film anemometer. The calibration was performed for a series of different velocity settings, ranging from near-zero test-section velocity to the maximum velocity of the tunnel. The hot-film probe measurements were also corrected for local fluctuations in ambient temperature[23] and density[24] at each calibration point. A 4^{th} degree least-squares fit was constructed using the calibration data points. The calibration coefficients were then used to convert the acquired hot-film measurements to velocity measurements at the exit of the blowing slots.

The jet velocity measurements were acquired across the span of the blowing slot at discrete spatial intervals of about 4.5 mm, the spatial resolution being limited by the dimensions of the probe tip. The velocity at each spanwise section of the slot was recorded for a single time period of actuation. The data were then numerically integrated to obtain an average representation of the flow rate over a cycle of actuation. The process was repeated at other slots for a series of different actuation parameters to check for consistency between the calculated and the experimentally determined mass flow rate over an actuation cycle. Example jet velocity histories for three different duty cycles of actuation are shown in Fig. 2.13.

2.5 Flow Diagnostics Methods

2.5.1 Fluorescent Oil Surface Flow Visualization

Fluorescent-oil surface flow visualization was used in the present investigation to provide a qualitative understanding of the time averaged surface flowfield characteristics of the airfoil model, such as a leading edge separation bubble, laminar-to-turbulent transition points, and surface traces of turbulent jet crossflow interaction during flow control.

The fluorescent-oil surface flow visualization process was completed in multiple steps. First the airfoil model was wrapped in black contact paper, which provided a high contrast between the fluorescent oil and the airfoil surface. Next, two lengths of yellow tape with marks at regular chordwise intervals of 10% were applied to provide a representative scale to the acquired images and for easy identification of the chordwise locations of flowfield characteristics of interest. Next, a thin coat of 5W-30 motor oil was applied over the surface of the contact paper. The application of motor oil was intended to minimize surface imperfections thereby facilitating the flow of fluorescent oil across the surface of the contact paper. Next, the fluorescent oil mixture, created by mixing mineral oil and an oil-based leak detector dye, was sprayed homogeneously on the surface of the airfoil using an airbrush.

The airfoil model was then set at the desired angle of attack and the tunnel was run at a given test condition for a total of four minutes. After the tunnel was turned off, the model was rotated back to $\alpha = 0°$. Long-wave UVA radiation from black lights was used to excite the leak detector dye in the fluorescent oil mixture. Images of the upper surface of the airfoil were then documented using a Nikon D3100 digital SLR camera at multiple extended exposure times.

2.5.2 Particle Image Velocimetry

Particle Image Velocimetry (PIV) is a non-intrusive experimental technique that is used to determine the instantaneous velocity fields by measuring the velocity of small tracer particles that accurately track the motion of the fluid.[25] These particles are introduced artificially into the flow and are illuminated by a high-intensity coherent source of light such as a laser. Measurements of velocity of the tracer particles are achieved by recording successive images of the particles at precisely defined time intervals and determining the displacement of particles across small regions of the field of view.

In this study, planar PIV data were acquired across a horizontal plane at the trailing-edge region of the airfoil model extending from $x/c = 0.7$ to $x/c = 1.0$, as shown in Fig. 2.14. All of the PIV measurements were acquired at an angle of attack of $\alpha = 7°$. A dual-pulsed Nd:YAG laser, model Gemini 200 PIV manufactured by New Wave Research Inc., was used to project two consecutive laser pulses, each delivering an average energy of 45 mJ at 532 nm. The separation time between the two laser pulses was maintained at 25 μs, which resulted in an average particle displacement of 8 pixel units. This average particle displacement was deemed optimum for processing using a 32×32 pixel interrogation window. A combination of converging and diverging lenses was used to form a collimated laser sheet, approximately 1 mm thick, at the trailing-edge region of the airfoil model. The image plane for PIV acquisition was centered at one of the blowing slots near the center span of the airfoil.

In order to minimize surface reflections while acquiring data, a reflector was mounted inside the test section downstream of the airfoil model, which projected the laser sheet upstream almost parallel to the surface of the airfoil near the trailing-edge region. Vibrations induced by unsteady aerodynamic forces were minimized by mounting the reflector inside a streamlined housing (Fig. 2.15), which was securely clamped to the ceiling of the test section. By configuring the laser sheet to graze the surface of the airfoil, the intensity of the reflected light off of the airfoil model was significantly reduced, as compared to a direct impingement of the laser sheet.

The flow was seeded using a ViCount smoke generator, model Compact 1300 manufactured by Concept Engineering Ltd. The smoke generator was capable of producing oil-based smoke particles ranging from 0.2-0.3 μm in size and was carefully operated to maintain a uniform seeding density inside the test-section of the wind tunnel. A high-resolution (1600×1200 pixel) PCO.1600 14 bit charge-coupled device (CCD) camera equipped with a 35-105 mm zoom lens at an *f*-number setting of 5.6 was used to record images of the PIV tracer particles. The PCO Camware application software was used to interface the camera with a computer.

The laser and camera system were synchronized using a BNC Model 625A digital-delay generator. A random time delay was introduced in the data acquisition process to ensure statistical independence of the acquired data sets for an accurate phase-averaged representation of the flowfield. For the phase-locked measurements of the velocity field however, the PIV system was synchronized with the flow control actuation cycle. The experimentally acquired

particle image pairs were processed using the DaVis software package from LaVision. The correlation process used multiple iterations at interrogation window sizes ranging from 64 × 64 pixel windows to 32 × 32 pixel windows at 50% overlap to obtain the final vector field. A set of numerical post-processing filters was also utilized to eliminate erroneous vectors in the instantaneous velocity fields.

2.6 Wind Tunnel Corrections

A wind tunnel testing environment is designed to simulate the flow around an airfoil model in a spatially unbounded freestream. Due to the infeasibility of such a design, however, the true wind tunnel testing environment is constrained with finite wall boundaries introducing local wall effects that are absent in a hypothetically unbounded freestream. The acquired data were corrected to compensate for three major tunnel wall effects through standard correction procedures following the work of Barlow et al.[26] for 2D, low-Reynolds number wind tunnel testing. These three effects included solid blockage, wake blockage, and streamline curvature. The validity of these corrections is, however based upon the assumptions of steady, incompressible flow.

The solid blockage effect is caused by an effective reduction in the test-section cross-sectional area, producing local flow accelerations that are functions of model thickness and angle of attack. The effects of the local acceleration can be corrected for using a solid-blockage velocity increment factor, ε_{sb}[26], defined by,

$$\varepsilon_{sb} = \frac{K_1 V_m}{C^{3/2}} \tag{2.36}$$

where K_1 is a constant parameter based on the airfoil configuration (K_1 = 0.52 for airfoil models spanning the height of the test-section[26]), C is the empty test-section area, and V_m is the volume of the airfoil model which was estimated using,

$$V_m = \frac{3}{4} tcb \tag{2.37}$$

where t and b are the dimensional thickness and span of the airfoil model.

Since the wake of an airfoil model is usually associated with a region of velocity deficit, a local region of increased streamwise velocity is produced across the potential flow regions

outside the wake of the airfoil to ensure a constant mass flux across any given cross-section of the wind tunnel. Moreover, since the profile drag of the airfoil is directly related to the extent of velocity deficit in the wake, it can be empirically correlated with the local flow acceleration outside the wake region. Thus, the influence of this wake blockage effect can be determined using the wake blockage velocity increment factor, ε_{wb}, which can be calculated using,

$$\varepsilon_{wb} = \frac{1}{2}\frac{c}{h}C_{d,u} \tag{2.38}$$

where h and $C_{d,u}$ are the height of the test section and the uncorrected value of the airfoil drag coefficient respectively. The net velocity increment due to a combination of the solid and wake blockages is calculated by a linear summation of the solid blockage correction factor and the wake blockage correction factor and is given by,

$$\varepsilon = \varepsilon_{sb} + \varepsilon_{wb} \tag{2.39}$$

The constraints imposed by finite wall boundaries also introduce streamline curvature effects that would otherwise be absent in an unbounded flowfield. These curvature effects increase the apparent camber of the airfoil leading to an increment in the lift and the magnitude of the quarter-chord pitching moment in comparison with the lift and moment values that would be obtained in an unbounded environment. The streamline curvature effect can be compensated for using an empirically derived variable σ, which can be calculated using,

$$\sigma = \frac{\pi^2}{48}\left(\frac{c}{h}\right)^2 \tag{2.40}$$

The airfoil angle of attack, pressure coefficient, lift coefficient, drag coefficient and quarter-chord pitching moment coefficient were corrected using a set of empirically derived relations with terms involving the correction factors calculated in Eqs. 2.36, 2.38, and 2.40.
The corrected airfoil angle of attack and performance coefficients were calculated using,

$$\alpha_{cor} = \alpha_u + \frac{57.3\sigma}{2\pi}\left(C_{l,u} + 4C_{m,u}\right) \tag{2.41}$$

$$C_{l,cor} = C_{l,u}\left(1 - \sigma - 2\varepsilon\right) \tag{2.42}$$

$$C_{d,cor} = C_{d,u}\left(1 - 3\varepsilon_{sb} - 2\varepsilon_{wb}\right) \tag{2.43}$$

$$C_{m,cor} = C_{m,u}\left(1 - 2\varepsilon\right) + \frac{1}{4}\sigma C_{l,u} \tag{2.44}$$

$$C_{p,cor} = \frac{C_{p,u}}{\left(1+\varepsilon\right)^2} \tag{2.45}$$

2.7 Flow Control Methodology

2.7.1 Open-Loop Flow Control

2.7.1.1 Power Spectral Density

Power Spectral Densities (PSDs) were computed for the acquired unsteady pressure measurements in order to characterize the spectral content of unsteady modes of interest. The PSDs of acquired unsteady pressure measurements were calculated using standard fast Fourier transform (FFT) methods. A fast Fourier transform is an algorithm that is used to compute the discrete Fourier transform (DFT) of a signal more rapidly than a standard DFT calculation. The DFT of a signal is described using

$$X_k = \sum_{n=0}^{N-1} x_n e^{-i 2\pi k \frac{n}{N}} \qquad k = 0, 1, 2, \ldots, N-1 \tag{2.46}$$

where X_k represents the transformed signal, $x_0, \ldots, x_{N-1}$ are complex numbers, N is the number of data points in the DFT, and k represents the discrete frequency values such that

$$f_k = \frac{k}{N\Delta t} \qquad k = 0, 1, 2, \ldots, N-1 \tag{2.47}$$

where Δt is the temporal spacing of data points. The series outside the range $0,\ N-1$ is assumed to be N-periodic, i.e. $x_n = x_{n+N}$ for all $n = 0, 1, 2, \ldots, N-1$. The power spectral density (G_{xx}) is then defined as,[27]

$$G_{xx}(f) = 2\lim_{T\to\infty}\frac{1}{T}E\left[\left|X_k(f,T)\right|^2\right] \tag{2.48}$$

where E represents the expected value of the bracketed term. Using a reference power level (P_0), the amplitude of the PSD can be expressed in decibel (dB), which is a logarithmic ratio of units of power. For the current study, P_0 was defined as unity. This conversion from power to decibel was calculated using

$$L_{dB} = 10\log_{10}\left(\frac{P_1}{P_0}\right) \tag{2.49}$$

In the current study, the PSDs were calculated using 1.44 million data points split between 20 identical runs of 72,000 samples each, in order to observe distribution of power across the frequency spectrum ranging from f = 0 Hz to the Nyquist frequency (i.e. half of the sampling frequency).

2.7.1.2 Flow Control Parameters

An active unsteady flow control system is generally associated with two major control parameters: non-dimension actuation frequency (F^+) and non-dimensional jet momentum coefficient (C_μ). In the present investigation, two different length scales were utilized when calculating the non-dimensional actuation frequency. The first length scale was based on the quarter-chord length of the airfoil (c/4), and the corresponding non-dimensional actuation frequency was calculated using Eq. 2.50. While the chord length is commonly used as the characteristic length scale in the literature, the quarter-chord length was preferred in the current study, as it reflects the distance from the blowing slot to the airfoil trailing edge.

$$F^+ = \frac{f\left(\frac{c}{4}\right)}{U_\infty} \tag{2.50}$$

The second frequency scaling utilized the projected airfoil height from the location of the blowing slots to the trailing edge ($csin\alpha$/4), as the characteristic length scale. This length scale has been shown in previous studies to be commensurate with the scale of the largest eddies in the flow.[28] The second dimensionless frequency was calculated using,

$$F_{\text{var}}^{+} = \frac{f\left(c\sin\alpha\right)}{4U_{\infty}} \tag{2.51}$$

A number of studies use look-up-tables (*LUT*) to determine C_{μ} as a function of the input parameters. However, for the present study, the mean velocity of the jet at the exit of the slots was calculated directly by applying the principle of continuity with measured flow parameters at the mass flow meter and the combined area of all the blowing slots as:

$$C_{\mu} = \frac{2}{h_{slot}c}\left(\frac{\dot{m}}{12\rho U_{\infty} l_{slot}}\right)^{2} \tag{2.52}$$

where $\dot{m}$ is the mass flow rate through the pneumatic supply system and ρ is the local density at the slot exit. Using the hot film probe, measurements of the jet velocity at the exit of the blowing slots were acquired for different input pressure ratios (*PR*), frequencies and duty cycles, as discussed in section 2.4. The C_{μ} values determined from the probe were found to be consistent with those calculated using Eq. 2.52.

2.7.2 Closed-Loop Separation Prediction and Control

In addition to being used for flow measurement and diagnostic purposes, the unsteady surface pressure measurements were also used to provide feedback in a closed-loop flow control configuration. The unsteady C_p at $x/c = 0.90$ was used to predict the extent of the separated flow across the trailing edge of the airfoil, as well as the frequencies of the shear-layer instabilities associated with boundary-layer separation. In order to extract this information, the unsteady C_p measurements were processed using Empirical Mode Decomposition (EMD). The EMD method decomposes a time-dependent signal into modal components of varying temporal (i.e., frequency) scales. It is also the decomposition method utilized in the Hilbert-Huang transform (HHT),[29-32] which was developed in order to analyze nonstationary and nonlinear time series data.

Extraction of modes using EMD is conducted through a process known as "sifting," where the highest frequency band of oscillations is extracted from a signal through an iterative process. The mode extraction process is repeated until all of the oscillatory content of a signal is removed, a pre-determined number of modes are extracted, or a certain low-frequency threshold

of the residual signal is reached. These extracted modes are known as Intrinsic Mode Functions (IMFs), which are oscillatory functions featuring time-dependent amplitude and frequency with zero mean. By extracting all of the oscillatory content, this process leaves only the data trend as the residual, which can be nonstationary. The original unsteady signal, $x(t)$, can be reproduced by summing the time-dependent IMFs, $c_j(t)$, and adding that sum to the time-dependent residual, $r(t)$.

An example of the iterative sifting process is shown in Fig. 2.16 on a test signal. The sifting process begins with a given data set, $f(t)$. The local maxima and minima of this signal are identified and connected through splines as shown in Fig. 2.16 a). The instantaneous average of the two extrema is subtracted from the original signal. The average-subtracted signal is then used as an input to a second iteration where the sifting process is repeated identically as in the first case to obtain a second average-subtracted signal (Fig. 2.16 b)). This sifting process is further repeated until the average-subtracted signals converge, i.e., a mean-squared error tolerance is attained. An example of the converged signal is shown in Fig. 2.16 c). This final signal is defined as the first IMF, $c_1(t)$ and the result obtained by subtracting this IMF from the original signal is defined as the residual, $r_1(t)$. Additional IMFs are extracted by repeating the sifting process on the residual, $r_1(t)$.

The physical basis produced by EMD was discussed in detail by Lee et al.[33] EMD has also recently been used in studies involving fluid flows and turbulence,[34,35] where the resulting IMFs are generally used to separate large-scale from small-scale oscillatory content, or serve as a dyadic filter. The EMD method used in the current study was based on the algorithm of Rilling,[36-38] which was then programmed into a LabVIEW environment. This implementation allowed the EMD processing and closed-loop separation control to be conducted in real-time during data acquisition. Prior to processing the C_p measurements through the EMD algorithm, they were first conditioned with a low-pass filter in order to remove the influence of noise and unsteadiness induced by the testing environment at high frequencies. Since most fluid unsteadiness is inherently attributed to broad-band frequency ranges, a masking technique was also used, based on the method of Deering and Kaiser,[39] to reduce the amount of mode mixing experienced during the EMD reduction.

The EMD method was utilized due to its adaptive nature and ability to be employed *in-situ*, requiring little calibration for a specific application. Other decomposition techniques,

such as Proper Orthogonal Decomposition (POD), Balanced Proper Orthogonal Decomposition (BPOD), and Dynamic Mode Decomposition (DMD), are extremely useful for identifying and understanding flow phenomena, though a great deal of *a-priori* calculation and correlation of modal behavior to sensory feedback is typically required when these decomposition methods are used in a flow control context. While it is possible that closed-loop flow control techniques that utilize POD (e.g., Pinier et al.[16]), BPOD, or DMD may result in more effective state estimation than EMD, it was the specific goal of the current study to develop a closed-loop system to be as adaptive as possible while still operating on a physically-relevant modal decomposition.

In order to predict if the flow across the trailing-edge region of the airfoil was separated, the average amplitude of each IMF was compared to a threshold value. If the average amplitude of any of the IMFs was greater than the threshold value, the flow was assumed to be separated at the sensor location. This method is similar to the thresholding method used by Corke et al.[15] However, instead of utilizing a prescribed frequency and amplitude of actuation, the power-weighted frequency of the highest-amplitude IMF was used to set the frequency of actuation, using

$$\overline{f} = \frac{\sum_{i=1}^{k} a(i) f^2(i)}{\sum_{i=1}^{k} a(i) f(i)} \tag{2.53}$$

where a is the amplitude and f is the frequency of the IMF at index i, and k is the number of sample points. The residual of the EMD method was also used to set the C_μ imposed by the pulsed blowing. An overview of the closed-loop control process used in the current study is presented in Fig. 2.17. Since the residual of the EMD method produces the trend of the unsteady signal, in the current application this residual was simply the mean C_p at the sensor location. A proportional controller was used to set the C_μ necessary to achieve a desired C_p with an error of 0.5%. As will be discussed later, the C_p for x/c = 0.90 was identified as being an excellent predictor of the airfoil C_l. A diagram of the proportional controller used to set the necessary C_μ to the desired C_p value is presented in Fig. 2.18.

2.8 Chapter 2 Figures

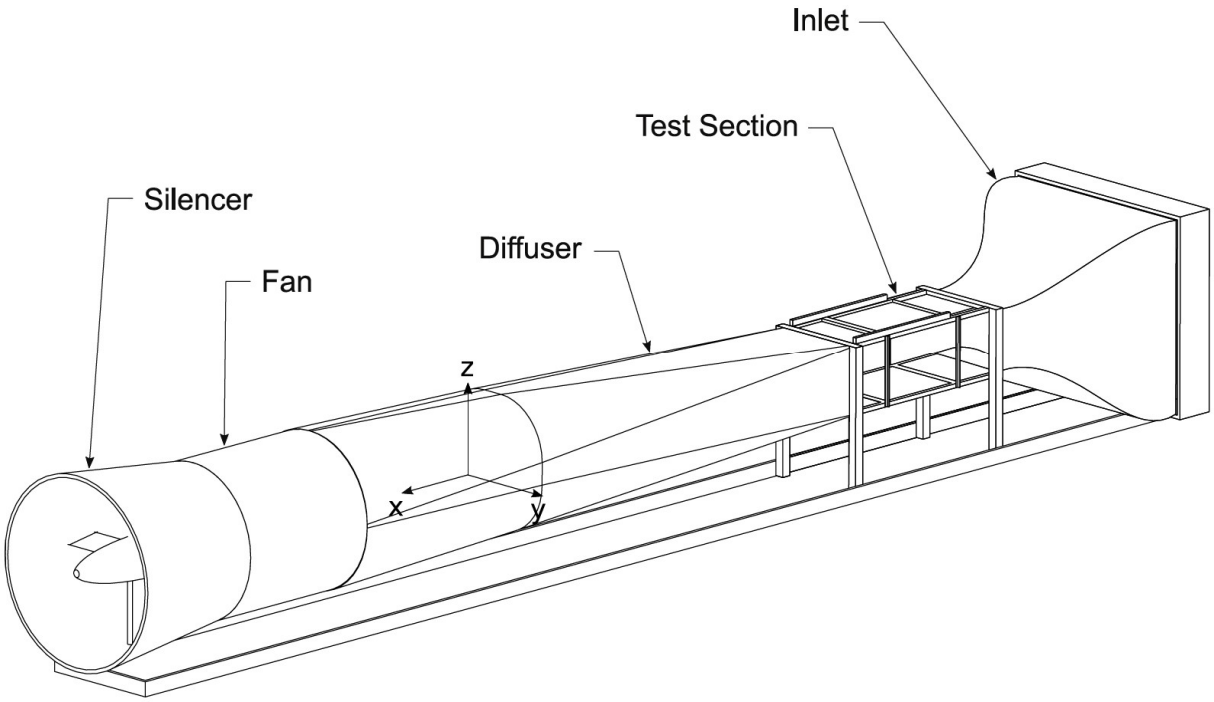

Fig. 2.1 Schematic of the University of Illinois 3-ft × 4-ft subsonic wind tunnel.

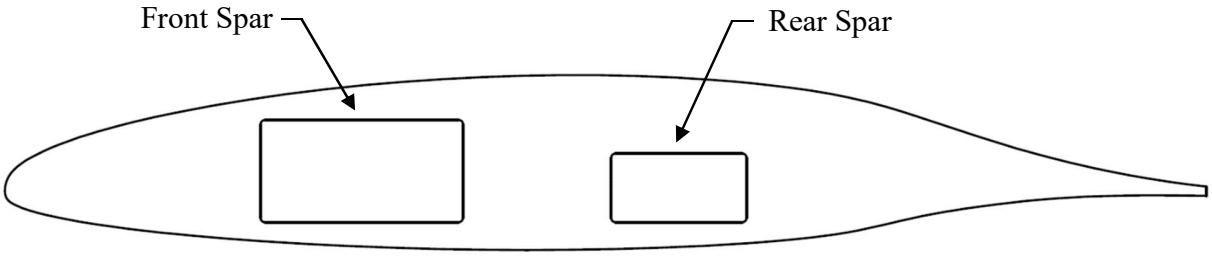

Fig. 2.2 NLF 0414 geometry indicating the relative positions of the front and rear spars.

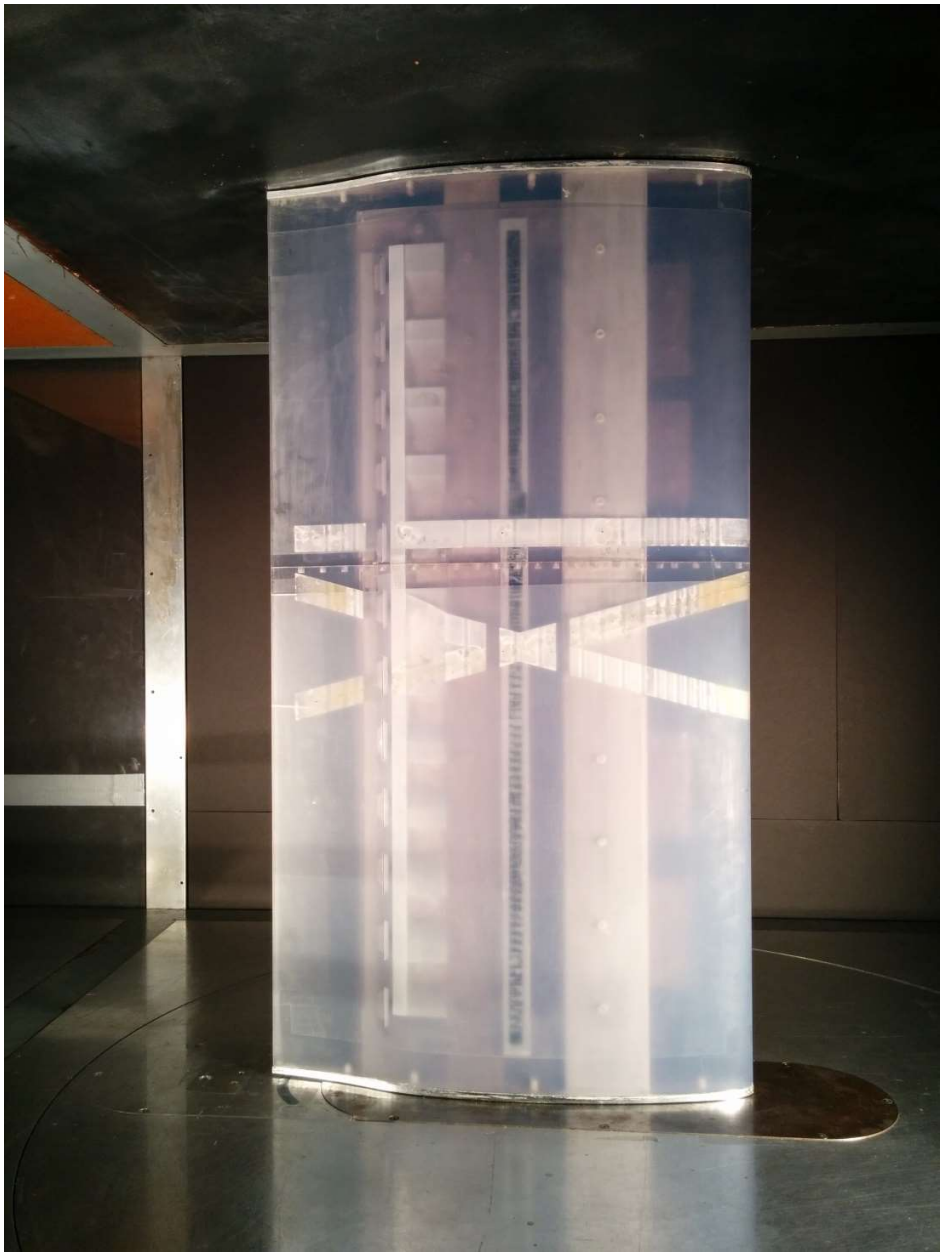

Fig. 2.3 NLF 0414 airfoil model installed in the wind tunnel test section.

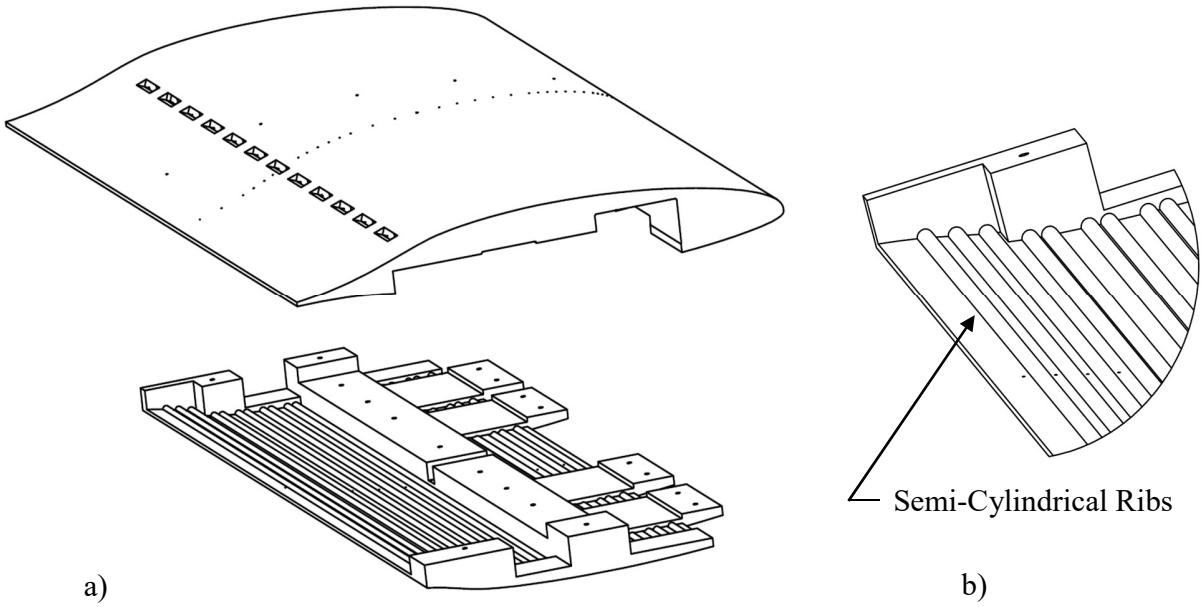

Fig. 2.4 a) Access panel on the lower surface of the NLF 0414 model; b) Semi-cylindrical ribs incorporated into the skin of the model for additional structural rigidity.

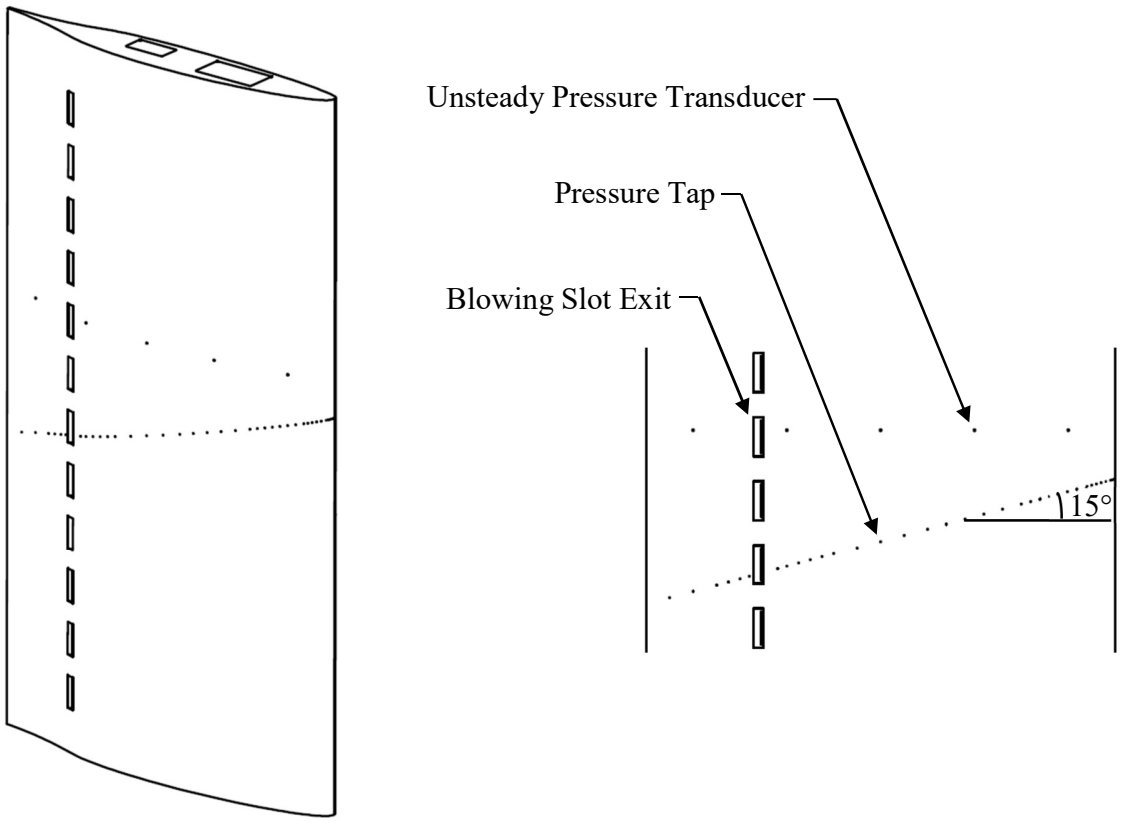

Fig. 2.5 Illustration of the NLF 0414 model components and the static pressure tap stagger angle.

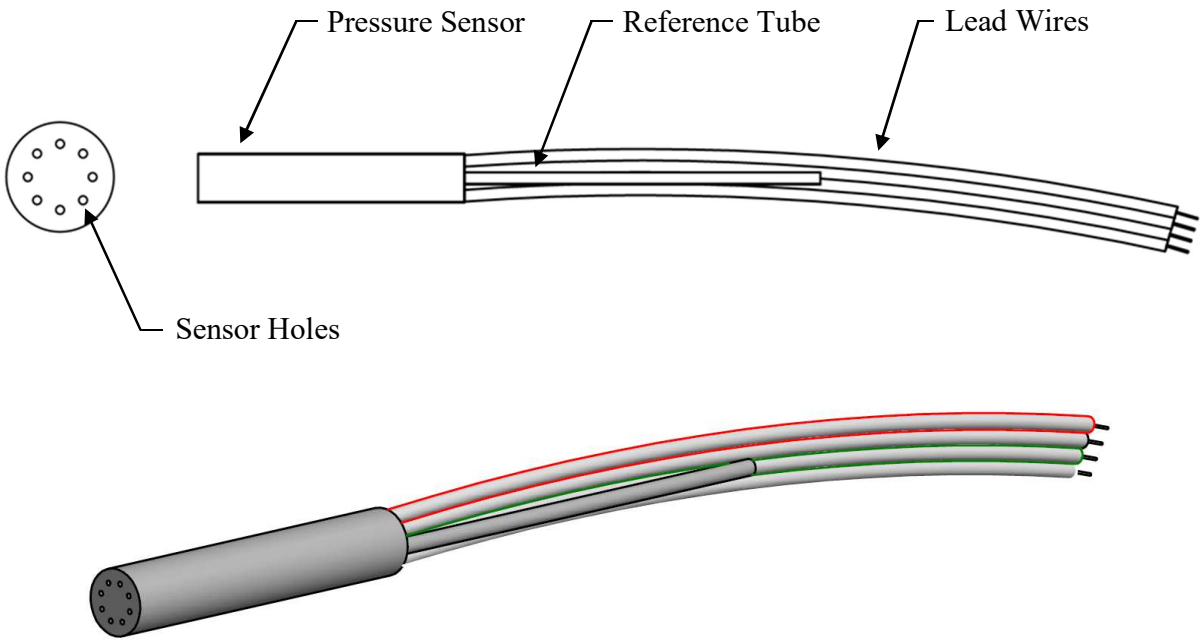

Fig. 2.6 Schematic of the Kulite XCS-062-5D high-frequency response pressure transducer.

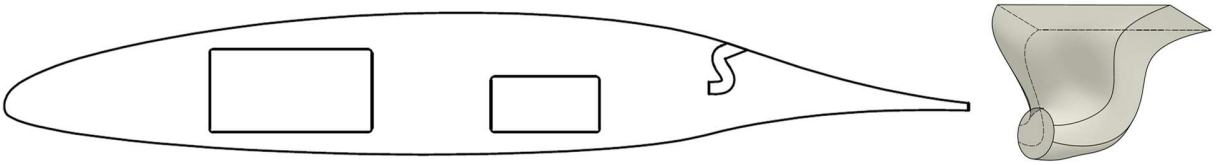

a) b)

Fig. 2.7 a) Sectional view of the blowing-slot path inside the NLF 0414 model; b) 3D profile of the blowing-slot path.

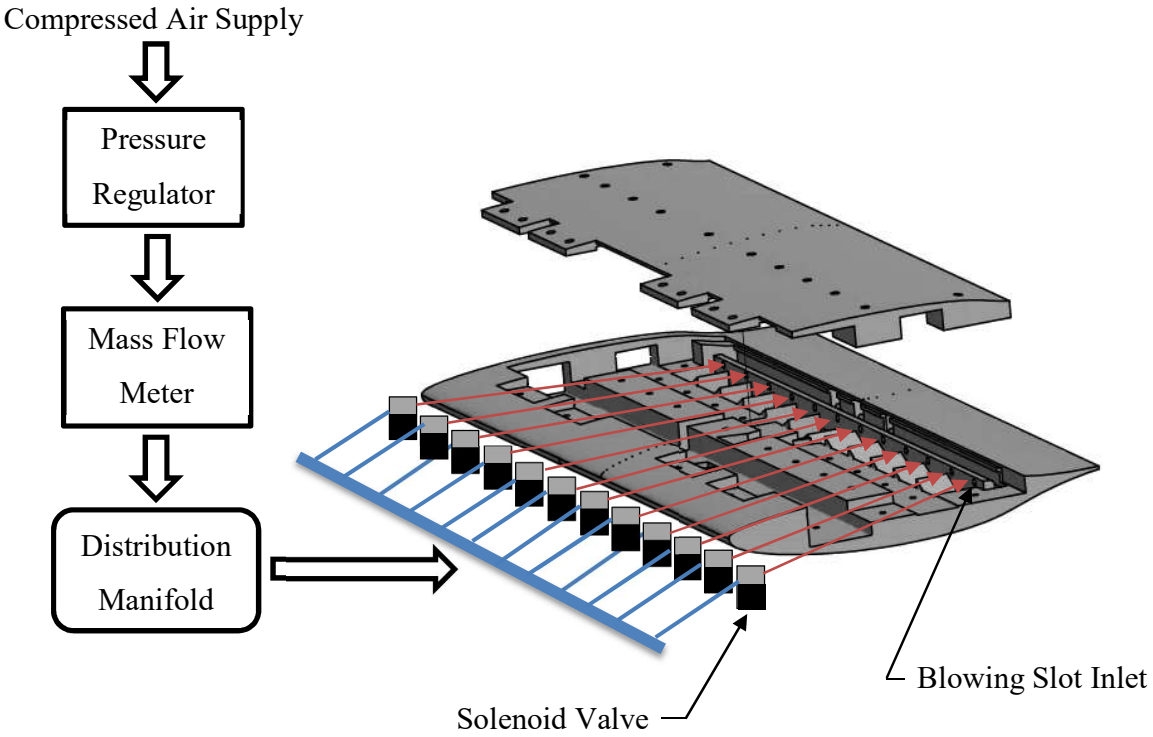

Fig. 2.8 Illustration of the pneumatic circuit for active unsteady flow control.

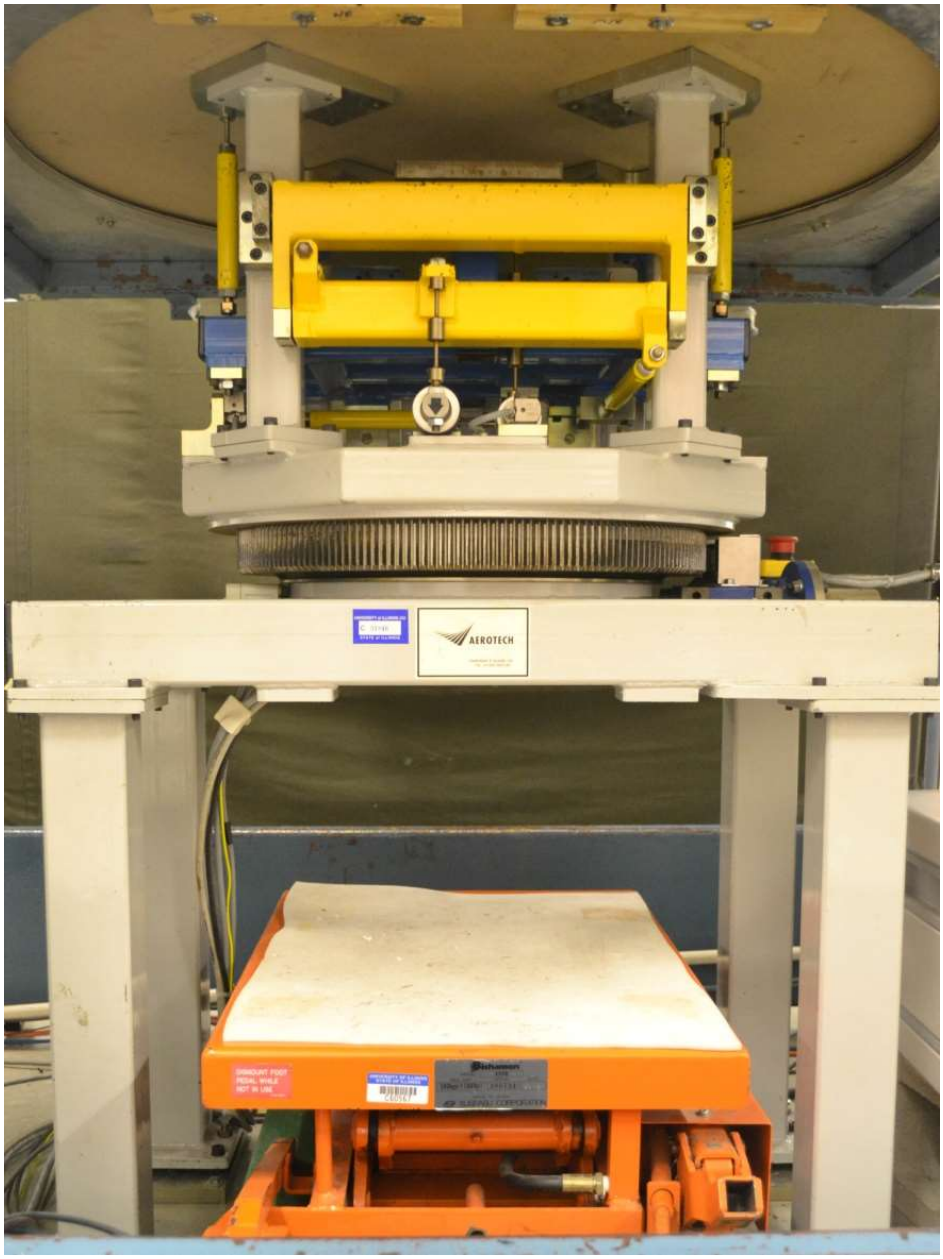

Fig. 2.9 Three-component force balance used to measure the forces and moment on the airfoil model, after Ansell.[40]

Fig. 2.10 Wake rake installed in the test section downstream of the NLF 0414 airfoil model.

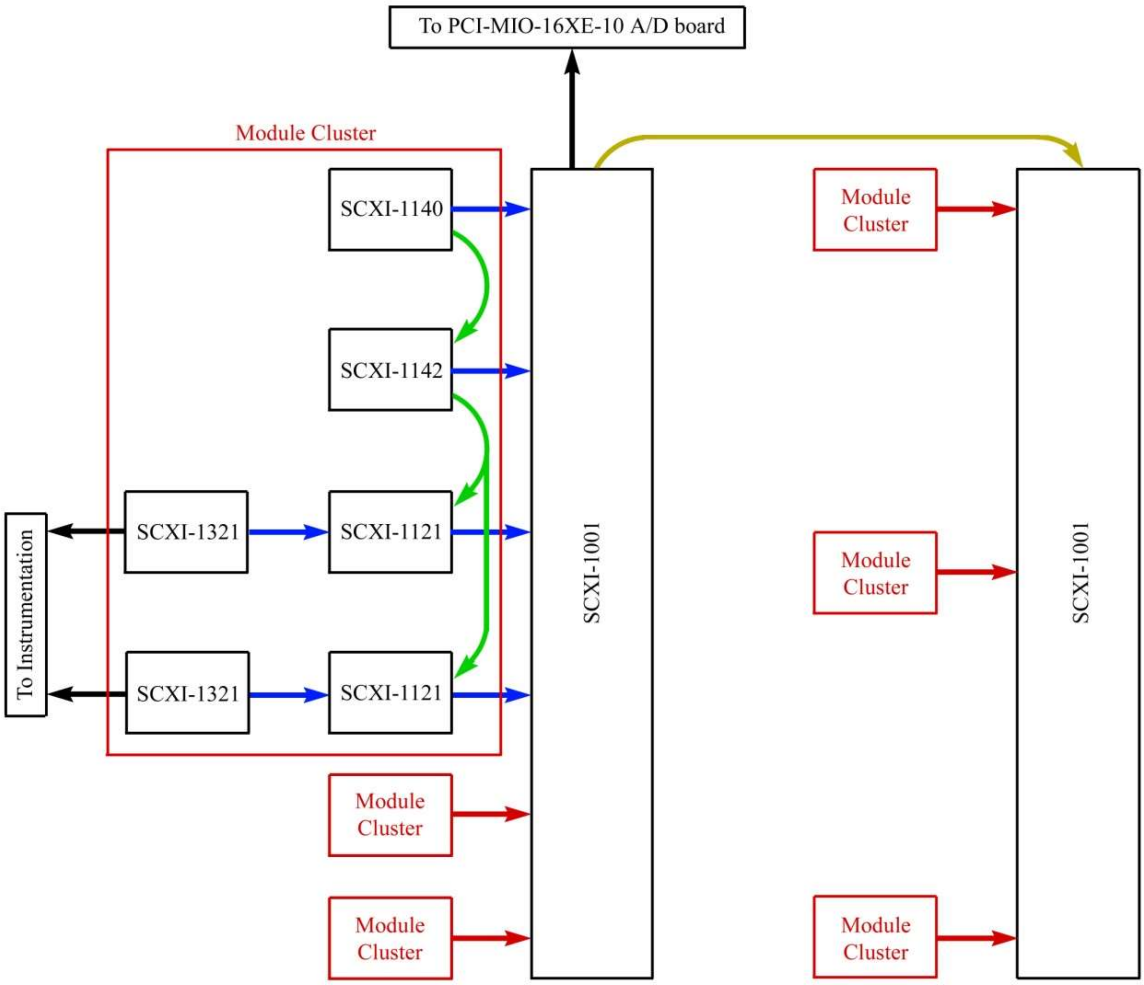

Fig. 2.11 Schematic of the SCXI module and chassis connection, after Ansell.[40]

Fig. 2.12 Hot-film measurement assembly installed near the exit of the blowing slot.

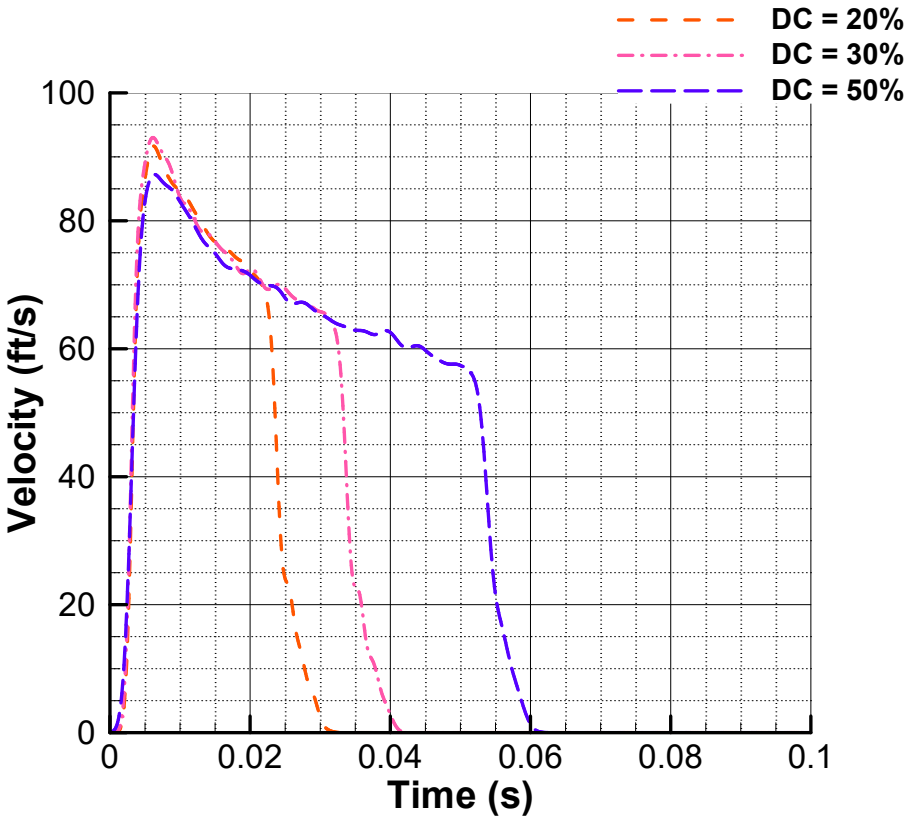

Fig. 2.13 Jet velocity histories for different duty cycles of actuation.

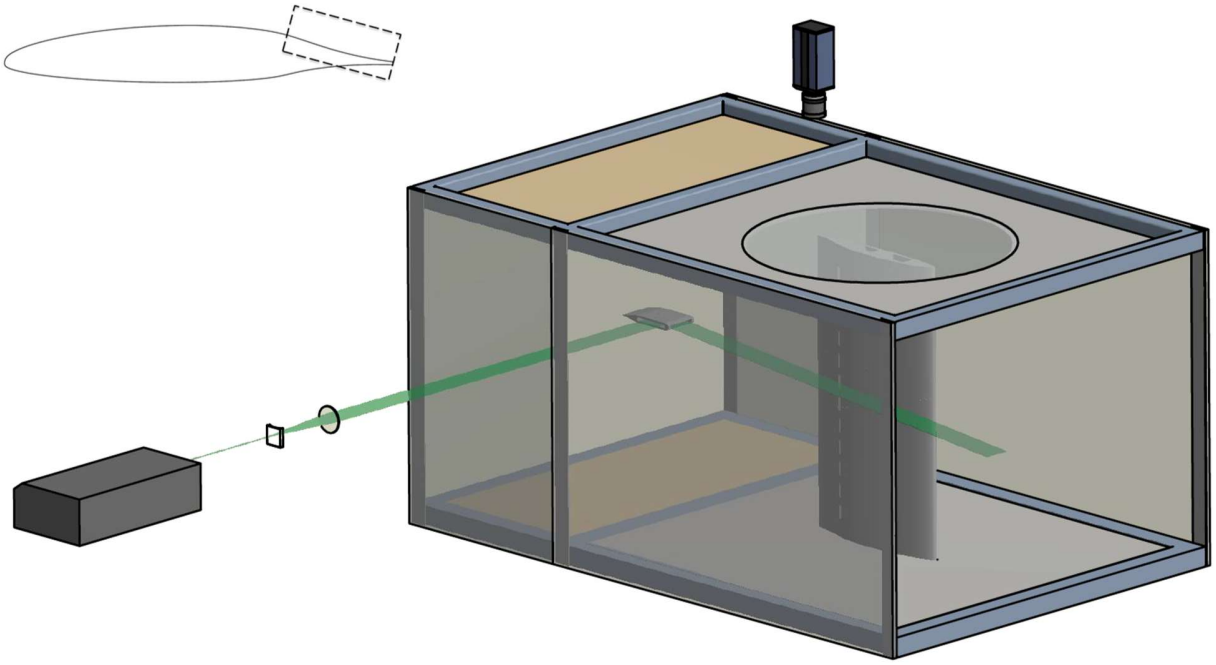

Fig. 2.14 Schematic of the PIV setup and the interrogation region used in the present investigation.

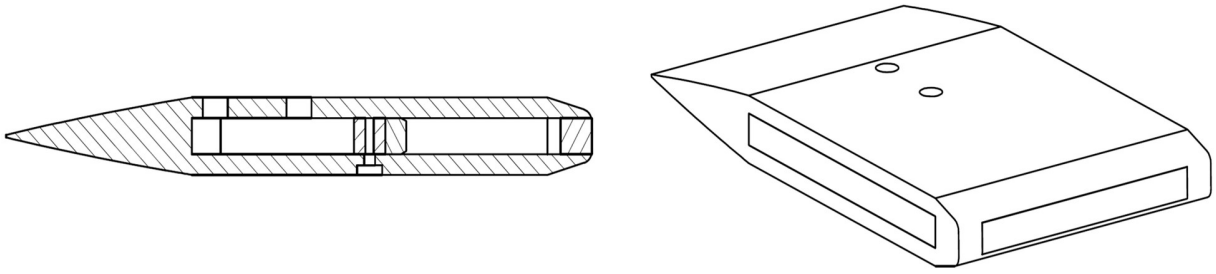

Fig. 2.15 PIV reflector housing designed to minimize vibrations induced by unsteady aerodynamic forces.

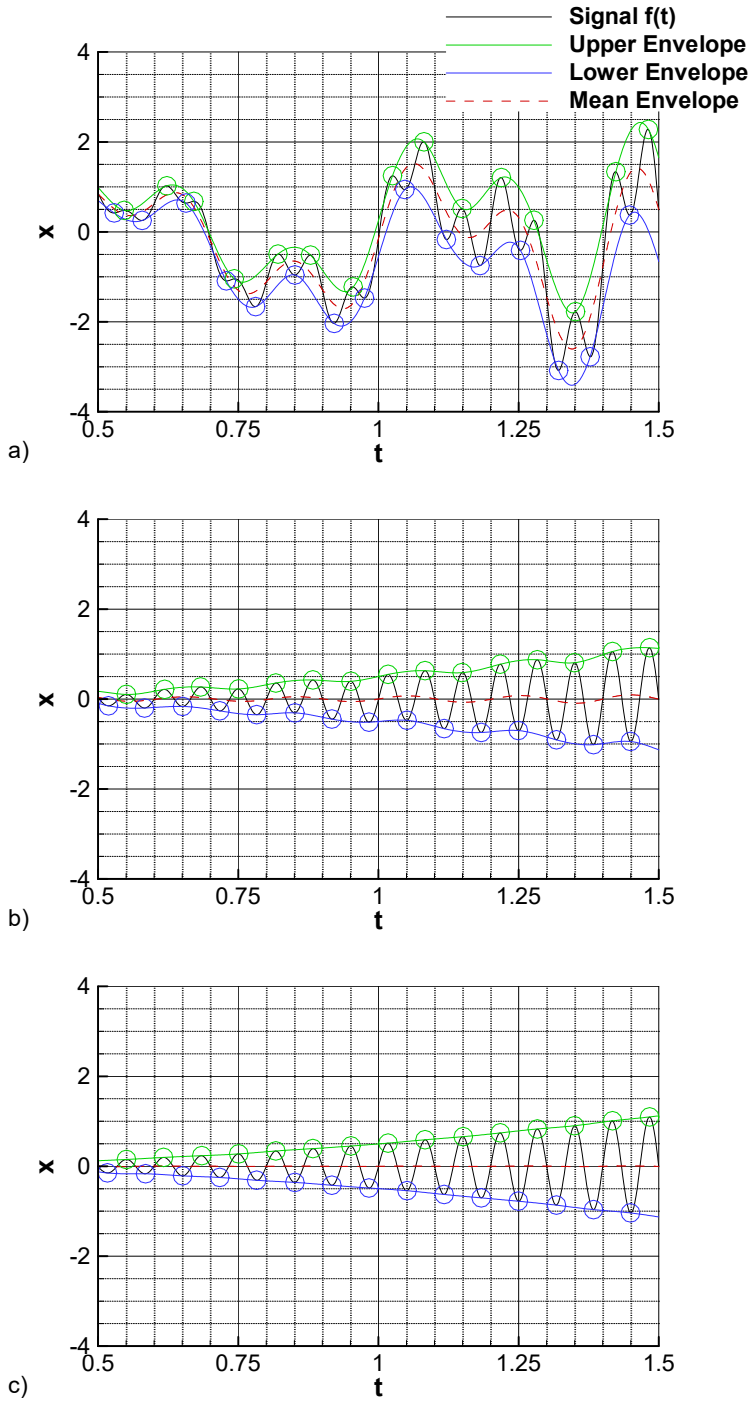

Fig. 2.16 Illustration of sifting process; a) original test signal, b) second sifting iteration, c) converged sifting process.

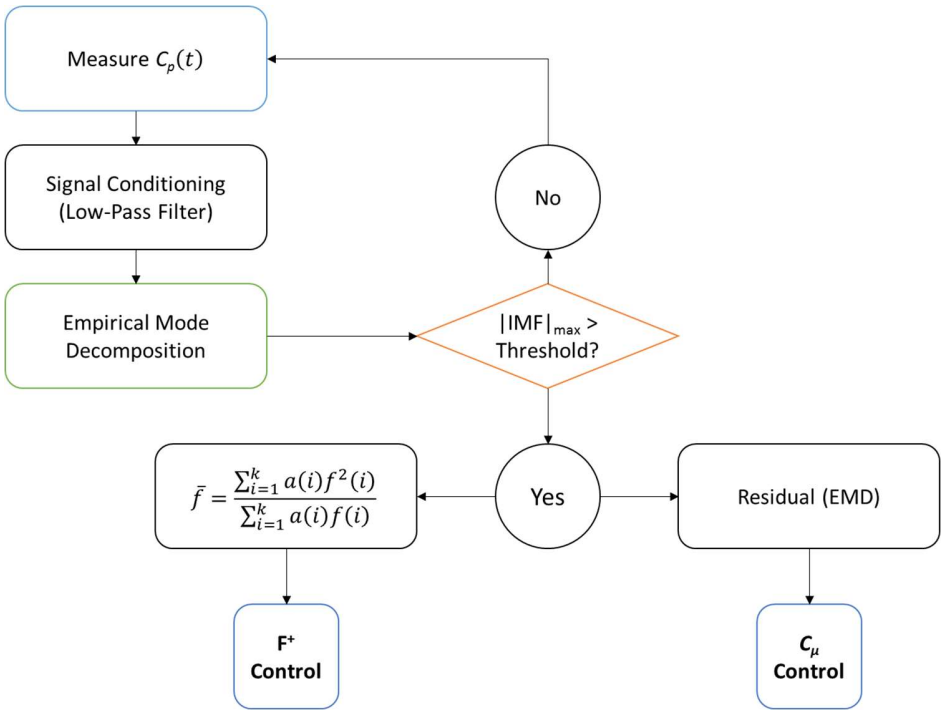

Fig. 2.17 Diagram of signal processing in closed-loop separation control.

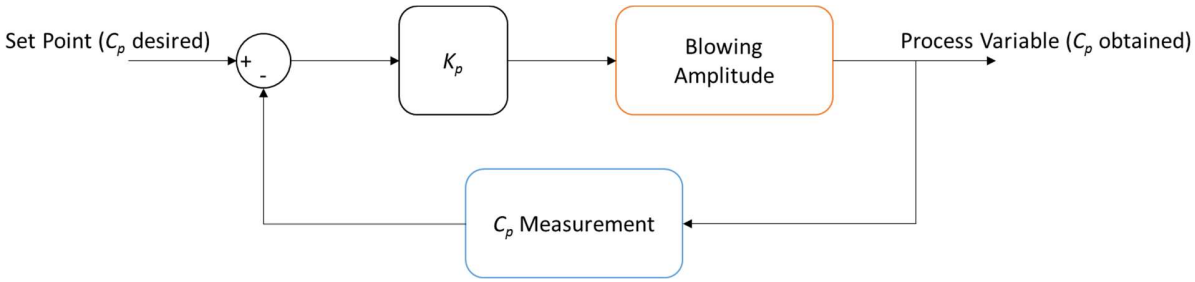

Fig. 2.18 Control scheme for closed-loop flow control.

Chapter 3

Results and Discussion

The results from the experimental investigation are presented in this chapter. It includes detailed analysis of the airfoil performance from parametric studies involving three major flow control parameters: blowing amplitude, frequency, and duty cycle. Also presented in this chapter is the design of a closed-loop flow control architecture with real-time actuation amplitude and frequency control capabilities.

3.1 Experimental Validation of NLF 0414 Airfoil

The NLF 0414 model installation was first validated by taking performance measurements of the baseline NLF 0414 airfoil. In this baseline configuration, the flow control system was deactivated and the blowing taps were carefully covered to provide a smooth undisturbed surface for the flow of air around the airfoil. The experimental measurements for the baseline configuration were compared with the results from experiments carried out at the NASA Langley Research Center in 1987, which are reported in the design document for the given airfoil[17]. The results from the present investigation for the baseline airfoil show similar trends with those reported in the NASA document for the NLF 0414 airfoil. Quantitative differences observed between the two sets of measurements are explained in section 3.2.1.

3.2 Open-Loop Experiments

3.2.1 Baseline Flow

When designed, the NLF 0414 airfoil was envisaged to achieve significantly lower cruise drag coefficients than the existing NLF or NACA 6 series airfoils of the time, and yet maintain acceptable maximum lift and stalling characteristics[17]. Thus, the design of the airfoil features an extensive favorable pressure gradient region, which prevents the amplification of Tollmien-Schlichting (TS) waves. This configuration allows the airfoil to maintain a natural laminar flow to about 70% of the chord on both the upper and lower surfaces at $Re_c = 10 \times 10^6$. Moreover, in order to improve $C_{l,max}$ performance, a thicker leading edge is utilized than typical airfoils with extensive laminar flow operating at high Reynolds number (Viken et al.[17]). However, a significant disadvantage of utilizing large regions of favorable pressure gradient required for extensive NLF is the existence of a very rapid pressure recovery close to the trailing-edge region of the airfoil. In order to help lessen the severity of the effects imposed by the aggressive pressure recovery on the boundary layer, a concave-type pressure recovery is utilized. In a concave pressure recovery, the magnitude of the adverse pressure gradient is tapered in order to compensate for the loss in fluid momentum and thus, a decline in the ability of the boundary layer to sustain adverse pressure gradients. The trailing-edge region of the airfoil is designed such that the strongest adverse pressure gradients exist near regions with sufficiently high fluid momentum. In contrast, regions of low momentum fluid further downstream are confronted with increasingly less severe adverse pressure gradients in order to keep the flow completely attached on the airfoil surface across a fixed range of angles of attack. Flow separation is, however, still expected in the rapid pressure recovery regions at off-design conditions in the absence of boundary layer control.

Fig. a) through e) show the C_p distribution around the baseline NLF 0414 airfoil at $\alpha = 2°$, 5°, 7°, 9°, and 13°. The surface flow visualization images are also presented alongside the C_p distributions in order to identify and correlate the flowfield features with the pressure measurements on the surface of the airfoil. The blowing slots away from the proximity of the center span of the airfoil model are excluded from the surface flow visualization images presented in Fig. . This exclusion is justified because of the presence of strong 3D effects close to the tips of the model that are not representative of the flow around a true airfoil. An extensive

favorable pressure gradient region can be easily identified from the C_p distribution at $\alpha = 2°$. A region of concave pressure recovery close to the trailing edge of the airfoil can also be identified from the C_p distribution at $\alpha = 2°$. Boundary layer characteristics are inferred from the shear-stress driven oil-droplet distribution on the airfoil surface as seen in the corresponding flow-visualization images. At $\alpha = 2°$, the flow remains completely attached on the surface of the airfoil since the oil droplets all the way across the chord are displaced downstream from their initial positions. Furthermore, a region of boundary layer transition can also be identified from the surface flow visualization image, shown in Fig. a), by observing two distinct regions of the flowfield on the airfoil separated by the dashed vertical lines at $x/c = 0.75$. The oil droplets downstream of $x/c = 0.75$ are scrubbed away faster than the corresponding droplets upstream of $x/c = 0.75$ indicating a difference in the magnitude of the shear stress on the airfoil surface. The lower magnitude of the shear stress is characteristic of a laminar boundary layer that extends spatially to about 75% of the chord. On the other hand, the higher magnitude of shear stress on the airfoil surface is indicative of stronger momentum mixing due to the presence of a turbulent boundary layer beyond $x/c = 0.75$.

The C_p distribution reaches a plateau near the trailing-edge region at $\alpha = 5°$ (Fig. b)). This observation was attributed to the pressure recovery losses caused by trailing-edge separation and is further substantiated by the surface flow visualization image at $\alpha = 5°$, shown in Fig. b). The oil droplets beyond $x/c = 0.75$ remain secured to their initial positions on the airfoil surface due to exceedingly low magnitudes of the local shear stress, which is associated with flow separation. A leading-edge separation bubble can also be identified in the surface flow visualization image recorded at $\alpha = 7°$ by observing alternate bands of low and high shear stresses (Fig. c)) that is indicative of boundary layer separation and reattachment. The streamwise size of the leading-edge separation bubble diminishes with increasing angle of attack. In contrast, the spatial extent of trailing-edge separation increases with increasing angle of attack and extends to about 40% of the chord at $\alpha = 13°$ (Fig. e)). Furthermore, the region of concave pressure recovery, seen prominently in the C_p distribution at $\alpha = 2°$, is completely absent in the C_p distribution at $\alpha = 13°$.

The effect of the pressure distribution across the chord of the airfoil is reflected in the airfoil performance, shown in Fig. 3.2 at $Re_c = 1 \times 10^6$. In the off-design conditions, beyond $\alpha = 3°$, the separated flow region across the trailing edge of the airfoil effectively decambers the

airfoil, producing a decrease in the lift-curve slope and an increase in pressure drag prior to airfoil stall. The maximum lift coefficient, $C_{l,max}$ is measured to be 1.26 at α = 13°. The airfoil also has a very low drag bucket with the minimum profile drag, $C_{d,min}$ = 0.00905 observed at α = 2°. As previously mentioned in section 3.1, while the results from the present investigation show similar trends with those reported in the NASA document, there are finite quantitative differences. These quantitative differences can be explained in terms of the difference in *Re*, which for the present investigation is 10 times lower than the value reported in Viken[17]. It is safe to assume that an increase in the Re_c will increase $C_{l,max}$ and further reduce $C_{d,min}$, which would likely bring the performance measurements from the current study at par with the aforementioned report. More importantly, however, the existence of a well-defined trailing-edge separation heightens the motivation to introduce active flow control schemes in an effort to improve the performance of the airfoil beyond its design angle-of-attack range.

3.2.1.1 Unsteady Surface Pressure Measurements

The PSDs of the NLF 0414 C_p at x/c = 0.9 on the upper surface for various angles of attack up to stall are shown in Fig. 3.3 a). For clarity, the amplitude of each PSD has been multiplied by a factor of ten with respect to the PSD at the previous angle of attack. It should be noted that several of the narrow-band peaks in Fig. 3.3 a) are the result of structural modes of the airfoil model and the angular frequency of the rotation of wind tunnel fan which, from the RPM, was found to occur in integral multiples of 50Hz. At α = 8°, a wide band of frequencies are amplified in the spectral content of unsteady C_p, indicating the presence of a continuous range of scales of unsteady motion with similar energies rather than a single highly amplified vortical structure. In contrast, the PSD at α = 12° is characterized by a relatively narrow band of strongly amplified frequencies with a more distinct central peak than the PSD at α = 8°.

Thus, an increase in the airfoil angle of attack is accompanied by an increase in the spectral energy and a decrease in the bandwidth and the dimensional center frequency of the spectral peak. Using the center frequencies from Fig. 3.3 a), the non-dimensional actuation frequency, F^+_{var} from Eq. 2.51, reduced to a constant value of 0.09 (Fig. 3.3 b)). The center frequencies have been shown in previous studies[41] to correspond to an eigenvalue associated with the maximum amplification rate. Thus, unsteady actuation at F^+_{var} = 0.09 is expected to amplify the natural instabilities in the flow, strengthening the formation and growth of coherent

vortical structures in the shear layer. This augmentation of vortical structures due to unsteady actuation is further expected to enhance mixing between the inviscid flow and the recirculation regions, thereby re-energizing the boundary layer and alleviating the undesirable effects of separation across the trailing edge of the airfoil.

3.2.2 Blowing Amplitude Parametric Investigation

3.2.2.1 Performance Measurements

The performance of the NLF 0414 airfoil was first evaluated for a range of non-dimensional jet momentum (or blowing) coefficients, C_μ. It should be stated here that the sensitivity of the airfoil performance to a change in one actuation parameter can only be determined by holding all other control parameters constant. Thus, to understand the effects of C_μ, the duty cycle (DC) was held constant at a value of DC = 50% and actuation frequency at F^+_{var} = 0.09. The value of C_μ between two different data sets was varied by changing the input pressure setting in the pressure regulator. The resulting lift, drag and quarter-chord pitching moment characteristics of the airfoil are presented in Fig. 3.4**.**

The lift generated by the airfoil was found to increase monotonically with increasing magnitude of C_μ, as the introduction of a higher momentum jet into the boundary layer provides further assistance in the pressure recovery across the trailing-edge region. Similar trends are also observed for the drag polar and quarter-chord pitching moment characteristics of the airfoil. These performance measurements are corroborated by measurements of the pressure distribution across the chord of the airfoil at α = 2°, 5°, 7°, 9°, 11°, and 13° for two different C_μ settings, presented in Fig. 3.5. The no blowing C_p contour is also presented in Fig. 3.5 for comparison. Since the flow is completely attached over the airfoil surface, the C_p contours are largely similar for all of the actuated cases at α = 2°. However, for α = 5°, 7°, 9°, 11°, and 13°, actuation at the higher momentum coefficient promotes greater trailing-edge pressure recovery and stronger leading-edge suction, which results in a higher magnitude of total lift that is generated by the airfoil. Although, the results are consistent with our understanding of boundary layer control, they are classically well understood and provide minimal additional understanding into the performance effects beyond what is readily available in the literature.

3.2.3 Actuation Frequency Parametric Investigation

3.2.3.1 Performance Measurements

The effects of a range of non-dimensional actuation frequencies, $F^+ = 0.25$, 0.5, 1, 2, and $F^+_{var} = 0.09$ on the performance of the NLF 0414 airfoil model is shown in Fig. 3.6 for $Re_c = 1 \times 10^6$. As discussed previously, in order to compare the effects of F^+, the results were obtained at a constant $C_\mu = 0.25\%$ and duty cycle, $DC = 50\%$. Thus, any perceived differences in the performance should originate solely from the variation of actuation frequencies. Performance measurements of the airfoil with steady blowing at the same C_μ, as well as the unactuated case, are also included in Fig. 3.6 for comparison.

As discussed briefly in section 3.2.2.1, the flow around an NLF 0414 airfoil is attached all the way across the chord over the upper surface when operated within the design limits. As such, no significant differences in the lift and drag of the airfoil are observed when flow control is utilized below $\alpha = 3°$. Improvements in the lift generated by the airfoil due to actuation begin to emerge beyond $\alpha = 3°$, where trailing-edge separation was observed to affect the performance of the unactuated model. Actuation at and around the center frequency, $F^+_{var} = 0.09$, is seen to produce significant improvements in the lift as high as 15% as compared to the lift generated by the airfoil in the absence of blowing. This observation reinforces the hypothesis of a resonance mechanism with the natural instabilities in the flow, which can be targeted in order to achieve improved mixing between the potential flow and near-wall regions. This trend is also reflected in the pitching moment characteristics of the airfoil about the quarter-chord which increases significantly in magnitude due to pressure recovery at the trailing edge. Actuation at $F^+ = 0.25$ and $F^+ = 0.5$ are also observed to produce very similar increments in lift as $F^+_{var} = 0.09$, except at the higher angles of attack. Actuation at $F^+ = 0.5$ is in fact observed to produce a slightly higher $C_{l,max}$ than that achieved with an $F^+_{var} = 0.09$ actuation. At moderate to high angles of attack ($8° < \alpha \leq 13°$), all of the pulsed blowing cases are found to perform better than steady actuation. It is also interesting to observe that while $C_{l,max}$ varies between the different blowing cases, there is minimal change in the angle of attack at which the airfoil stalls. This observation may be explained through the location of the separation point, which at the extreme angles of attack moves too far upstream for the actuation at $x/c = 0.75$ to bring about any further separation control and performance enhancement.

Drag on the airfoil model remains largely unaffected by variations in actuation frequency, although a distinct reduction in C_d of the order of 5-6% can be identified when compared to the unactuated case in Fig. 3.6 due to stronger pressure recovery at the trailing-edge region of the airfoil. Pressure drag forms a more dominant component of the total drag on objects with stronger bluff body characteristics such as a cylinder in cross-flow or for airfoils at post-stall angles of attack. As such, a reduction in total drag due to pressure recovery is expected to be significantly higher in magnitude for the latter in contrast with the NLF airfoil used in the present study.

Fig. 3.7 presents a comparison of the C_p distributions at α = 2°, 5°, 7°, 9°, 13°, and 15° for no blowing, steady blowing and F^+_{var} = 0.09. As discussed previously, the flow remains attached all the way across the chord at α = 2° and as such no discernable differences can be observed in the C_p distributions between the actuated and the unactuated cases. On the other hand, for α = 5°, 7°, and 9°, actuation at F^+_{var} = 0.09 produces a strong pressure recovery across the trailing-edge region which further promotes stronger suction near the leading edge of the airfoil. This phenomenon is a well-known characteristic of low-speed flows governed by elliptic partial differential equations wherein information travels almost instantaneously in all directions.[42] The re-establishment of the suction peak leads to significant gains in lift at low to moderate angles of attack. At α = 13°, the pressure recovery at the trailing-edge region is largely diminished and the C_p distribution is mostly indistinguishable from the steady and no blowing cases. However, actuation at F^+_{var} = 0.09 is still found to produce greater suction at the leading-edge region and thus, a higher value of C_l in comparison with the steady and no blowing cases. A plateau in the growth of suction peak is observed in the C_p distribution for the actuated and the unactuated cases at α = 15°. Thus, the movement of the separation point further upstream dramatically reduces the performance gains brought about by flow actuation, rendering the process of flow control at α > 13° inefficient.

3.2.3.2 Particle Image Velocimetry Measurements

The time-averaged PIV velocity fields, along with the *z*-component vorticity fields are presented in Fig. for the no blowing, steady blowing, F^+ = 0.25, F^+ = 1, F^+ = 2, and F^+_{var} = 0.09 cases. The vector fields for each of these cases are processed from over 3000 raw image pairs. In Fig. , the no-blowing case corresponds to subplots a) and b), steady blowing corresponds to c)

and d), $F^+ = 0.25$ corresponds to e) and f), $F^+ = 1$ corresponds to g) and h), $F^+ = 2$ corresponds to i) and j) and $F^+_{var} = 0.09$ corresponds to subplots k) and l). The region of flow recirculation that exists near the trailing-edge of the airfoil without flow control is largely absent from the mean velocity fields presented in Fig. for the $F^+ = 0.25$, $F^+ = 1$, $F^+ = 2$ and $F^+_{var} = 0.09$ cases. This observation clearly demonstrates the improved effectiveness of unsteady actuation in comparison with steady blowing for a fixed C_μ. Furthermore, actuation at $F^+ = 0.25$ and $F^+_{var} = 0.09$ is observed to promote stronger alleviation of trailing-edge separation in comparison with the remaining unsteady actuation cases investigated using PIV. The separated shear layers for $F^+ = 0.25$ and $F^+_{var} = 0.09$ are observed to be closer to the surface of the airfoil near the trailing edge, with a smaller recirculation region, as compared to the other actuation frequencies. This higher level of effectiveness is further substantiated by the presence of higher concentrations of vorticity, identified by a more sizeable region of saturated gridpoints near the surface of the airfoil for the $F^+ = 0.25$ and $F^+_{var} = 0.09$ cases. The higher vorticity concentration is indicative of greater mixing of the flow and a more effective alleviation of the separated flow region.

In addition to the mean flowfield, PIV measurements were also acquired with the velocity field interrogations locked in phase with the actuation cycle for $F^+_{var} = 0.09$, $F^+ = 1$, and $F^+ = 0.25$. These measurements were acquired across eight equally-spaced time intervals at $\alpha = 7°$. The velocity fields were processed from over 1000 image pairs at each of the eight temporal gridpoints, effectively eliminating any non-periodicity in the flowfield from the processed images. A comparison of the velocity fields and the vorticity contours for the $F^+_{var} = 0.09$ and $F^+ = 1$ cases is presented in Fig. and Fig. , respectively, where subplots a), c), e), g), i), k), m), o) correspond to eight cycles of phase for $F^+_{var} = 0.09$ and b), d), f), h), j), l), n), p) are similarly the eight cycles of phase for $F^+ = 1$. The velocity and vorticity fields for the $F^+ = 0.25$ case are presented separately in Fig. . Similar to the $F^+_{var} = 0.09$ and $F^+ = 1$ cases, subplots (a), b)), (c), d)), (e), f)), (g), h)), (i), j)), (k), l)), (m), n)) and (o), p)) in Fig. correspond to the velocity fields and vorticity contours for eight cycles of phase for $F^+ = 0.25$. Since a duty cycle of 50% was used, the first four contours correspond to phases $\varphi = 0°$, 45°, 90° and 135°, where the blowing system was active. The remaining contours correspond to the phases φ =180°, 225°, 270°, and 315°, during which the blowing system was switched off. These phase-locked measurements provide detailed insights into the underlying mechanism responsible for alleviating flow separation due to periodic excitation.

Regions of localized vorticity are immediately identified in the *z*-component phase locked vorticity contours for all of the actuated cases shown in Fig. and Fig. . The motion of these vortical structures produce ripples in the shear layer as identified by arrows in the phase-locked velocity contours presented in Fig. and Fig. . The formation of these ripples has been discussed previously by Packard et al.[10] as an interaction of the high momentum fluid from the potential flow region with the low momentum fluid in the shear layer. This interaction causes the low-momentum fluid in the shear layer to be displaced downstream resulting in the formation of an undulation. This ripple effect is however, more prominent for the F^+_{var} = 0.09 and F^+ = 0.25 cases, which is indicative of stronger entrainment of high momentum fluid from the inviscid region. All of the vorticity contours are also characterized by strong, temporally persistent swaths of localized vorticity due to large gradients of the streamwise velocity component along the *y*-axis. These regions of high vorticity are seen to originate from the far upstream end of the PIV interrogation window, close to the point of separation, and extend almost 60-65 mm spatially downstream for the F^+_{var} = 0.09 and F^+ = 1 cases and almost 30 mm spatially downstream for the F^+ = 0.25 case.

The formation and evolution of the vortices for the case in which actuation was performed at F^+_{var} = 0.09 is only slightly different from the formation of such structures produced with an F^+ = 1 periodic excitation. On the other hand, the dynamics of the evolution of vorticity for F^+ = 0.25 is distinctly different from the F^+_{var} = 0.09 and F^+ = 1 cases and will be discussed subsequently. At the onset of actuation, φ = 0°, remnants from the previous actuation cycle in the form of two distinct vortical structures, numbered 1 and 2, are identified in the vorticity contours for the F^+ = 1 case (Fig. b)). This observation of multiple vortical structures is in contrast with F^+_{var} = 0.09 where only a single, yet significantly stronger structure, can be identified in the shear layer (number 1 in Fig. a)). Further down the current actuation cycle at φ = 180°, new regions of localized vorticity, identified by vertical arrows in subplots i) and j) of Fig. , are observed to emerge from the shear layer for both F^+_{var} = 0.09 and F^+ = 1. Furthermore, for F^+ = 1, minor traces of the vortical structure from the previous actuation cycle are observed to persist near the airfoil trailing edge in its entirety. In contrast, the vortical structure from the previous actuation cycle for F^+_{var} = 0.09 is found to have almost convected past the trailing edge of the airfoil. Thus, for F^+_{var} = 0.09, the time between the formation of vortical structures appears to match the convective time scale of the flow. This effect is interesting to note, since a

value of $F^+ = 1$ is intended to allow the actuation time scale to match the convective time-scale of the flow. However, vortices formed in separated shear layers typically do not convect at the freestream velocity,[43] causing there to be multiple vortical structures present in the flowfield near the trailing-edge of the airfoil at any given instance for the $F^+ = 1$ case.

In an effort to better identify and compare the vortex dynamics, swirl strength of the velocity field were calculated for each of the eight cycles of phase for $F^+_{var} = 0.09$ and $F^+ = 1$. The phase-locked swirl strength contours for the $F^+_{var} = 0.09$ and $F^+ = 1$ cases are presented in Fig. where, subplots a), c), e), g), i), k), m), o) correspond to $F^+_{var} = 0.09$ and subplots b), d), f), h), j), l), n), p) correspond to $F^+ = 1$. Consistent with the flowfield characteristics observed in the vorticity contours, the vortical structures generated in successive cycles of actuation are found to be more closely spaced in the swirl strength contours for $F^+ = 1$, as compared to $F^+_{var} = 0.09$. Moreover, for $F^+_{var} = 0.09$, the time scale of actuation is clearly observed to match the convective time scale of the vortices in the flow. The closer spacing of the vortical structures as a result of higher dimensional frequency of actuation for $F^+ = 1$ promotes stronger interactions leading to an onset of merging process between the pair of initially coherent vortical structures. A co-rotating vortex merging process is associated with strong dissipation of vorticity and an elliptic-type deformation of the vortex cores.[44] These characteristics are immediately identified in the swirl strength contours for $F^+ = 1$ at $\varphi = 0°$, 45°, and 90°. The vortical structures close to the trailing edge of the airfoil for $F^+ = 1$ are observed to gradually coalesce, deform and dissipate in strength due to the mutual interactions. Such an effect is not observed for $F^+_{var} = 0.09$ due to the larger spacing between the vortical structures that inhibits any perceivable mutual interactions. The strong dissipation of vorticity for $F^+ = 1$ results in weaker momentum entrainment near the trailing-edge region of the NLF 0414 in contrast with forcing at $F^+_{var} = 0.09$, leading to an inferior lift performance of the former in comparison with the latter. This inferior performance is reflected in the mean position of the shear layer which for $F^+_{var} = 0.09$ was observed, in Fig. , to be closer to the surface of the airfoil near the trailing-edge than $F^+ = 1$.

Unlike $F^+_{var} = 0.09$ and $F^+ = 1$, a remarkably different mechanism governing the formation of coherent vortical structures is observed for the $F^+ = 0.25$ case, presented in Fig. . This difference is evident by the state of the flow at the onset of actuation ($\varphi = 0°$) for $F^+ = 0.25$, which is characterized by a non-localized distribution of vorticity along the shear layer close to

the surface of the airfoil. This broad vorticity distribution is in contrast with the $F^+_{var} = 0.09$ and $F^+ = 1$ cases, which were characterized by locally-confined vortical structures from the previous actuation cycle. At $\varphi = 90°$, the distribution of vorticity in the shear layer for $F^+ = 0.25$ is observed to roll up into a single coherent vortical structure, resembling an interface roll up process that is characteristic of the Kelvin-Helmholtz instability. This coherent structure is observed to amplify in size as it convects further downstream and eventually past the trailing-edge of the airfoil at $\varphi = 225°$. Upon convection of the vortex past the trailing-edge, the shear layer is observed to gradually relax back to the original state seen at the onset of the actuation cycle. The roll up of the shear layer into a coherent structure and the subsequent amplification are responsible for momentum entrainment across the potential flow and recirculation regions and the alleviation of separation observed when actuating at $F^+ = 0.25$.

3.2.4 Duty Cycle Parametric Investigation

3.2.4.1 Performance Measurements

Fig. 3.13 depicts the variation in the lift, drag and quarter-chord pitching moment coefficient for three different duty cycles, DC = 30%, 50%, and 70%. As in the previous two cases, the sensitivity of the airfoil performance to a change in DC is determined by holding a constant $C_\mu = 0.25\%$ and an $F^+_{var} = 0.09$. The results reveal a monotonic increase in the lift and the magnitude of the pitching moment of the airfoil with decreasing duty cycle. Consistent with the results of F^+ modulation, a variation of the duty cycle produces no visible change in the lift of the airfoil below a threshold value of the angle of attack, $\alpha = 3°$, during which separation at the trailing edge is either completely absent or highly insignificant. The C_p distributions at $\alpha = 2°$, 5°, 7°, 9°, 11°, and 13°, shown in Fig. 3.14, are observed to be very similar in their profile for the range of actuation duty cycles considered in this parametric investigation. However, small but significant differences in the leading edge suction can be resolved upon closer inspection of the C_p contours. The C_p distribution at the lower duty cycles are characterized by stronger levels of suction near the leading edge in comparison with the C_p distributions at the higher duty cycles. The integrated effects of these differences are reflected in the difference in the airfoil performance observed due to modulation in the duty cycle of actuation.

3.2.4.2 Particle Image Velocimetry Measurements

The PIV velocity and z-component vorticity fields with varying DC of actuation are presented in Fig. 3.15. In Fig. 3.15 subplots a) and b) correspond to DC = 30%, subplots c) and d) correspond to DC = 50% and subplots e) and f) correspond to DC = 70%. From the velocity and vorticity contours, it is observed that for the case in which actuation was performed at DC = 30%, the region of flow recirculation is spatially smaller, with a higher concentration of near-wall vorticity than the case in which actuation was performed at DC = 50%. Actuation at DC = 50% is, in turn, observed to have a smaller recirculation region and a higher near-wall vorticity concentration in comparison with DC = 70%. Thus, consistent with the performance measurements presented in section 3.2.4.1, alleviation of trailing-edge separation becomes progressively stronger as the duty cycle of actuation is decreased with the strongest alleviation observed for DC = 30%.

An explanation for stronger alleviation of separation at lower duty cycles is implicitly contained in the definition of non-dimensional jet momentum coefficient C_μ. In the present study, the calculation of C_μ was based on an average momentum flux across a fixed data acquisition time, rather than across the "on" time of a single duty cycle. Thus, the definition of C_μ used in the current study represents a total energy factor over a certain period of actuation, providing a more realistic evaluation of power requirements for practical applications. Therefore, under the present definition, a low duty cycle actuation is expected to have higher blowing amplitude than a high duty cycle actuation for a constant average momentum flux since it is associated with a longer "off" time for a given period. Improved performance at lower duty cycle is therefore a trivial result of actuating at higher blowing amplitude, but across a shorter portion of the period of actuation.

3.3 Surface Flow Visualization

Fig. 3.16 provides a comparison of the surface flow visualization images recorded at α = 5°, 7°, and 13° for the NLF 0414 airfoil with actuation at F^+_{var} = 0.09 and DC = 50%, as well as the no blowing configuration. As discussed previously, only the slots in the proximity of the center span of the model are presented in the surface flow visualization images. For the cases in which flow control was inactive, regions of low shear stresses can be identified beyond the separation point marked by dashed vertical lines (Fig. 3.16 a)), where the oil droplets are not

scrubbed away from their initial position on the airfoil surface. In contrast, several distinct flow features can be seen on the surface of the airfoil in the presence of actuation, as indicated in Fig. 3.16 b). The exit of the jet from the blowing slots into the surrounding fluid is an example of a turbulent jet-cross flow interaction that has been studied extensively in the past.[45,46] Such flows are usually characterized by four different near-field vortical structures,[46] the distorted shear layer vortices at the circumference of the deflected jet, a counter-rotating vortex pair that dominates the structure of the jet, horse-shoe vortices in the crossflow, and secondary vortices in the wake of the jet.

The flow over the upper surface of the airfoil immediately upstream of the blowing slots is similar in its behavior to a 2D stagnation flow. In the present context, a high-momentum jet exiting the blowing slot acts as a blockage in the path of the crossflow, forcing it to circumnavigate around the slot and producing a pattern of streamlines on the surface that is highlighted in Fig. 3.16 b). The vortices in the wake of the jet, immediately downstream of the slot are also easily identified in these images. Since the flow structures and interactions primarily occur in the off-body flowfield, surface-oil flow visualization provides limited understanding of these complex vortical structures. However, further downstream of the blowing slots, traces of a counter-rotating vortex structure can be identified in the oil flow pattern on the surface. Such out of plane 3D features of the interaction between the boundary layer and the blown jet were not resolved in the planar PIV measurements. The traces of the vortical structures left behind on the surface of the airfoil become increasingly weaker as the angle-of-attack is increased (Fig. 3.16 f)). This weakening of the surface trace indicates that the vortical structures in the shear layer are formed progressively farther away from the surface of the airfoil as the separation point moves further upstream upon increasing the angle-of-attack.

3.4 Closed-Loop Experiments

3.4.1 Actuation Frequency Control

As discussed in section 2.7.2, the unsteady C_p measurements at $x/c = 0.90$ were used to regulate the F^+ and C_μ of the pulsed blowing system in a closed-loop architecture. Initially, only frequency control was performed, and the flow control parameters were set to maximize the supply pressure to the AFC system, which corresponded to $C_\mu = 0.3\%$. The resulting

performance measurements are presented in Fig. 3.17 for the airfoil with closed-loop frequency control, with the open-loop control results at $F^{+}_{var} = 0.09$ provided as a reference. From Fig. 3.17, use of the closed-loop control system resulted in similar airfoil lift characteristics as the most effective open-loop control case. The value of $C_{l,max}$ achieved by the closed-loop separation control was also slightly higher than that obtained from open-loop control at post-stall angles of attack.

In order to understand how the EMD algorithm utilizes the flow physics of the trailing-edge separation in order to identify the natural frequency of the shear layer instability, the premultiplied pressure spectra corresponding to $x/c = 0.90$ are presented in Fig. 3.18 for an angle-of-attack range up to stall. Much like in Fig. 3.3 a), the premultiplied spectra presented in Fig. 3.18 have been multiplied by a factor of ten with respect to the spectrum at the previous angle of attack in order to improve the visibility of traits associated with these spectra. The actuation frequencies selected by the EMD algorithm are also provided in Fig. 3.18 using an arrow symbol. It is important to note that these actuation frequencies were identified in real-time by the EMD algorithm, and these EMD-selected frequencies correspond to the same experiment as the closed-loop C_l measurements in Fig. 3.17. From Fig. 3.18, the actuation frequencies from the closed-loop separation control method are consistent with the frequencies of maximum energy in the premultiplied pressure spectra. This bias of the IMF frequencies to the premultiplied spectra has also been observed by Agostini and Leschziner[35] when applying EMD to turbulence simulations.

The ideal lift curve of $C_l = 2\pi\alpha$ is also provided in Fig. 3.17 as a reference. The primary purpose of pulsed blowing on the airfoil model was to alleviate trailing-edge separation, which introduces considerable streamline displacement across the upper surface and a severe decambering of the airfoil. This decambering leads to a distinct decrease in the lift-curve slope from the ideal value of theoretical models. As a result, using AFC to produce attached flow across the airfoil trailing-edge region eliminates the primary viscous decambering effect from the flowfield, bringing the airfoil C_l to within a range that would be expected from theoretical methods. While other viscous effects, such as boundary-layer growth across the airfoil surface, also cause the lift-curve slope of an airfoil to deviate from the ideal theoretical value, these effects on the airfoil C_l are typically far less significant than those caused by separation.

3.4.2 Blowing Amplitude Control

It was observed that the C_p at $x/c = 0.90$ served as a good predictor of the decrease in lift produced at a given angle of attack relative to an ideal, inviscid value. A comparison of the measured lift coefficient during the wind-tunnel experiments and the relative difference in the measured lift coefficient (ΔC_l) from $C_l = 2\pi\alpha$ is presented in Fig. 3.19 a). In comparison, the mean C_p value at $x/c = 0.90$ obtained for a corresponding ΔC_l is presented in Fig. 3.19 b). From Fig. 3.19 b), a linear relationship between C_p at $x/c = 0.90$ and ΔC_l was assumed ($R = 0.983$), such that by prescribing a desired value of C_p, the airfoil C_l can be controlled to within a desired percentage of the ideal value. By providing a state estimator for C_l using C_p at $x/c = 0.90$, control of C_μ could also be included in the closed-loop separation control method.

In an example, the closed-loop separation control method was used to control the C_l of the airfoil model to within a 90%, 85%, and 80% of the ideal value. The resulting airfoil C_l obtained by implementing closed-loop frequency and amplitude control of the pulsed blowing system is presented in Fig. 3.20. From Fig. 3.20 it can be observed that the value of C_l obtained with C_μ control was highly consistent with that corresponding to the desired percentage of the ideal C_l. There are, however, two exceptions to this observation. When the C_μ control saturates to the maximum amplitude achievable by the actuation system, the desired C_l cannot be achieved. As a result, at high angles of attack, the C_l measurements deviate from the desired C_l value that has been prescribed. The second exception is at low angles of attack when C_l is prescribed to be some small percentage (i.e., < 90%) of the ideal value. For example, when setting C_l to be 80% of the ideal value, the AFC system does not engage until 9°, and thus, the measured C_l for $\alpha = 6° - 8°$ is less than the desired value. This undershoot in the measured C_l occurs due to the change in the airfoil C_p distribution produced by AFC. The C_p at $x/c = 0.90$ when AFC is engaged is distinctly different from that when AFC is not engaged, and the C_p threshold that produces $C_l = (0.8)2\pi\alpha$ is not exceeded, even though the measured C_l is less than the desired value. This limitation can be overcome in future studies by employing a switching control system for actuated and non-actuated configurations and more accurately compensating for the small variation in the zero-lift angle of attack between successive performance polars. Despite this shortcoming, the closed-loop separation control method was observed to effectively detect and control trailing-edge separation using a single set of unsteady pressure measurements.

3.5 Chapter 3 Figures

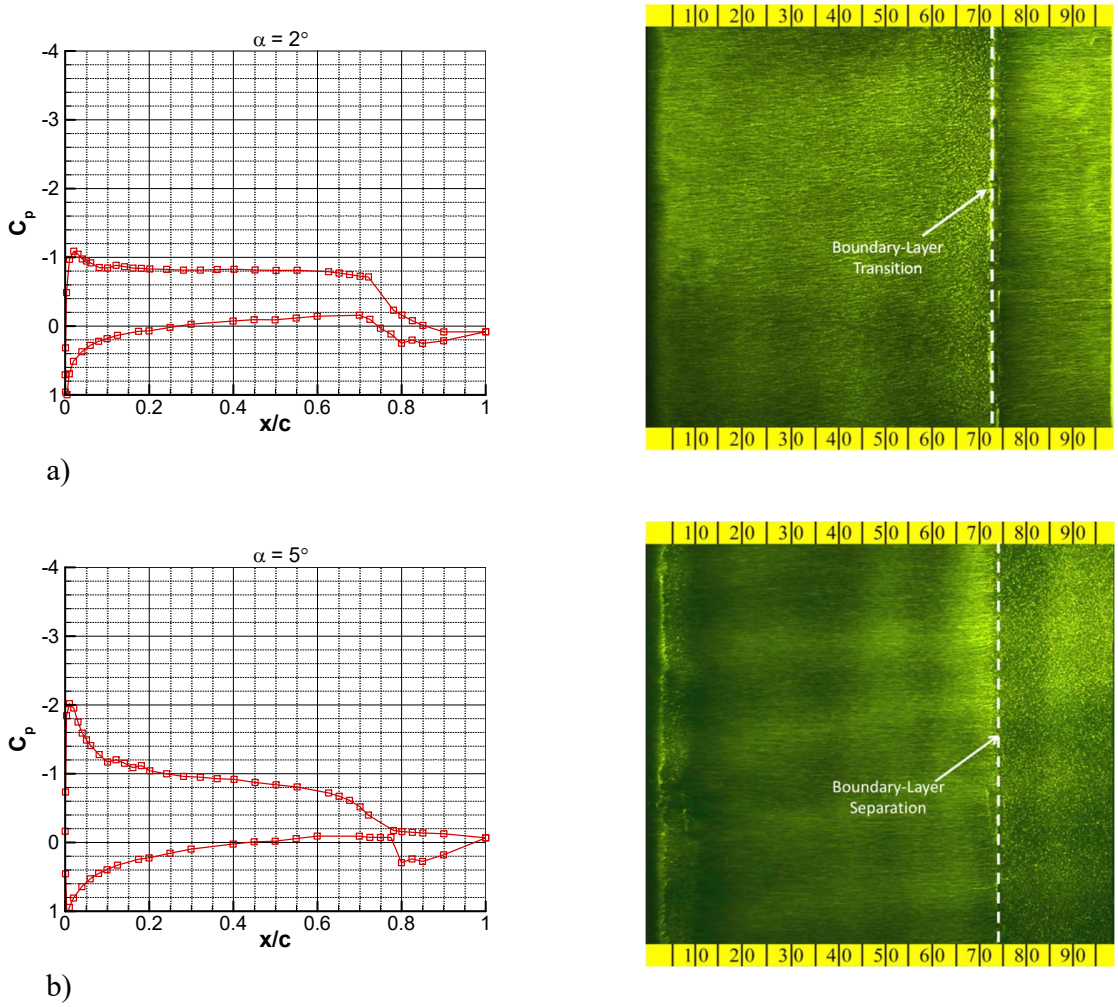

Fig. 3.1 C_p distributions and corresponding surface flow visualization images of the baseline NLF 0414 airfoil at a) α = 2°, b) α = 5°, c) α = 7°, d) α = 9°, and e) α = 13°.

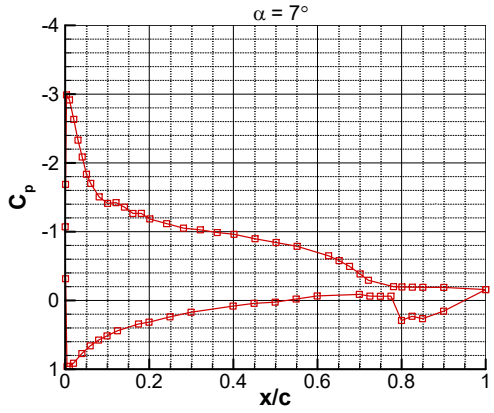

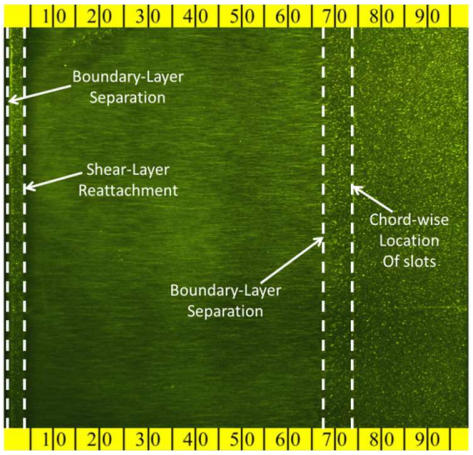

c)

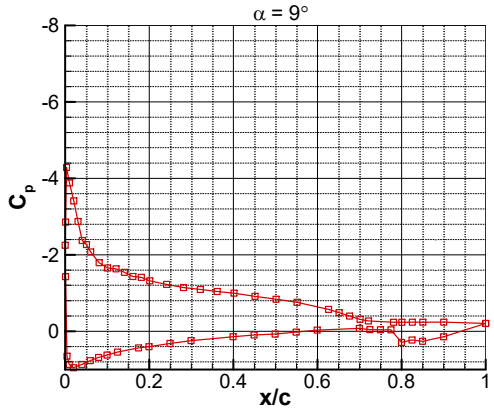

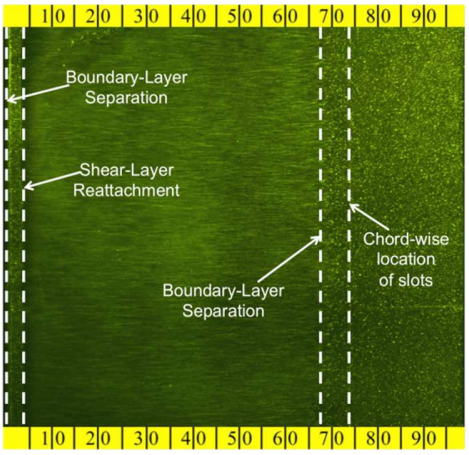

d)

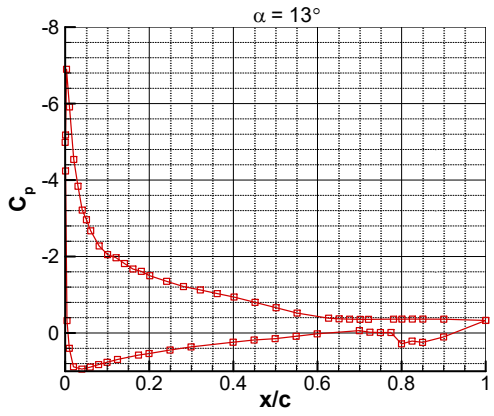

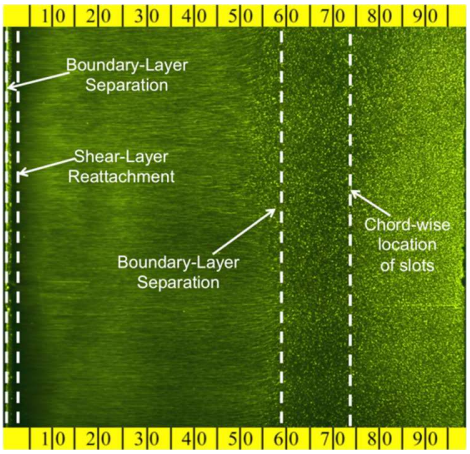

e)

Fig. 3.1 (cont.) C_p distributions and corresponding surface flow visualization images of the baseline NLF 0414 airfoil at a) $\alpha = 2°$, b) $\alpha = 5°$, c) $\alpha = 7°$, d) $\alpha = 9°$, and e) $\alpha = 13°$.

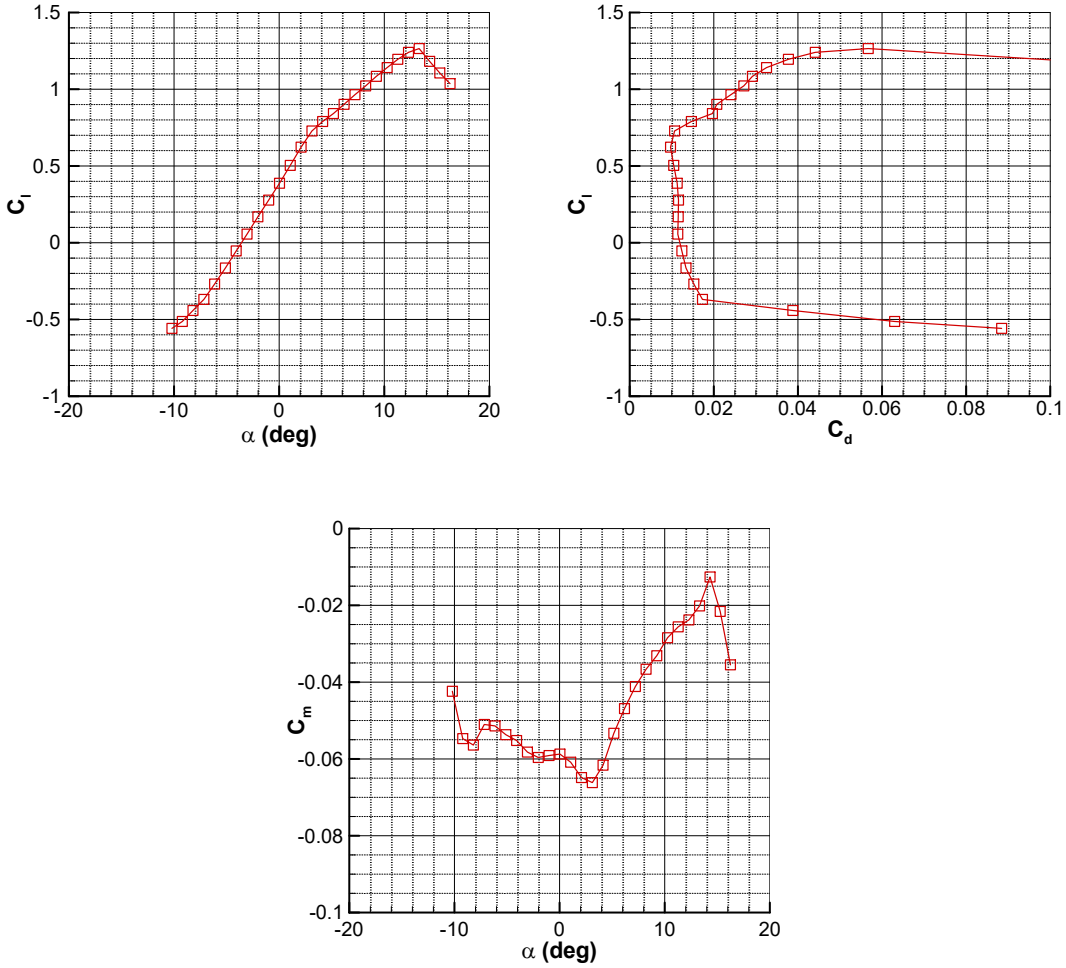

Fig. 3.2 Performance of NLF 0414 airfoil without flow control ($Re_c = 1 \times 10^6$).

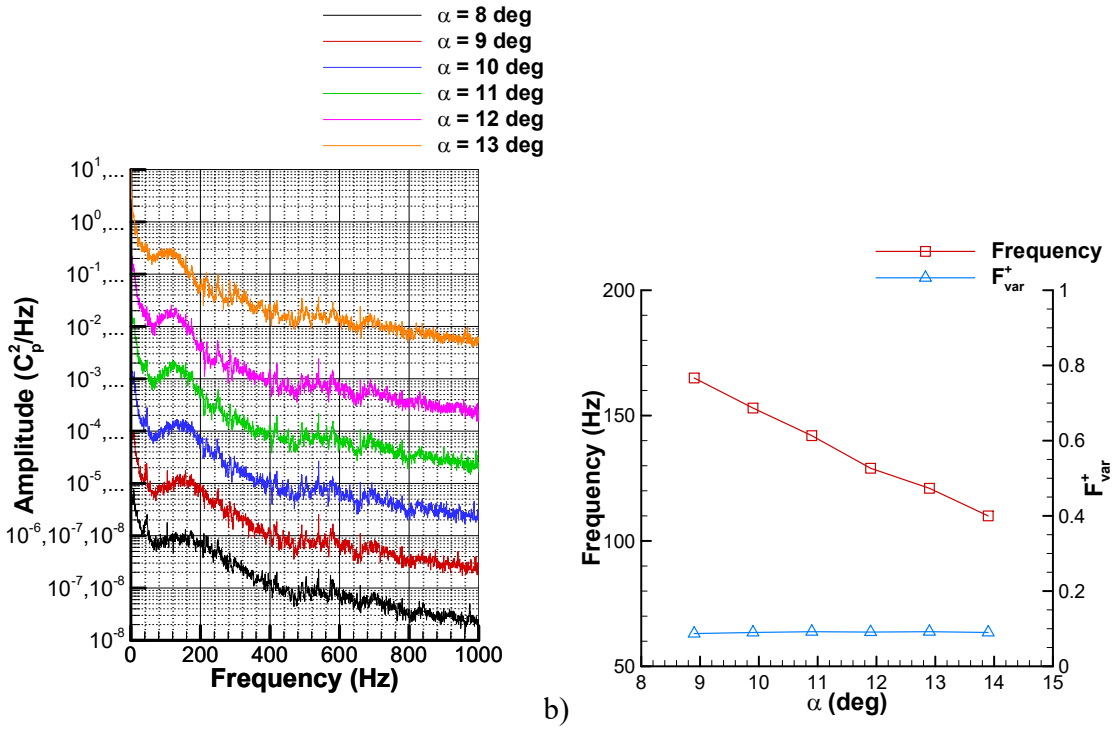

Fig. 3.3 a) Power spectral densities of unsteady C_p measured at x/c = 0.9 with varying angle of attack; b) center frequency scaling of instabilities.

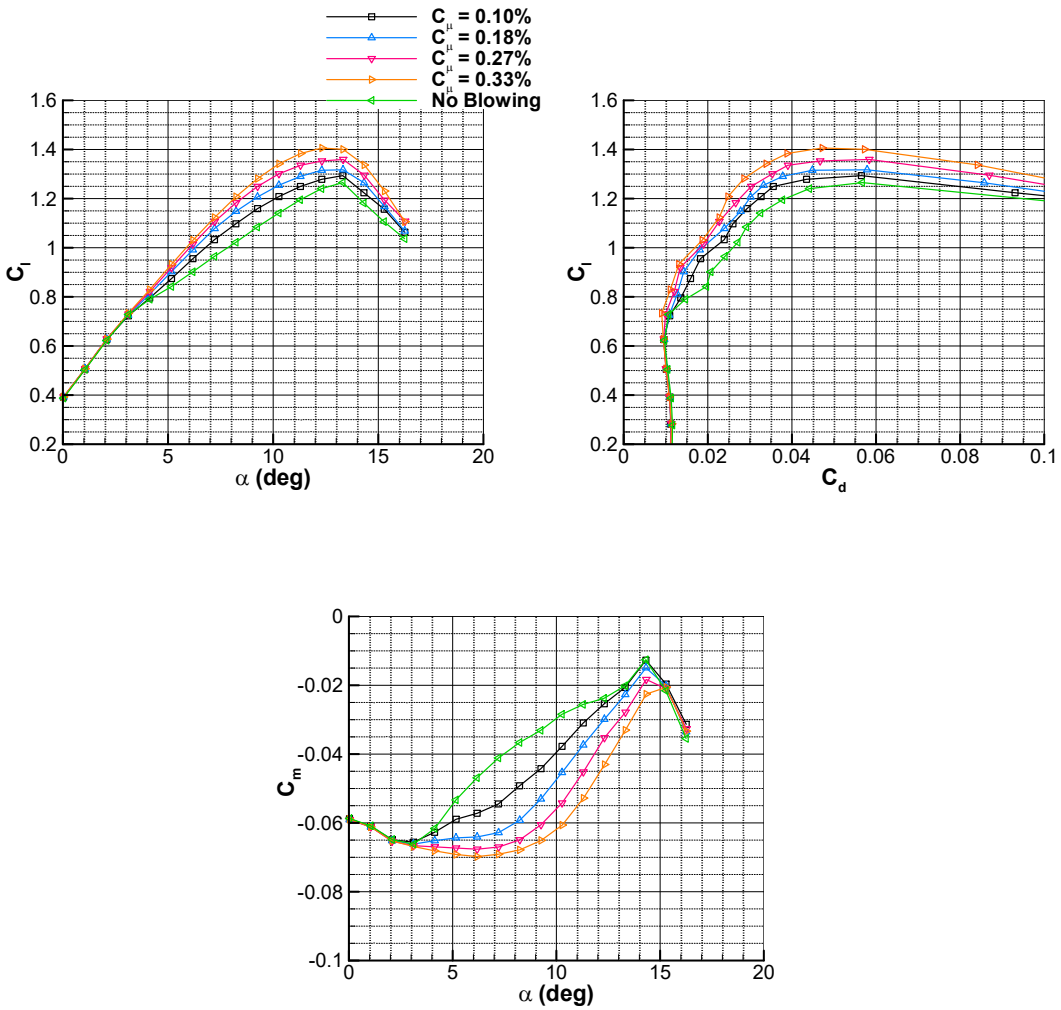

Fig. 3.4 Performance comparison of NLF 0414 for different non-dimensional jet momentum coefficients (C_μ) ($Re_c = 1 \times 10^6$).

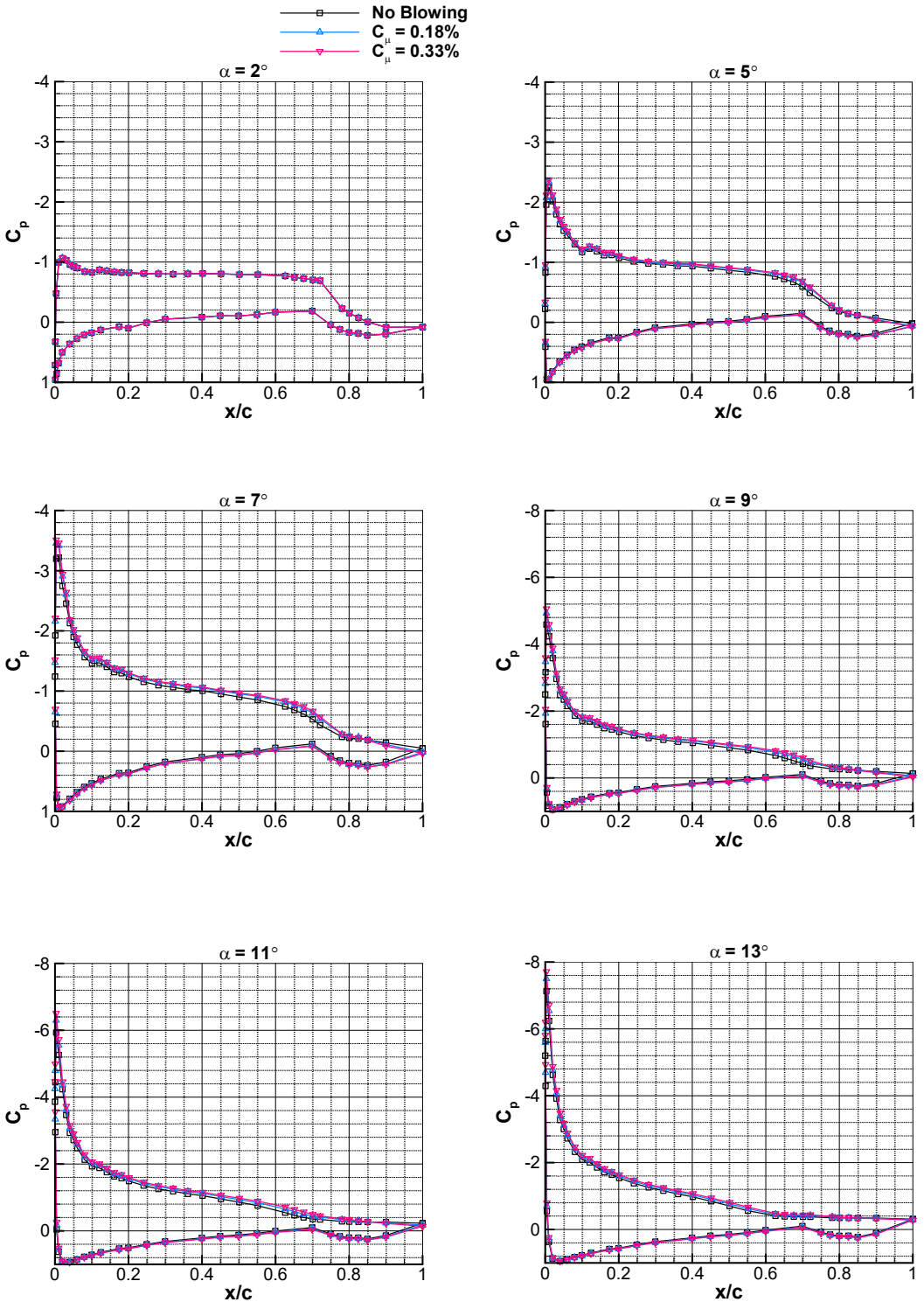

Fig. 3.5 Comparison of the pressure distributions (C_p) around NLF 0414 for two different non-dimensional jet momentum coefficients (C_μ) at α = 2°, 5°, 7°, 9°, 11°, and 13° ($Re_c = 1 \times 10^6$).

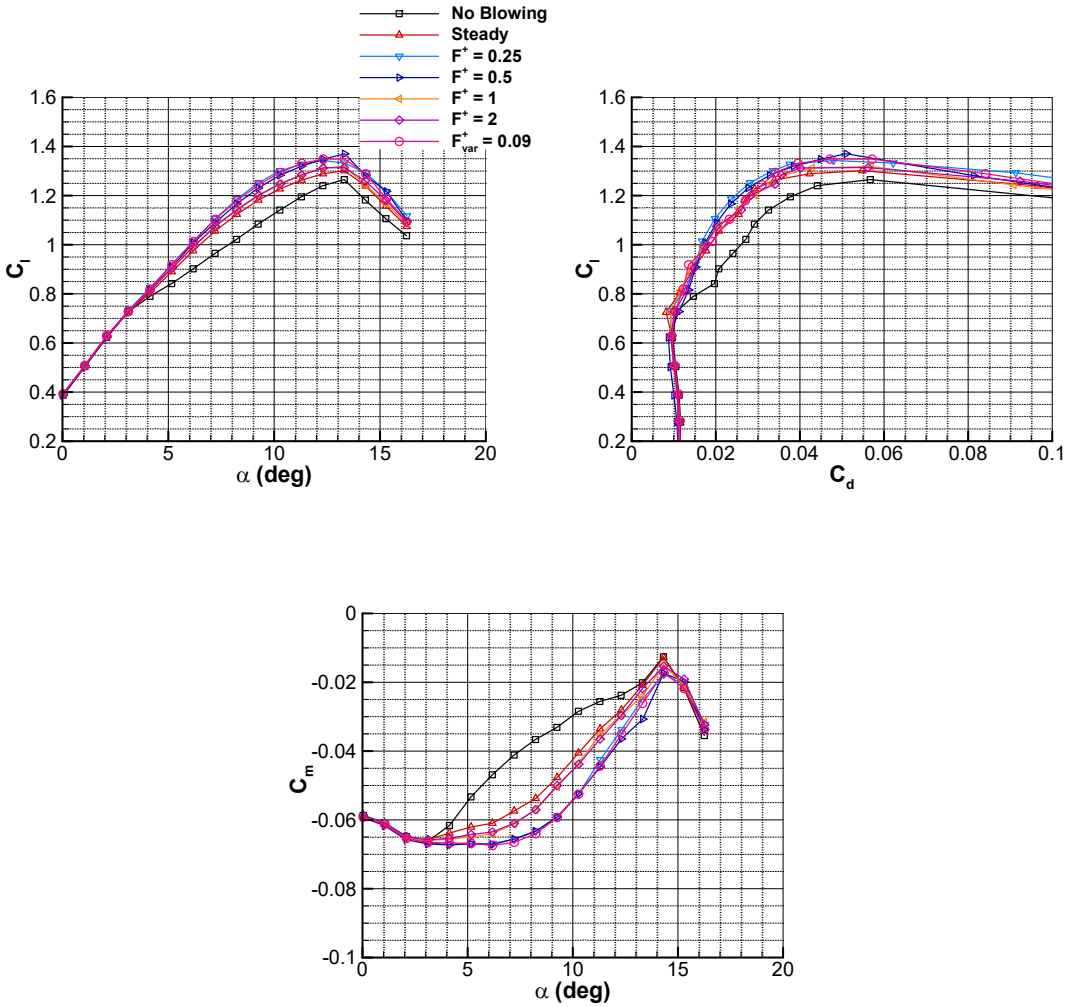

Fig. 3.6 Performance comparison of NLF 0414 for different non-dimensional actuation frequencies (F^+) ($Re_c = 1 \times 10^6$).

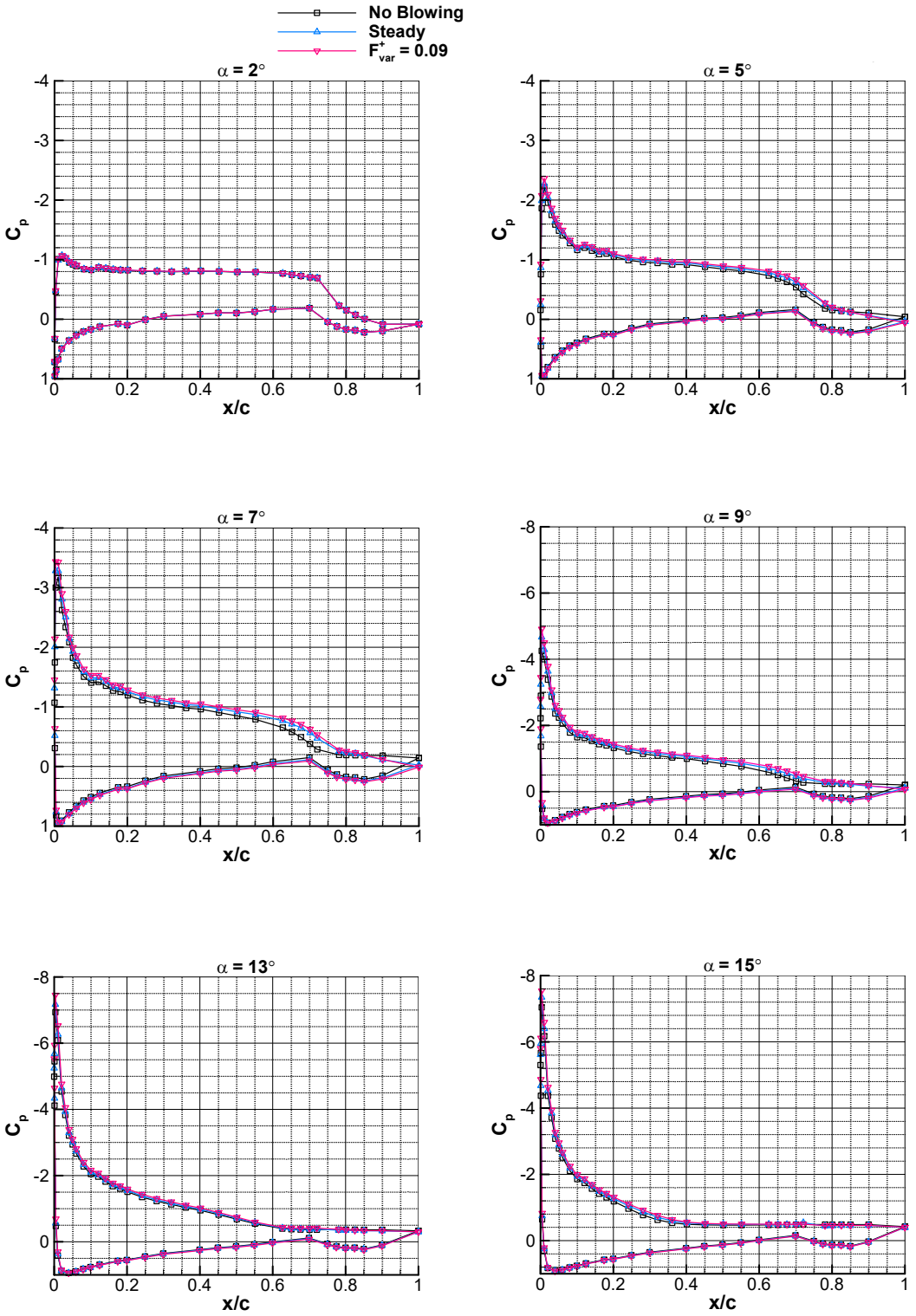

Fig. 3.7 Comparison of the pressure distribution (C_p) around NLF 0414 for no blowing, steady blowing and $F^+ = 0.09$ at $\alpha = 2°, 5°, 7°, 9°, 13°$, and $15°$ ($Re_c = 1 \times 10^6$).

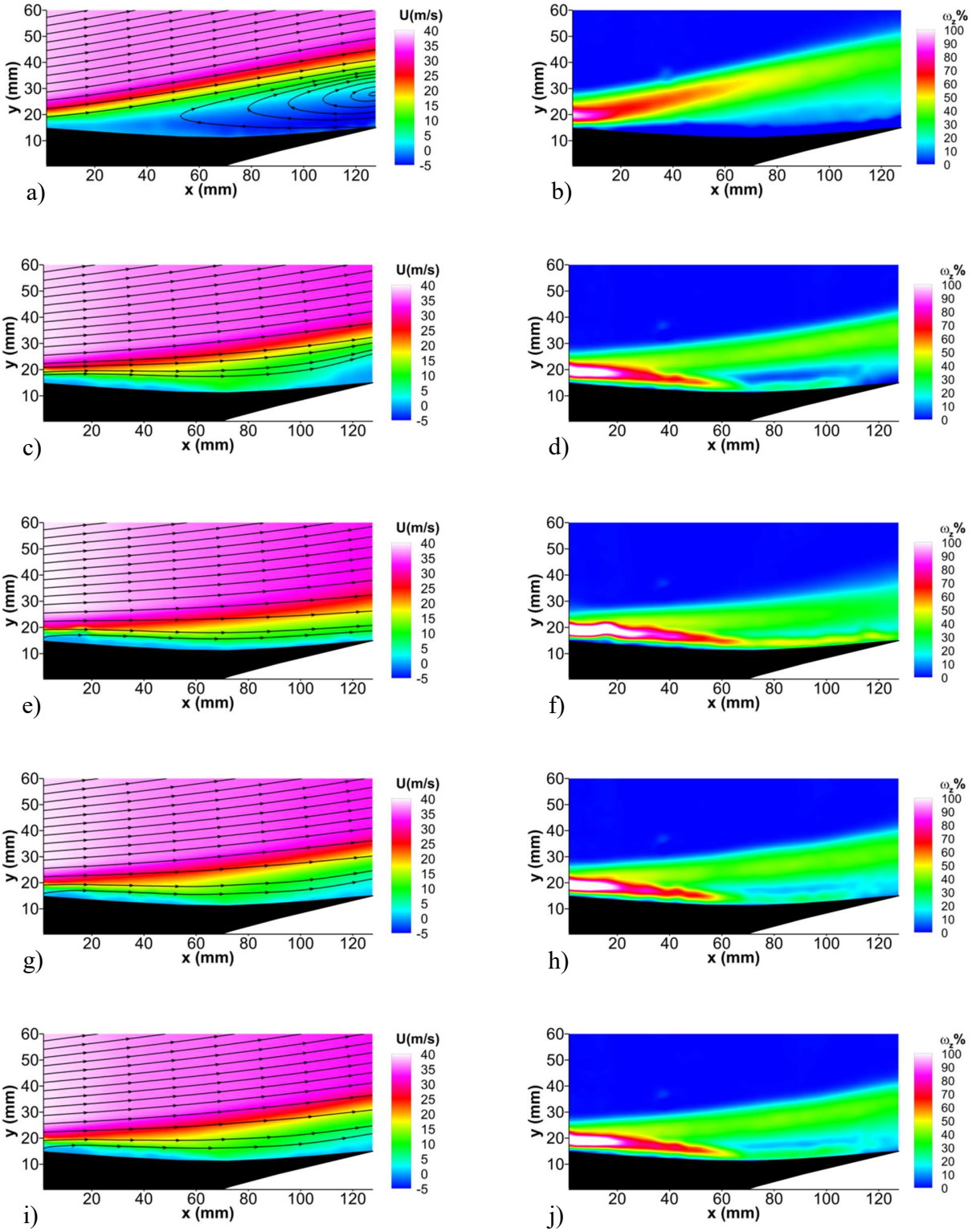

Fig. 3.8 Velocity and vorticity contours across trailing-edge region for no-blowing (a) and b)), steady blowing (c) and (d)), $F^+ = 0.25$ (e) and f)), $F^+ = 1$ (g) and h)), $F^+ = 2$ (i) and j)) and $F^+_{var} = 0.09$ (k) and l)).

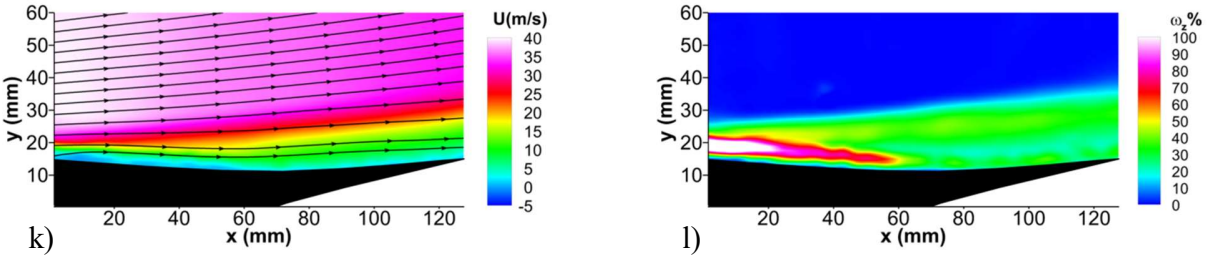

Fig. 3.8 (cont.) Velocity and vorticity contours across trailing-edge region for no-blowing (a) and b)), steady blowing (c) and (d)), $F^+ = 0.25$ (e) and f)), $F^+ = 1$ (g) and h)), $F^+ = 2$ (i) and j)) and $F^+_{var} = 0.09$ (k) and l)).

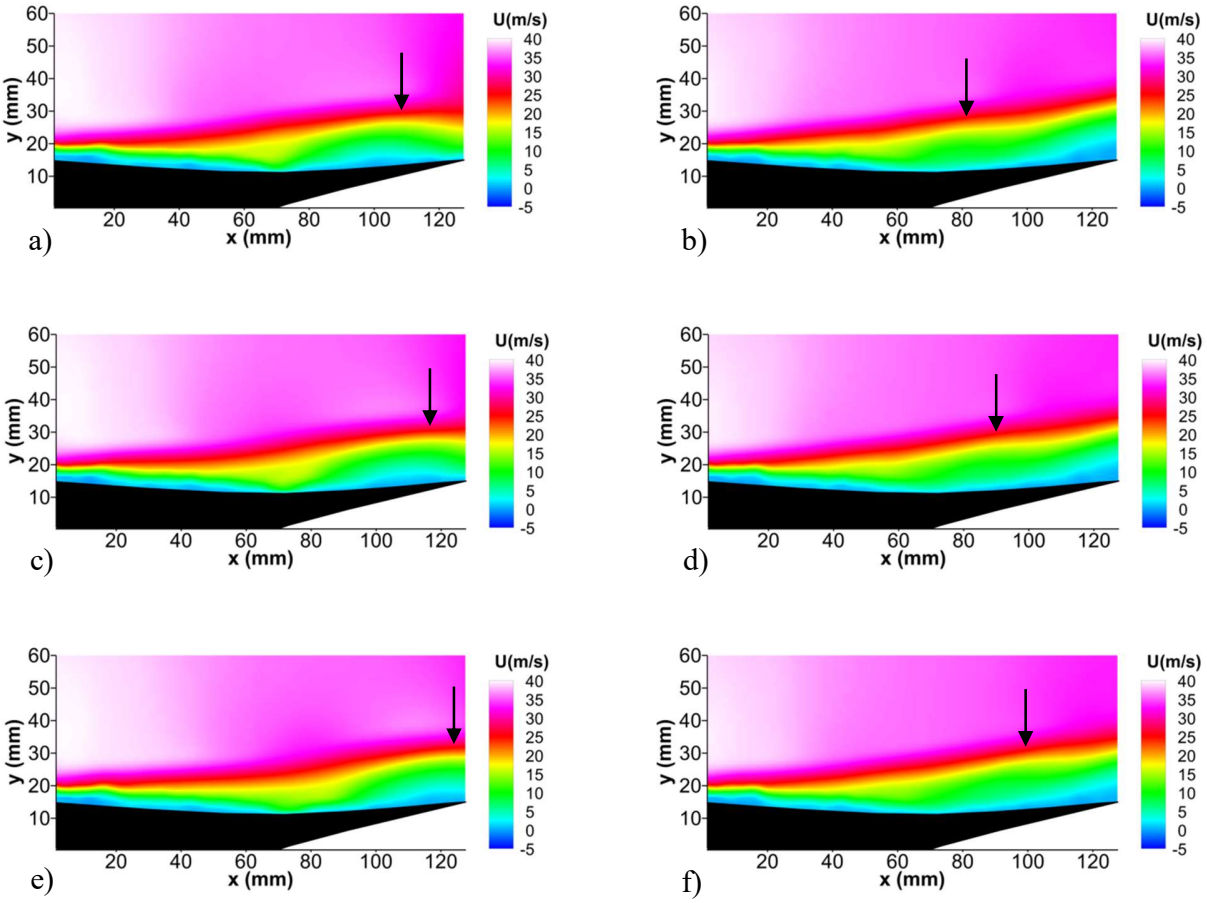

Fig. 3.9 Velocity fields across trailing-edge region for $F^+_{var} = 0.09$ (a), c), e), g), i), k), m) and o)) and $F^+ = 1$ (b), d), f), h), j), l), n) and p)). Arrows track the motion of ripples in the shear layer due to the interaction between the high momentum fluid in the potential flow region with the low momentum fluid in the shear layer.

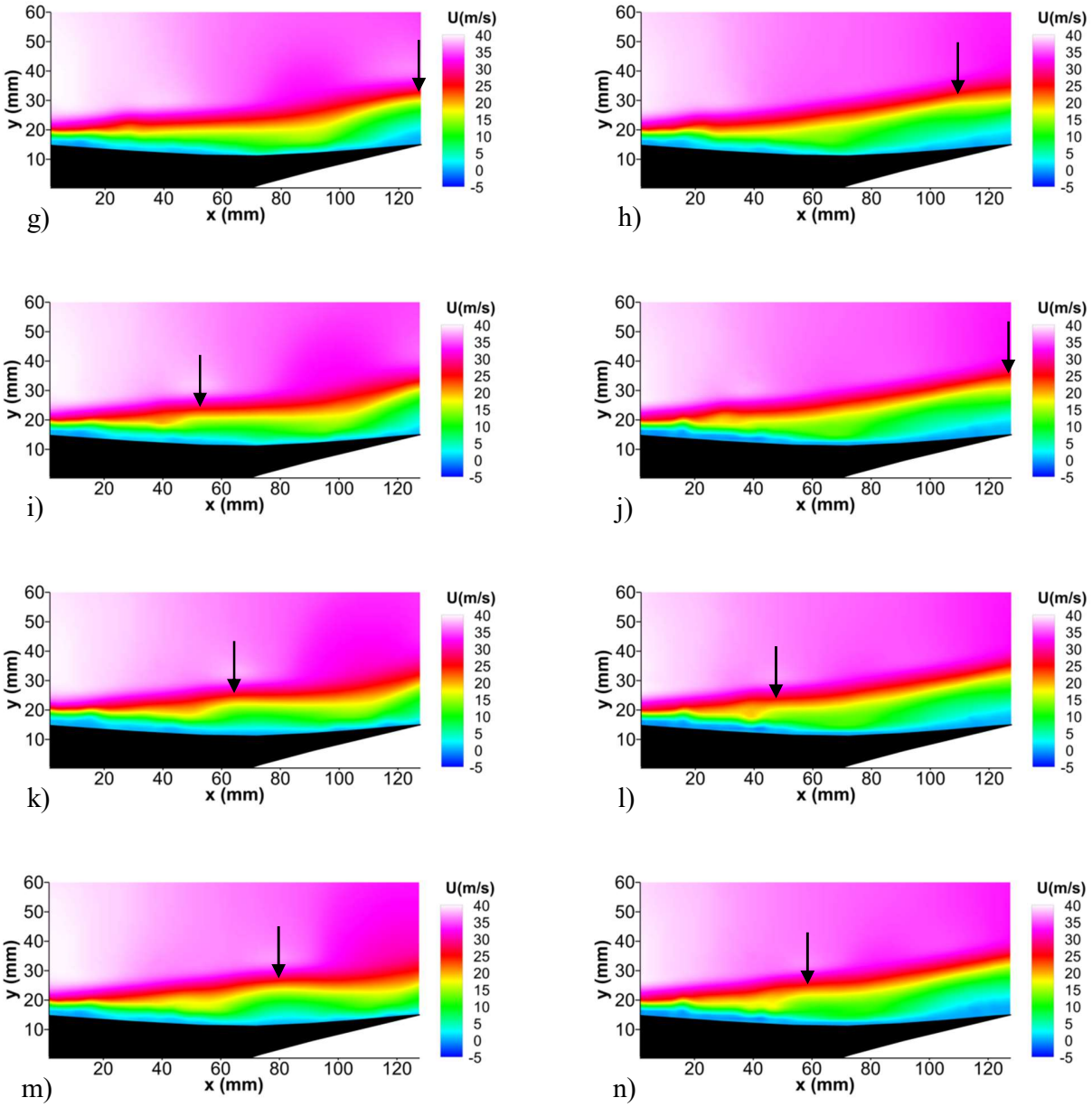

Fig. 3.9 (cont.) Velocity fields across trailing-edge region for F^{+}_{var} = 0.09 (a), c), e), g), i), k), m) and o)) and F^{+} = 1 (b), d), f), h), j), l), n) and p)). Arrows track the motion of ripples in the shear layer due to the interaction between the high momentum fluid in the potential flow region with the low momentum fluid in the shear layer.

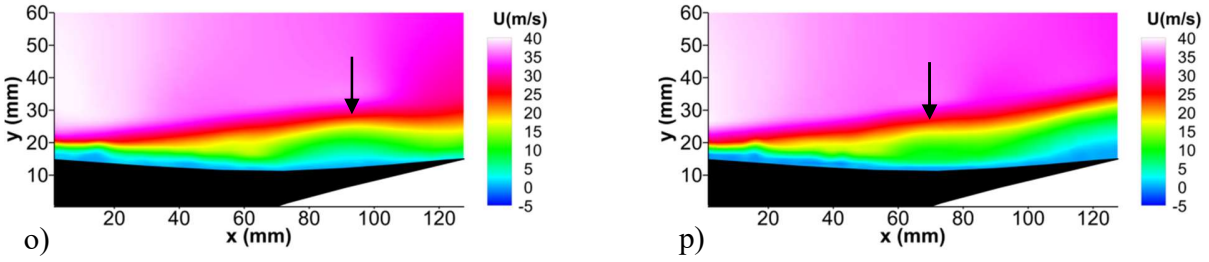

Fig. 3.9 (cont.) Velocity fields across trailing-edge region for F^{+}_{var} = 0.09 (a), c), e), g), i), k), m) and o)) and F^{+} = 1 (b), d), f), h), j), l), n) and p)). Arrows track the motion of ripples in the shear layer due to the interaction between the high momentum fluid in the potential flow region with the low momentum fluid in the shear layer.

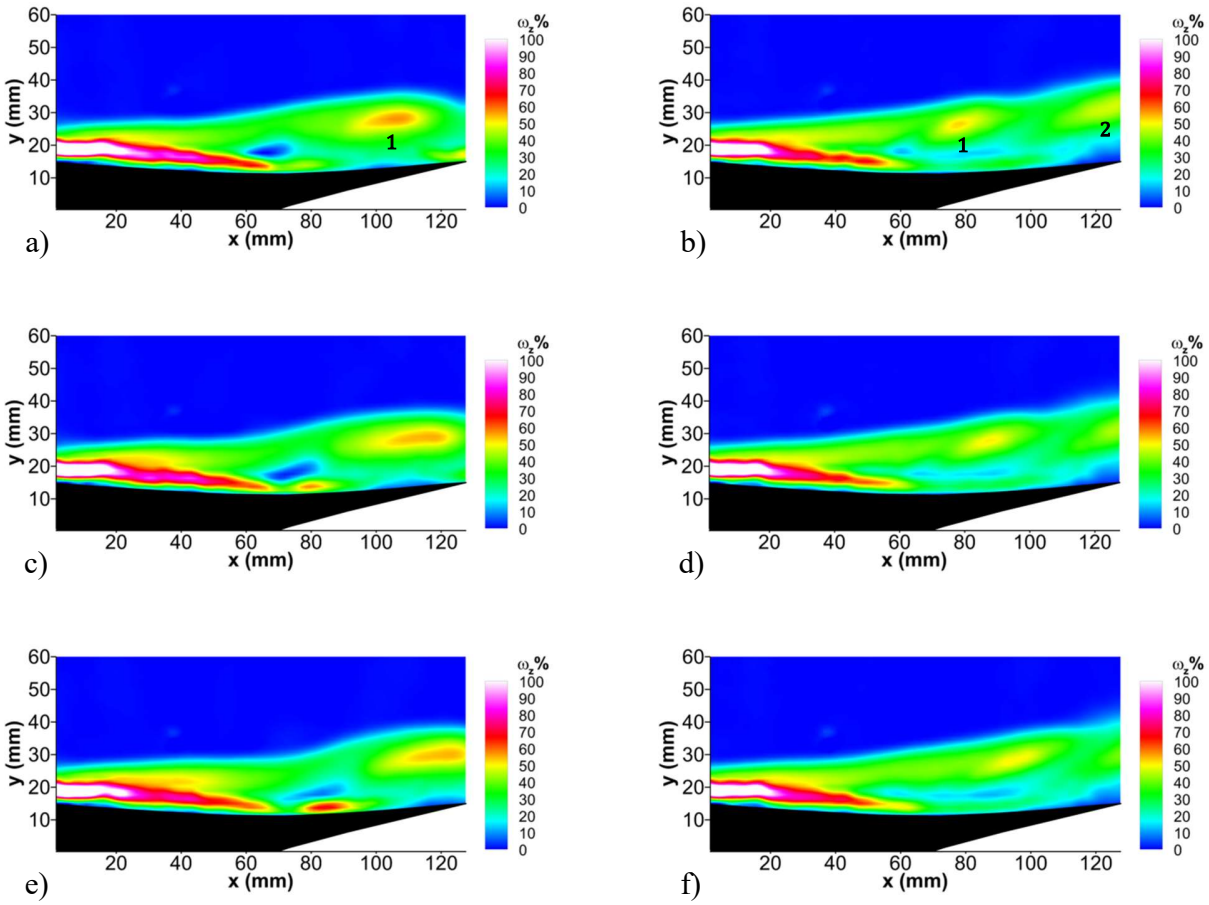

Fig. 3.10 Vorticity contours across trailing-edge region for F^{+}_{var} = 0.09 (a), c), e), g), i), k), m) and o)) and F^{+} = 1 (b), d), f), h), j), l), n) and p)).

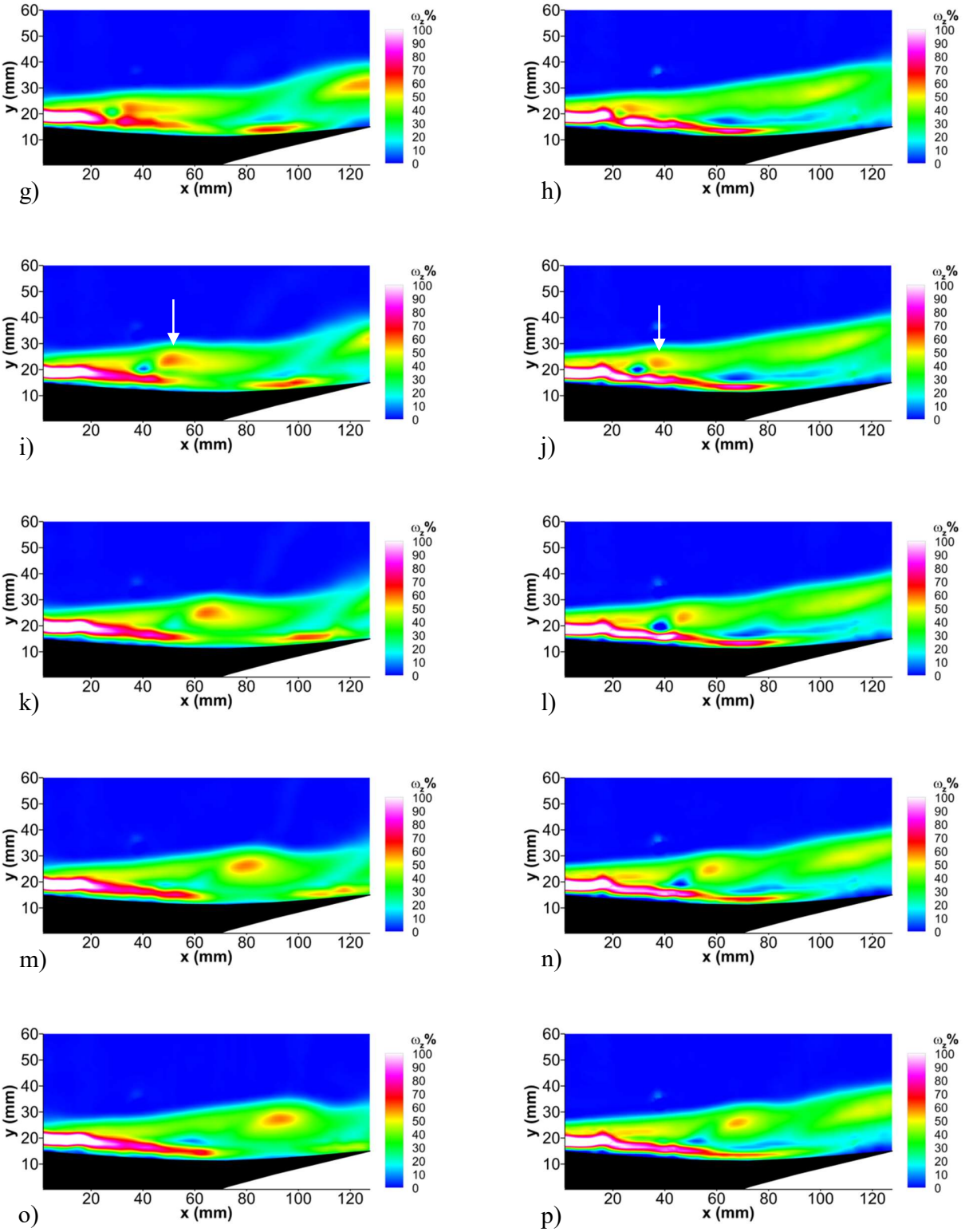

Fig. 3.10 (cont.) Vorticity contours across trailing-edge region for F^{+}_{var} = 0.09 (a), c), e), g), i), k), m) and o)) and F^{+} = 1 (b), d), f), h), j), l), n) and p)).

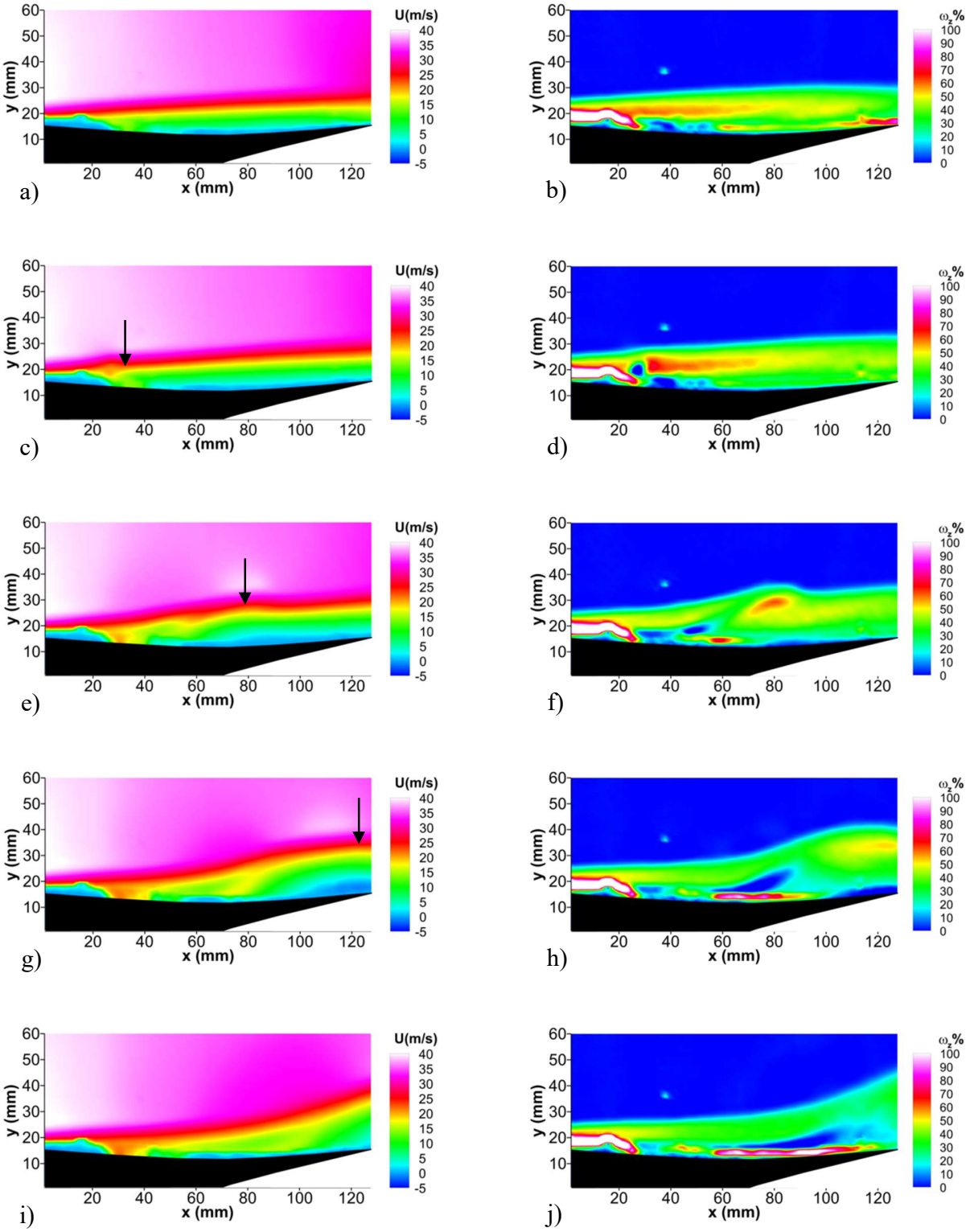

Fig. 3.11 F^+ = 0.25 phase-locked velocity fields (a), c), e), g), i), k), m) and o)) and vorticity contours (b), d), f), h), j), l), n) and p)).

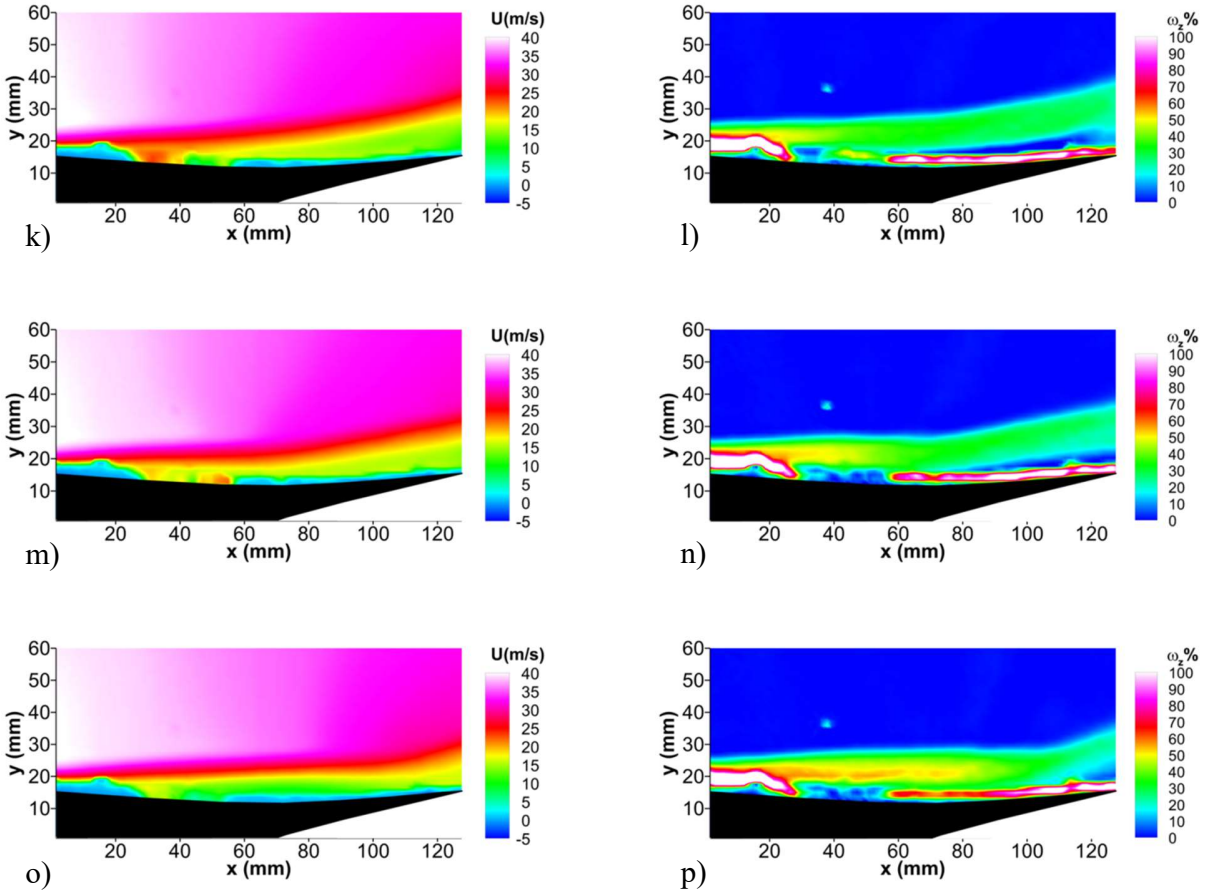

Fig. 3.11 (cont.) F^+ = 0.25 phase-locked velocity fields (a), c), e), g), i), k), m) and o)) and vorticity contours (b), d), f), h), j), l), n) and p)).

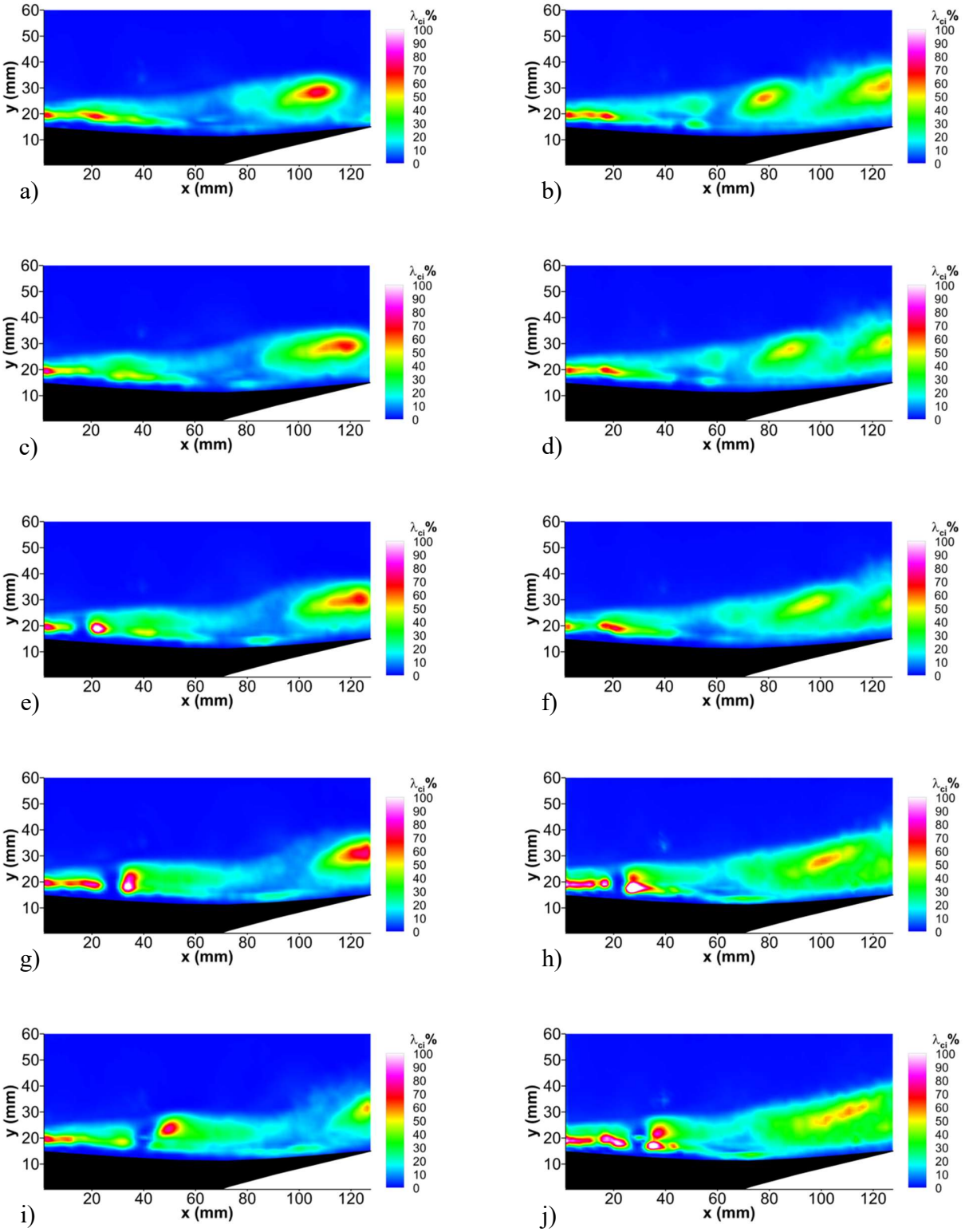

Fig. 3.12 Swirl strength contours across trailing-edge region for F^{+}_{var} = 0.09 (a), c), e), g), i), k), m) and o)) and F^{+} = 1 (b), d), f), h), j), l), n) and p)).

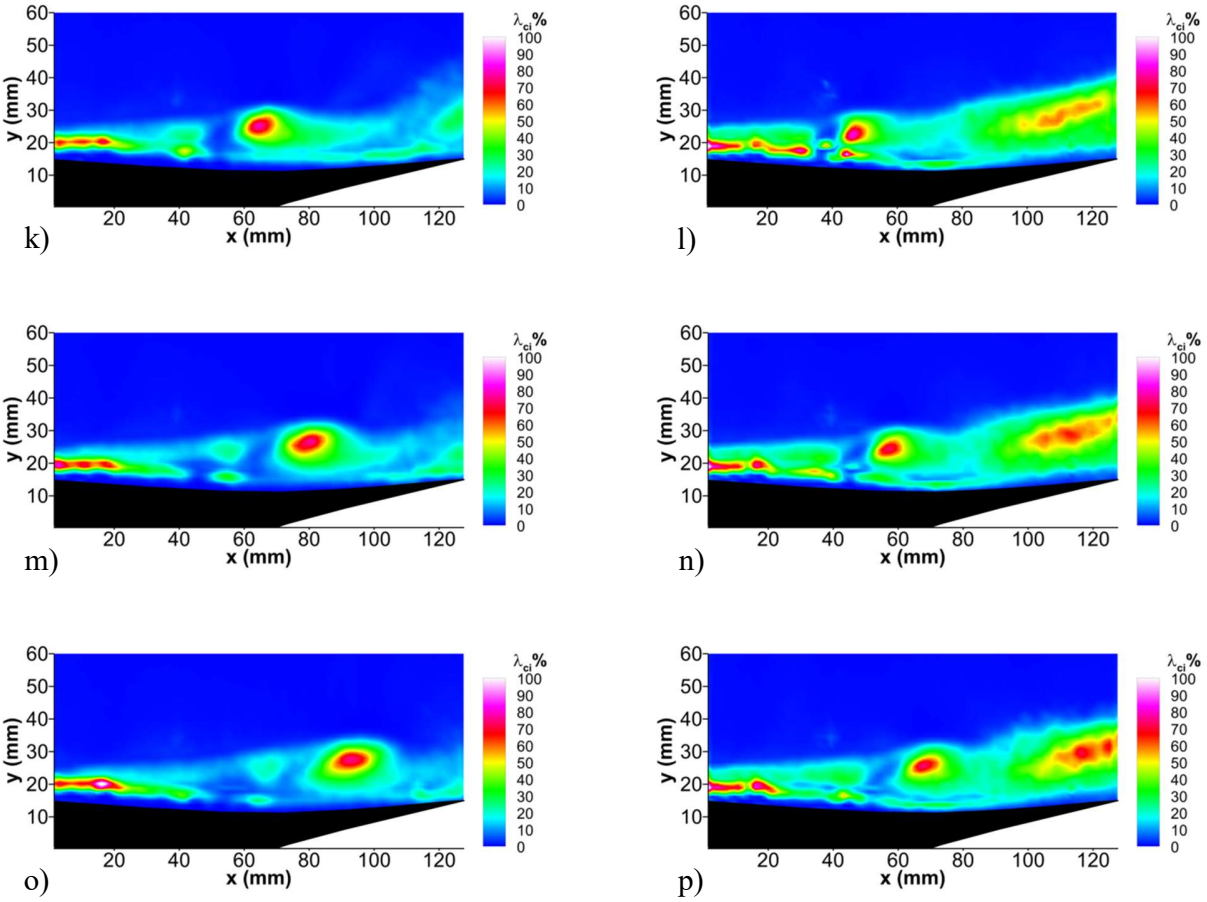

Fig. 3.12 (cont.) Swirl strength contours across trailing-edge region for F^{+}_{var} = 0.09 (a), c), e), g), i), k), m) and o)) and F^{+} = 1 (b), d), f), h), j), l), n) and p)).

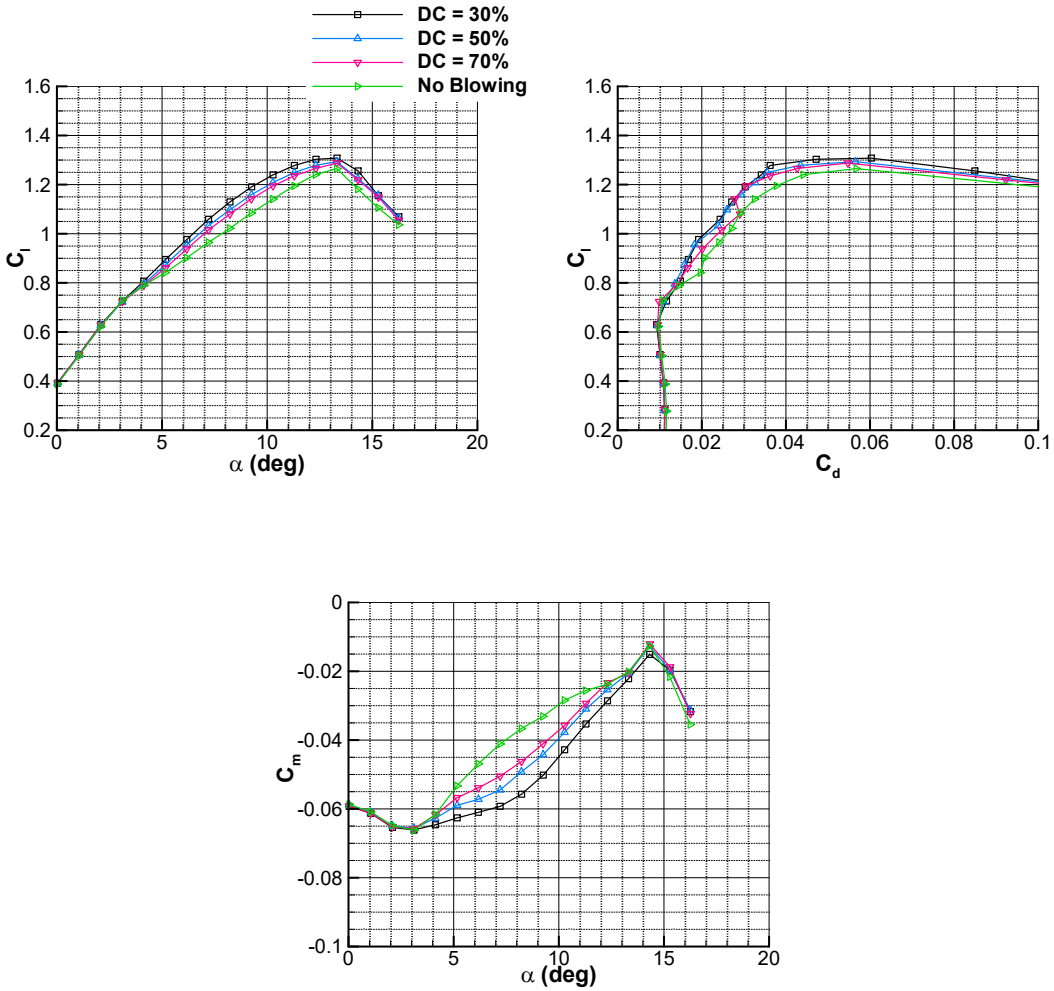

Fig. 3.13 Performance comparison of NLF 0414 for different duty cycles (*DC*) ($Re_c = 1 \times 10^6$).

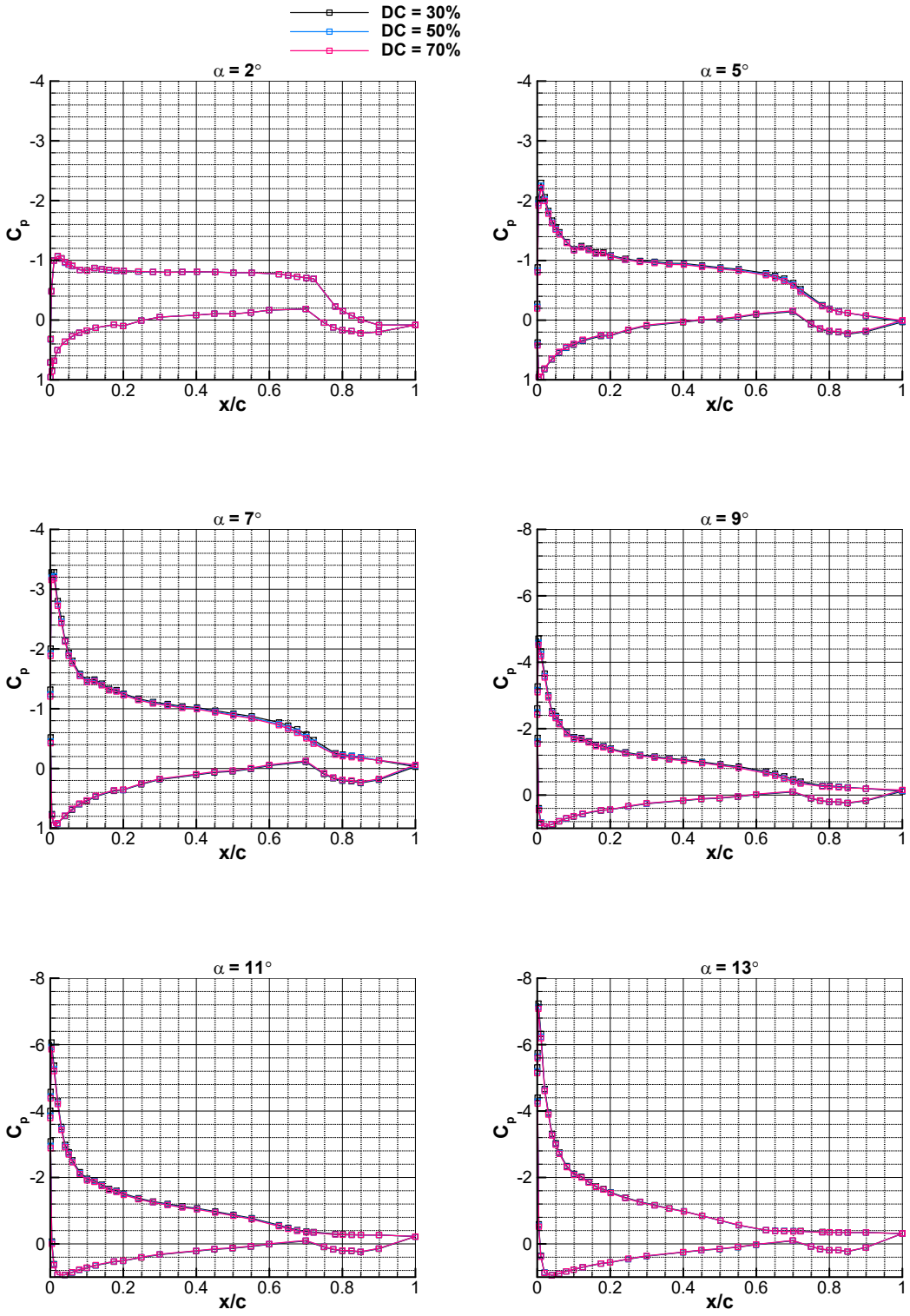

Fig. 3.14 Comparison of the pressure distributions (C_p) around NLF 0414 for DC = 30%, 50% and 70% at α = 2°, 5°, 7°, 9°, 11°, and 13° ($Re_c = 1 \times 10^6$).

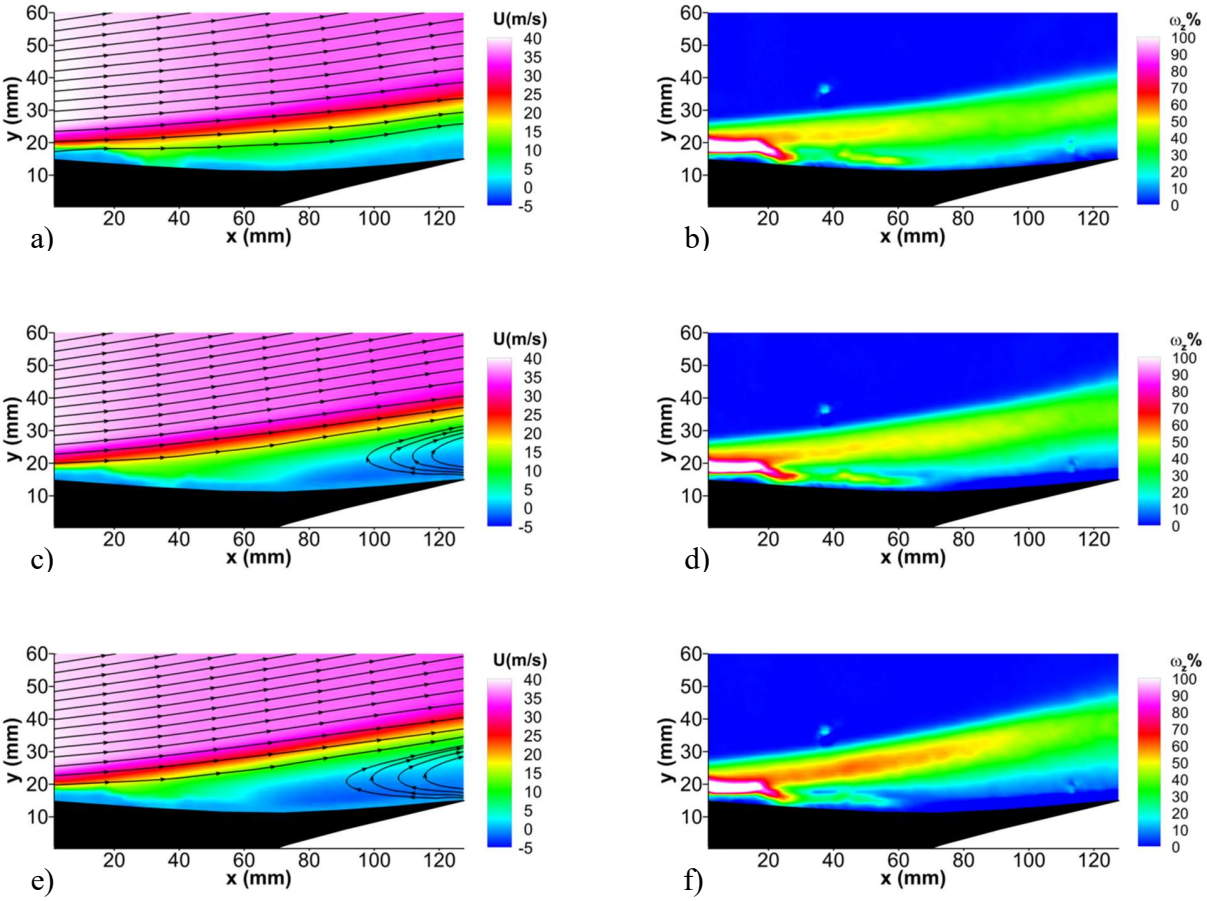

Fig. 3.15 Velocity and Vorticity contours across trailing-edge region for *DC* = 30% (a), b)), *DC* = 50% (c), d)) and *DC* = 70% (e) and f).

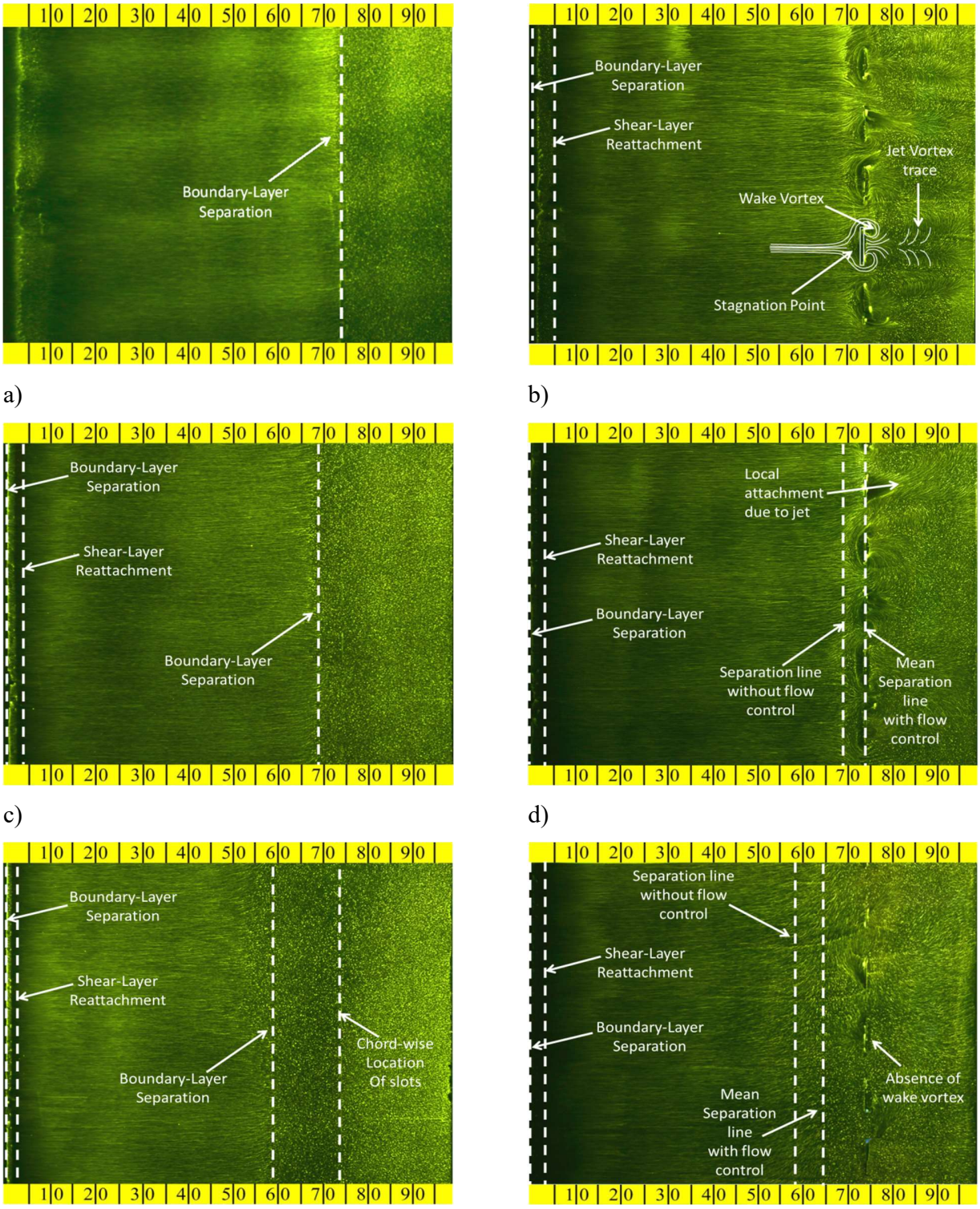

a) b)

c) d)

e) f)

Fig. 3.16 Comparison of the surface flow visualization images for the actuated and unactuated cases at (a), b)) α = 5°, (c), d)) α = 7° and (e), f)) α = 13°.

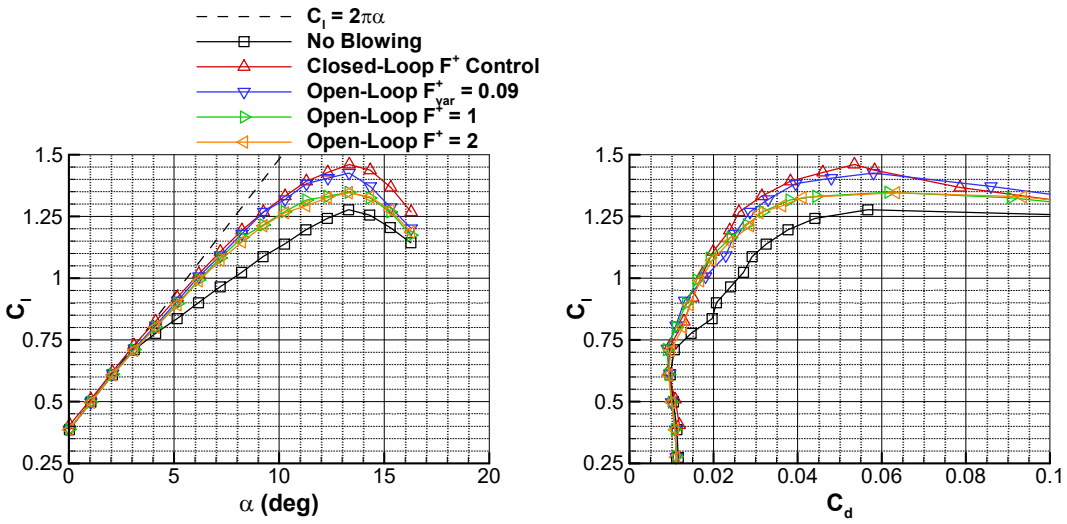

Fig. 3.17 Airfoil performance comparison between closed-loop and open-loop configurations ($Re_c = 1.0 \times 10^6$).

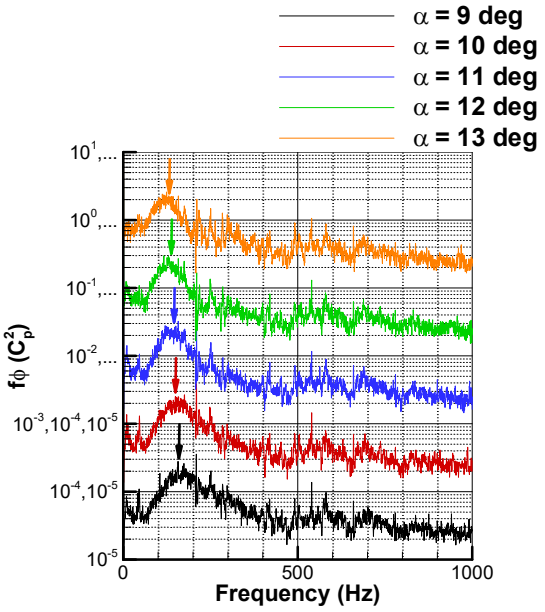

Fig. 3.18 Premultiplied spectra of C_p at x/c = 0.90 for NLF 0414 airfoil along with EMD-selected frequencies ($Re_c = 1.0 \times 10^6$).

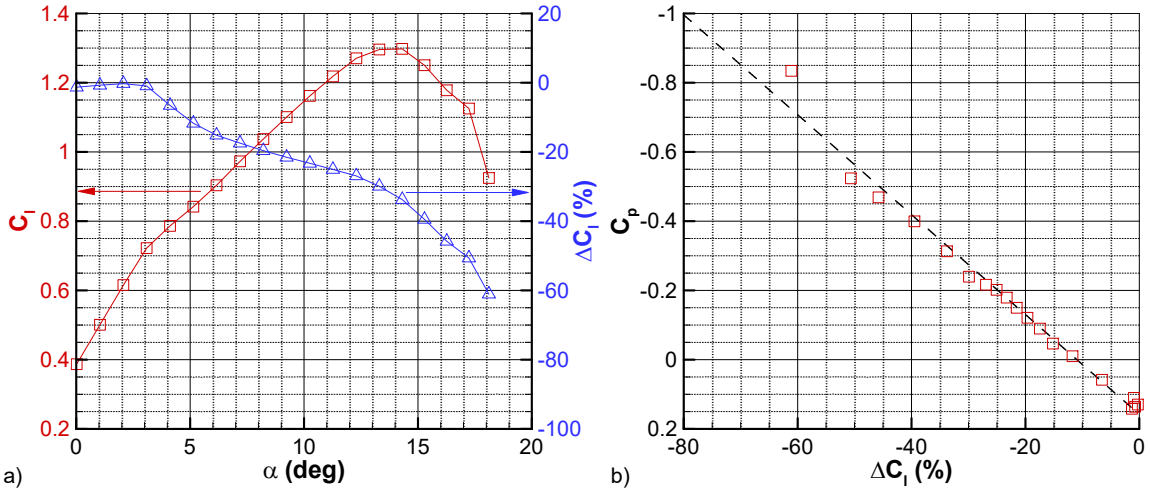

Fig. 3.19 Relationship between lift decrease and steady C_p at x/c = 0.90: a) no-blowing C_l and ΔC_l, b) linear relationship between C_p and ΔC_l.

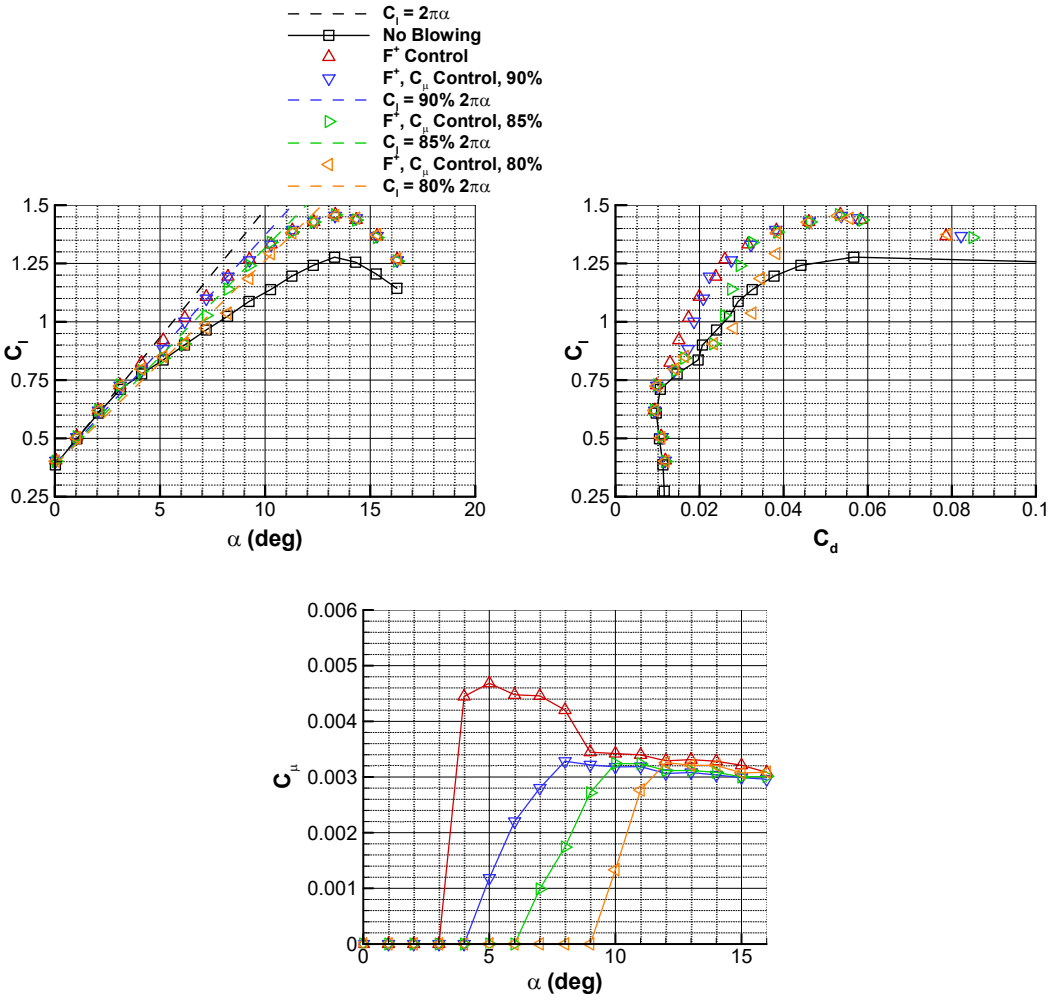

Fig. 3.20 Performance results of closed-loop control of trailing-edge separation ($Re_c = 1.0 \times 10^6$); control of actuation frequency and amplitude used to set C_l to a percentage of ideal value from theoretical model.

Chapter 4

Summary and Conclusions

In the current study, control of trailing-edge separation was achieved on an NLF 0414 airfoil in off-design conditions using active unsteady flow control. The NLF 0414 airfoil is associated with a well-defined trailing-edge separation as evident by a distinct change in the lift curve slope of the airfoil beyond $\alpha = 3°$ and corroborated by the surface pressure measurements and flow visualization results. The current investigation was motivated by a desire to improve the performance of the NLF 0414 beyond the design angle-of-attack range using active unsteady flow control.

All of the experiments were conducted at a chord-based Reynolds number, $Re_c = 1.0 \times 10^6$ in a 3-ft × 4-ft low-speed, low-turbulence wind tunnel. Unsteady actuation was constituted by means of fast-switching solenoid valves connected to blowing slots located at $x/c = 0.75$ on the upper surface of the airfoil model. The mass flow rate was precisely controlled using a pressure regulator and a mass flow meter. In addition to acquiring steady pressure measurements for evaluating the performance of the airfoil, high-frequency unsteady surface pressure measurements were also acquired to characterize the spectral content of the relevant modes in the unsteady flowfield around the trailing edge of the NLF 0414 airfoil. The center frequencies from the spectra of unsteady C_p were observed to correspond to a constant Strouhal number of 0.09 by utilizing the projected height of the aft quarter-chord of the airfoil ($csin\alpha/4$),

as the characteristic length scale. Actuation at the center frequencies was hypothesized to excite the natural instabilities in the shear layer leading eventually to the alleviation of separation at the trailing-edge region of the airfoil.

A set of open-loop trailing-edge separation control experiments were first conducted to parametrically investigate the effects of primary forcing parameters, i.e., C_μ, F^+ and DC, on the performance of the airfoil. A monotonic increase in C_l/C_d was observed with increasing magnitude of C_μ as the introduction of a higher momentum jet into the boundary layer produced stronger pressure recovery across the trailing-edge region of the airfoil.

Additionally, actuation at $F^+_{var} = 0.09$, $F^+ = 0.25$ and $F^+ = 0.5$ were observed to produce significant improvements in C_l/C_d as compared to $F^+ = 1$, $F^+ = 2$ and steady actuation for a fixed value of C_μ. Planar PIV data acquired across a horizontal plane at the trailing-edge region of the airfoil model revealed higher concentrations of vorticity near the surface of the airfoil for the $F^+_{var} = 0.09$, $F^+ = 0.25$ and $F^+ = 0.5$ cases indicating a greater degree of momentum mixing in the shear layer in comparison with the other actuation cases. Phase-locked planar PIV were also acquired to understand the spatio-temporal evolution of the flowfield for $F^+_{var} = 0.09$, $F^+ = 1$ and $F^+ = 0.25$. For the $F^+_{var} = 0.09$ case, the time-scale of the formation of coherent structures in the shear layer was observed to match the convective time scale of the flow. On the other hand, for $F^+ = 1$, vortical structures were observed to be more closely spaced in the shear layer causing them to merge and dissipate in strength due to their mutual interactions. The enhanced level of dissipation for $F^+ = 1$ resulted in weaker momentum entrainment near the trailing edge of the airfoil and in turn an inferior performance of airfoil in comparison with actuation at $F^+_{var} = 0.09$. A significantly different mechanism for separation control was observed for $F^+ = 0.25$. An initially non-localized distribution of vorticity in the shear layer was observed to undergo a Kelvin-Helmholtz type roll up process leading to the formation of a single, coherent vortical structure that was responsible for the alleviation of separation observed when actuating at $F^+ = 0.25$.

The performance of the airfoil was also found to increase monotonically with decreasing duty cycle of actuation for a fixed value of C_μ. This observation was also corroborated by the PIV measurements acquired at the corresponding actuation duty cycles. Since C_μ was defined to represent a total energy factor over a certain period of actuation, the higher effectiveness at the

lower duty cycles was found to be a result of higher blowing amplitude associated with a low duty cycle actuation for a constant average momentum flux over an actuation period.

The results from the open-loop separation control experiments were used to design a robust yet adaptive closed loop controller. Advanced signal processing techniques were used to extract the frequencies of natural instabilities in the flowfield in real time. These frequencies were found to correspond to the center frequencies of the pre-multiplied spectra of unsteady C_p. Performance measurements revealed that the closed-loop control case was equally or more effective than the open-loop actuation configurations utilized in this study. Control of C_μ was achieved through the design of a simple proportional controller wherein the mean C_p at $x/c = 0.9$ was utilized to estimate the state of the flow and the extent of trailing-edge separation. Blowing amplitude and actuation frequency were controlled simultaneously to maintain a desired performance metric, such as a prescribed C_l value, in a closed-loop context.

Chapter 5

Uncertainty Analysis

The experimental uncertainties associated with the results from the current investigation are presented in this chapter. The uncertainty in a measurement is described by Kline and McClintock[47] and Airy[48] as a "possible value that an error may have". An analysis of uncertainties is important in assessing the significance of the scatter associated with experimental results over multiple trials.[49] This assessment was necessary to provide a more robust interpretation of the experimental results. Experimental uncertainties can be classified as "fixed" or "random" based on the temporal characteristics of the error source and the process variability[49].

The "random" or "sampling" uncertainty (U_X) associated with a set of N observations of the variable (X) having a mean ($X_{(N)}$) can be calculated using,[49]

$$U_X = \frac{tS_{(N)}}{\sqrt{N}} \tag{5.1}$$

where t is the Student's t statistic appropriate for the number of samples N and the desired confidence interval, $S_{(N)}$ is the standard deviation of the set of N observations used to calculate the mean value $X_{(N)}$. The N samples of variable (X) are assumed to represent a Gaussian distribution.

The "fixed" or "bias" uncertainty (U_R) associated with the result of an experiment (R), represented by,

$$R = R(x_1, x_2, ..., x_n) \tag{5.2}$$

is expressed at the same odds as were used to estimate the uncertainties of each of the independent variables (x_i), by taking a root-square-sum of the corresponding uncertainty components produced by each variable[47]. The "bias" uncertainty can be calculated using,

$$U_R = \sqrt{\left(\frac{\partial R}{\partial x_1} U_{x_1}\right)^2 + \left(\frac{\partial R}{\partial x_2} U_{x_2}\right)^2 + ... + \left(\frac{\partial R}{\partial x_n} U_{x_n}\right)^2} \tag{5.3}$$

Using the aforementioned method, the resulting "bias" uncertainties associated with the flow conditions, pressure and performance coefficients, and active flow control parameters were calculated using the equations presented in section 5.1. A detailed derivation of these equations is presented in Ansell[40]. The resulting "sampling" uncertainty associated with the PIV measurements were also calculated using the methods described above and are discussed subsequently in section 5.2 .

5.1 Uncertainty in Performance Measurements

5.1.1 Uncertainty in Flow Conditions

The uncertainties associated with the flow conditions at which the experiments were run were calculated using the equations presented in this section. Examples of uncertainty values at 95% confidence level and at a reference condition are presented in Table 5.1. The results include estimates of the uncertainty in freestream dynamic pressure, atmospheric density, dynamic viscosity, freestream velocity, and Reynolds number. These uncertainties were calculated using,

$$U_{q_\infty} = \sqrt{\left(\frac{\partial q_\infty}{\partial (P_{ss} - P_{ts})} U_{(P_{ss} - P_{ts})}\right)^2} \tag{5.4}$$

$$U_{\rho_{amb}} = \sqrt{\left(\frac{\partial \rho_{amb}}{\partial P_{amb}} U_{P_{amb}}\right)^2 + \left(\frac{\partial \rho_{amb}}{\partial T_{amb}} U_{T_{amb}}\right)^2} \tag{5.5}$$

$$U_{\mu_{amb}} = \sqrt{\left(\frac{\partial \mu_{amb}}{\partial T_{amb}} U_{T_{amb}}\right)^2} \tag{5.6}$$

$$U_{U_\infty} = \sqrt{\left(\frac{\partial U_\infty}{\partial q_\infty} U_{q_\infty}\right)^2 + \left(\frac{\partial U_\infty}{\partial \rho_{amb}} U_{\rho_{amb}}\right)^2} \tag{5.7}$$

$$U_{\mathrm{Re}} = \sqrt{\left(\frac{\partial \mathrm{Re}}{\partial U_\infty} U_{U_\infty}\right)^2 + \left(\frac{\partial \mathrm{Re}}{\partial \rho_{amb}} U_{\rho_{amb}}\right)^2 + \left(\frac{\partial \mathrm{Re}}{\partial \mu_{amb}} U_{\mu_{amb}}\right)^2 + \left(\frac{\partial \mathrm{Re}}{\partial c} U_c\right)^2} \tag{5.8}$$

5.1.2 Uncertainty in Pressure and Performance Coefficients

The uncertainties associated with the pressure and performance coefficient results, i.e., C_p, C_l, C_m and C_d were calculated using the equations presented in this section. Examples of uncertainties from this section at the reference condition are presented in Table 5.2. Similar to the previous section, these uncertainties are reported at a 95% confidence level. The uncertainties in the pressure and performance coefficients were calculated using,

$$U_{C_p} = \sqrt{\left(\frac{\partial C_p}{\partial (P_s - P_{ts})} U_{(P_s - P_{ts})}\right)^2 + \left(\frac{\partial C_p}{\partial q_\infty} U_{q_\infty}\right)^2} \tag{5.9}$$

$$U_{C_l} = \sqrt{\left(\frac{\partial C_l}{\partial L'} U_{L'}\right)^2 + \left(\frac{\partial C_l}{\partial q_\infty} U_{q_\infty}\right)^2 + \left(\frac{\partial C_l}{\partial c} U_c\right)^2} \tag{5.10}$$

$$U_{C_m} = \sqrt{\left(\frac{\partial C_m}{\partial M'_{c/4}} U_{M'_{c/4}}\right)^2 + \left(\frac{\partial C_m}{\partial q_\infty} U_{q_\infty}\right)^2 + \left(\frac{\partial C_m}{\partial c} U_c\right)^2} \tag{5.11}$$

$$U_{C_d} = \sqrt{\left(\frac{\partial C_d}{\partial q_\infty} U_{q_\infty}\right)^2 + \left(\frac{\partial C_d}{\partial c} U_c\right)^2 + \left(\frac{\partial C_d}{\partial P_{0,\infty}} U_{P_{0,\infty}}\right)^2 + \sum_{i=1}^{n_{rake}-1} \left(\frac{\partial C_d}{\partial P_{0,w}} U_{P_{0,w}}\right)^2} \tag{5.12}$$

5.1.3 Uncertainty in Active Flow Control Parameters

The uncertainties associated with the non-dimensional actuation frequency, duty cycle and jet momentum coefficient were calculated using equations presented in this section. Example uncertainty values at 95% confidence level are presented in Table 5.3.

$$U_{F_{\text{var}}^+} = \sqrt{\left(\frac{\partial F_{\text{var}}^+}{\partial f}U_f\right)^2 + \left(\frac{\partial F_{\text{var}}^+}{\partial c}U_c\right)^2 + \left(\frac{\partial F_{\text{var}}^+}{\partial \alpha}U_\alpha\right)^2 + \left(\frac{\partial F_{\text{var}}^+}{\partial U_\infty}U_{U_\infty}\right)^2} \tag{5.13}$$

$$U_{F^+} = \sqrt{\left(\frac{\partial F^+}{\partial f}U_f\right)^2 + \left(\frac{\partial F^+}{\partial c}U_c\right)^2 + \left(\frac{\partial F^+}{\partial U_\infty}U_{U_\infty}\right)^2} \tag{5.14}$$

$$U_{C_\mu} = \sqrt{\left(\frac{\partial C_\mu}{\partial h_{slot}}U_{h_{slot}}\right)^2 + \left(\frac{\partial C_\mu}{\partial c}U_c\right)^2 + \left(\frac{\partial C_\mu}{\partial \rho_\infty}U_{\rho_\infty}\right)^2 + \left(\frac{\partial C_\mu}{\partial U_\infty}U_{U_\infty}\right)^2 + \left(\frac{\partial C_\mu}{\partial l_{slot}}U_{l_{slot}}\right)^2 + \left(\frac{\partial C_\mu}{\partial \dot{m}}U_{\dot{m}}\right)^2} \tag{5.15}$$

$$U_{DC} = \sqrt{\left(\frac{\partial DC}{\partial t_{ON}}U_{t_{ON}}\right)^2 + \left(\frac{\partial DC}{\partial T_s}U_{T_s}\right)^2} \tag{5.16}$$

Table 5.1 Example uncertainties for test conditions of NLF 0414 airfoil model at $Re_c = 1 \times 10^6$ and $\alpha = 7°$

Parameter	Reference Value	Absolute Uncertainty	Relative Uncertainty (%)
c	18 in	±0.005 in	±0.0278
α	6.991°	±0.02°	±0.2861
$q_{\infty,Setra}$	0.09602 psi	±0.000771 psi	±0.8026
$q_{\infty,PSI}$	0.09527 psi	±0.001425 psi	±1.4961
P_{amb}	14.45 psi	±0.008 psi	±0.0554
T_{amb}	526.8 °R	±1.8 °R	±0.3417
ρ_{amb}	2.302×10^{-3} slugs/ft^3	$\pm 7.867 \times 10^{-6}$ slugs/ft^3	±0.3417
μ_{amb}	3.783×10^{-7} lb-s/ft^2	$\pm 1.270 \times 10^{-9}$ lb-s/ft^2	±0.3358
U_∞	109.6 ft/sec	±0.1873 ft/sec	±0.1709
Re_c	1000590	±5097	±0.5094

Table 5.2 Example uncertainties for airfoil pressure and performance coefficients of NLF 0414 airfoil model at $Re_c = 1 \times 10^6$ and $\alpha = 7°$

Parameter	Reference Value	Absolute Uncertainty	Relative Uncertainty (%)
C_p 5 psi ($x/c = 0.10$)	-1.4449	±0.043530	±3.0130
C_p 1 psi ($x/c = 0.40$)	-0.9870	±0.020833	±2.1107
C_l	0.99125	±0.016006	±1.6147
C_m	-0.05245	±0.001844	±3.5160
C_d	0.02471	±0.000752	±3.0410

Table 5.3 Example uncertainties for active unsteady flow control parameters of NLF 0414 airfoil model at $Re_c = 1 \times 10^6$ and $\alpha = 7°$

Parameter	Reference Value	Absolute Uncertainty	Relative Uncertainty (%)
F^+_{var}	0.09	±0.000198	±2.1946
F^+	0.25	±0.001873	±0.7490
C_μ	0.00254	±0.000123	±4.8299
DC	50	±0.364430	±0.7289

5.2 PIV Uncertainty Analysis

The uncertainty associated with the PIV acquisition was estimated using methods described by Lazar et al.[50] These methods account for four major sources of uncertainty: Equipment uncertainty, uncertainty in Particle Dynamics, Sampling and Processing uncertainties.

Equipment uncertainty (U_E) includes uncertainties associated with the calibration scale, image distortion, jitter in the laser pulse timing and the accuracy of the delay generator used to control the timings of the laser and camera system.

The uncertainty in the Particle Dynamics (U_L) accounts for the out-of-plane motion of the seed particles and a lag in the motion of these particles with respect to the local flow velocity caused primarily due to the Stokes drag force, particularly in regions with large velocity gradients. The particle lag velocity can be calculated using,

$$u_f - u_p = \frac{1}{18}\frac{\rho_p d_p^2}{\mu_f}\left(\frac{\partial u_p}{\partial x_p}\frac{\partial x_p}{\partial t} + \frac{\partial u_p}{\partial y_p}\frac{\partial y_p}{\partial t}\right) \tag{5.17}$$

where u_f is the local velocity of the fluid, u_p is the velocity of the seed particle, ρ_p is the density of the seed particles, d_p represents the particle diameter, μ_f represents the fluid viscosity and x_p and y_p represent the local coordinate directions.

The time-averaged PIV vector fields and statistics reported in this investigation were derived from a set of instantaneous velocity vector fields recorded at statistically independent instances in time. The Sampling uncertainty (U_S) in the time-averaged PIV results was used to evaluate the scatter associated with these instantaneous velocity vector fields at a given confidence interval. In the current investigation, the sampling uncertainty was estimated by assuming a Gaussian distribution of statistically independent instantaneous velocity fields following a process that is identical to that outlined in the introduction to this chapter. Thus, the scatter in the flow velocity (σ_V) evaluated at a certain confidence level around the sample mean $V_{(N)}$ for a set of N samples with a standard deviation $S_{(N)}$ is given by,

$$\sigma_V = V_{(N)} \pm \frac{tS_{(N)}}{\sqrt{N}} \tag{5.18}$$

Processing uncertainty (U_P) is used to evaluate the accuracy and reliability of the digital processing techniques, particularly the image pre- and post-processing algorithms, filtering procedures and cross-correlation methods that are employed to transform the raw particle image pairs into meaningful vector fields. The processing uncertainty was evaluated by generating synthetic image pairs for the flowfield of interest based on the input velocity field using a synthetic PIV program created within a MATLAB environment. These synthetic image pairs were then processed using identical processing steps as were used with the acquired particle image pairs in order to obtain the corresponding vector fields. The processing uncertainty was then calculated by comparing the vector fields generated by the particle image pairs acquired during experimentation with those produced by the synthetic image pairs.

As with the performance uncertainties, the total PIV uncertainty (U_T) can be calculated through a root-mean-square sum of the individual uncertainties from four dominant sources discussed above. The total PIV uncertainty was calculated using,

$$U_T = \sqrt{U_E^2 + U_L^2 + U_S^2 + U_P^2} \tag{5.19}$$

The freestream normalized uncertainties in the streamwise and transverse velocity field measurements for the baseline airfoil at $Re_c = 1 \times 10^6$ and $\alpha = 7°$ is presented in Fig. 5.1. The corresponding uncertainties for the case in which actuation was performed at $F^+_{var} = 0.09$ is

presented in Fig. 5.2. Similar to the uncertainties in the performance measurements, the uncertainty associated with PIV acquisition is reported at a 95% confidence level.

5.3 Chapter 5 Figures

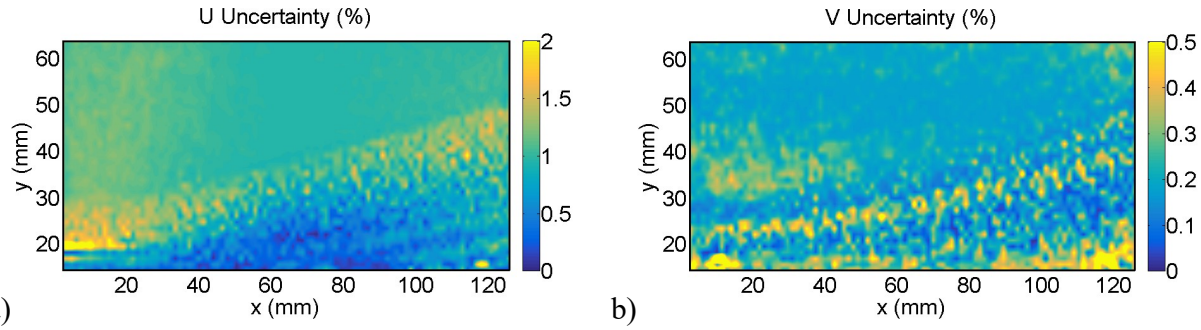

Fig. 5.1 PIV Uncertainty for freestream normalized a) streamwise and b) transverse velocity components for the baseline airfoil at $Re_c = 1 \times 10^6$ and $\alpha = 7°$.

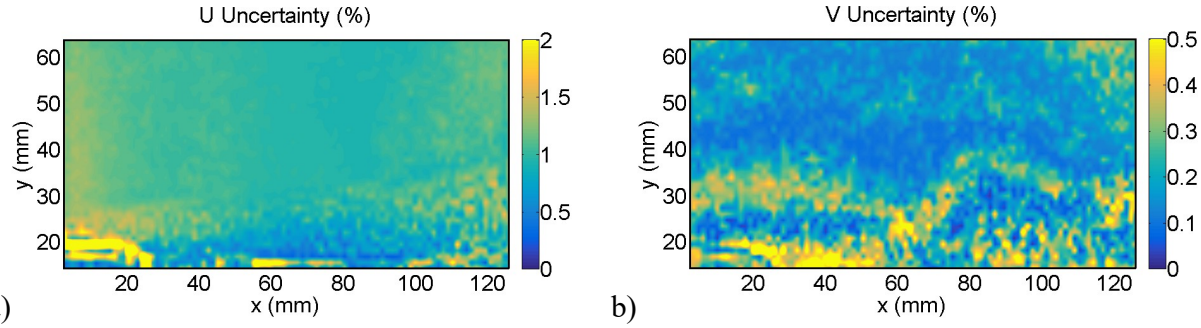

Fig. 5.2 PIV Uncertainty for freestream normalized a) streamwise and b) transverse velocity components for $F^+_{var} = 0.09$ case at $Re_c = 1 \times 10^6$ and $\alpha = 7°$.

References

[1] Gad-el-Hak, "*Flow Control*," Applied Mechanics Review, ASME, Vol. 42, no 10, 1989.

[2] Schubauer, G.B., Skramstad, H.K., "*Laminar boundary layer oscillations and transition on a flat plate*," NACA Rep 909, 1948.

[3] Seifert, A., Bachar, T., Koss, T., Wygnanski, I., "*Oscillatory blowing, a tool to delay boundary layer separation*," AIAA paper 93-0440, 31st AIAA Aerospace Sciences Meeting, 1993.

[4] Wu, J.-Z., Lu, X.-Y., Denny, A. G., Fan, M., and Wu, J.-M., "*Post-Stall Flow Control on an Airfoil by Local Unsteady Forcing*," Journal of Fluid Mechanics, Vol. 371, 1998, pp. 21-58.

[5] McCormick, D. C., "*Boundary Layer Separation Control with Directed Synthetic Jets*," AIAA paper 2000-0519, 38th AIAA Aerospace Sciences Meeting and Exhibit, 2000.

[6] Raju, R., Mittal, R., and Cattafesta, L., "*Dynamics of Airfoil Separation Control using Zero-Net Mass-Flux Forcing*," AIAA Journal, Vol. 46, No. 12, 2008, pp. 3103-3115.

[7] Griffin, J., Oyarzun, M., Cattafesta, L. N., Tu, J. H., Rowley, C. W., Mittal, R., "*Control of a canonical separated flow*," 43rd Fluid Dynamics Conference, 2013.

[8] Amitay, M., Glezer, A., "*Role of actuation frequency in controlled flow reattachment over a stalled airfoil*," AIAA journal, 40(2), 2002, pp. 209-216.

[9] Volino, R. J., Kartuzova, O., Ibrahim, M. B., "*Separation Control on a Very High Lift Low Pressure Turbine Airfoil Using Pulsed Vortex Generator Jets*," J. Turbomach, 133, 041021, 2011, 13 pages; doi:10.1115/1.4003024.

[10] Packard, N. O., Bons, J. P., "*Pulsed Blowing on a Laminar Airfoil at Low Reynolds Number*," AIAA paper 2011-3173, 2011.

[11] Hipp, K. D., Benton, S. I., Walker, M. M., Bons, J. P., "*Parametric Optimization of Control for a Post-Stall Airfoil Using Pulsed Jets*," 53rd AIAA Aerospace Sciences Meeting, 2015.

[12] Hecklau, M., Wiederhold, O., Zander, V., King, R., Nitsche, W., Huppertz, A., Swoboda, M., "*Active separation control with pulsed jets in a critically loaded compressor cascade*," AIAA journal, 49(8), 2011, pp. 1729-1739.

[13] Lee, B., Kim, M., Choi, B., Kim, C., Kim, H. J., Jung, K., "*Closed-loop active flow control of stall separation using synthetic jets*," AIAA Paper, 2013, *2925*.

[14] Becker, R., King, R., Petz, R., Nitsche, W., "*Adaptive closed-loop separation control on a high-lift configuration using extremum seeking*," AIAA journal, 45(6), 2007, 1382-1392.

[15] Lombardi, A. J., Bowles, P. O., Corke, T. C., "*Closed-loop dynamic stall control using a plasma actuator*," AIAA journal, 51(5), 2013, 1130-1141.

[16] Pinier, J. T., Ausseur, J. M., Glauser, M. N., Higuchi, H., "*Proportional closed-loop feedback control of flow separation*," AIAA journal, 45(1), 2007, 181-190.

[17] Viken, J. K., Watson-Viken, S. A., Pfenninger, W., Morgan Jr, H. L., Campbell, R. L., "*Design of the low-speed NLF (1)-0414F and the high-speed HSNLF (1)-0213 airfoils with high-lift systems*," 1987.

[18] Englar, R. J., "*Subsonic Two-Dimensional Wind Tunnel Investigations of the High Lift Capability of Circulation Control Wing Sections* (No. DTNSRDC/ASED-274)," David W Taylor Naval Ship Research and Development Center, Aviation and Surface Effects Dept, Bethesda MD, 1975.

[19] Günther, B., Carnarius, A., Thiele, F., "*Numerical investigation of active flow control applied to an airfoil with a camber flap*," Active Flow Control II (pp. 45-61), 2010, Springer Berlin Heidelberg.

[20] Jones, B. M., "*Measurement of Profile Drag by the Pitot-Traverse Method*," Tech. Rep. 1688, Aeronautical Research Council R&M, 1936.

[21] Schlichting, H., "*Boundary-Layer Theory*," McGraw-Hill Book Company, New York, 1979.

[22] Fingerson, L.M. and Freymuth, P., "*Thermal Anemometers*," in Goldstein, R.J., "*Fluid Mechanics Measurements*", 2nd ed., Washington DC, Taylor & Francis, 1996, Chapter 3.

[23] Tropea, C., Yarin, A.L., and Foss, J.F., "*Springer Handbook of Experimental Fluid Mechanics*," Springer-Verlag, Berlin, 2007.

[24] Spring, S.A., "*An Experimental Mapping of the Flow Field Behind a Glaze Ice Shape on a NACA 0012 Airfoil*," M.S. Thesis, The Ohio State University, Columbus, OH, 1987.

[25] Adrian, R. J., Westerweel, J, "*Particle image velocimetry* (No. 30)," Cambridge University Press, 2011.

[26] Barlow, J.B., Rae, W.H. Jr. and Pope, A., "*Low-Speed Wind Tunnel Testing*," 3rd Edition, John Wiley & Sons, Inc., New York, 1999.

[27] Bendat, J.S. and Piersol, A.G., "*Random Data: Analysis and Measurement Procedures*," 3rd Edition, John Wiley & Sons, Inc., New York, 2000.

[28] Wygnanski, I., "*Boundary layer and flow control by periodic addition of momentum*," AIAA paper, 2117, 1997.

[29] Huang, N.E., Shen, Z, Long, S.R., Wu, M.C., Shih, H.H., Zheng, Q., Yen, N., Tung, C.C., and Liu, H.H., "*The Empirical Mode Decomposition and the Hilbert Spectrum for Nonlinear and Non-Stationary Time Series Analysis*," Proceedings of the Royal Society A, Vol. 454, No. 1971, 1998, pp. 903–995.

[30] Huang, N.E. and Shen, S.S., "*Hilbert-Huang Transform and its Applications*," World Scientific, Singapore, 2005.

[31] Huang, N.E. and Attoh-Okine, N.O., "*The Hilbert-Huang Transform in Engineering*," CRC Taylor & Francis, 2005.

[32] Wu, Z. and Huang, N.E., "*A Study of the Characteristics of White Noise Using the Empirical Mode Decomposition Method*," Proceedings of the Royal Society A, Vol. 460, No. 2046, 2004, pp. 1597–1611.

[33] Lee, Y.S., Tsakirtzis, S., Vakakis, A.F., Bergman, L.A., and McFarland, D.M., "*Physics-Based Foundation for Empirical Mode Decomposition*," AIAA Journal, Vol. 47, No. 12, 2009, pp. 2938-2963.

[34] Huang, Y., Schmitt, F.G., Lu, Z., and Liu, Y., "*Empirical Mode Decomposition Analysis of Experimental Homogeneous Turbulence Time Series*," 21° Colloque GRETSI, 2007.

[35] Agostini, L. and Leschziner, M.A., "*On the Influence of Outer Large-Scale Structures on Near-Wall Turbulence in Channel Flow*," Physics of Fluids, Vol. 26, 2014.

[36] Rilling, G., Flandrin, P., and Gonçalves, P., "*On Empirical Mode Decomposition and its Algorithms*," IEEE-EURASIP Workshop on Nonlinear Signal and Image Processing (NSIP-03), 2003.

[37] Rilling, G., Flandrin, P., Gonçalves, P., and Lilly, J.M., "*Bivariate Empirical Mode Decomposition*," IEEE Signal Processing Letters, Vol. 14, No. 12, 2007, pp. 936-939.

[38] Flandrin, P., Rilling, G., and Gonçalves, P., "*Empirical Mode Decomposition as a Filter Bank*," IEEE Signal Processing Letters, Vol. 11, No. 2, 2004, pp. 112-114.

[39] Deering, R. and Kaiser, J.F., "*The Use of a Masking Signal to Improve Empirical Mode Decomposition*," Proceedings from IEEE International Conference on Acoustics, Speech, and Signal Processing, 2005, Vol. 4, pp. 485-488.

[40] Ansell, P.J., "*Unsteady Modes in the flowfield about an airfoil with a leading-edge horn-ice shape* (Doctoral Dissertation)," University of Illinois at Urbana-Champaign, Urbana, IL, 2014.

[41] Yarusevych, S., Sullivan, P. E., & Kawall, J. G., "*Coherent structures in an airfoil boundary layer and wake at low Reynolds numbers*," Physics of Fluids (1994-present), 18(4), 044101, 2006.

[42] Batchelor, G. K., "*An introduction to fluid dynamics*," Cambridge university press, 2000.

[43] Zhou, Y. and Antonia, R.A., "*Convection velocity measurements in a cylinder wake*," Experiments in Fluids, 2007, *13*(1), pp.63-70.

[44] Josserand, C. and Rossi, M., *"The merging of two co-rotating vortices: a numerical study,"* European Journal of Mechanics-B/Fluids, 2007, 26(6), pp.779-794.

[45] Fric, T. F., Roshko, A., "*Vortical structure in the wake of a transverse jet*," Journal of Fluid Mechanics, *279*, 1994, 1-47.

[46] Smith, S. H., & Mungal, M. G., "*Mixing, structure and scaling of the jet in crossflow*," *Journal of Fluid Mechanics*, *357*, 1998, 83-122.

[47] Kline, S. J., and McClintock, F. A., "*Describing Uncertainties in Single Sample Experiments*," Mech. Eng., 3-8 Jan. 1953.

[48] Airy, Sir George Biddle, "*Theory of Errors of Observation*," Macmillan, London, 1879.

[49] Moffat, R.J., "*Describing the Uncertainties in Experimental Results*," Experimental and Thermal Fluid Sciences, Vol. 1, No. 1, 1988, pp. 3–17.

[50] Lazar, E., DeBlauw, B., Glumac, N., Dutton, C. and Elliott, G., "*A practical approach to PIV uncertainty analysis*," 27th AIAA Aerodynamic Measurement Technology and Ground Testing Conference, Vol. 28, 2010.